THE PHYSICS AND CHEMISTRY OF MATERIALS

THE PHYSICS AND CHEMISTRY OF MATERIALS

Joel I. Gersten
Frederick W. Smith

The City College of the City University of New York

A WILEY-INTERSCIENCE PUBLICATION

JOHN WILEY & SONS, INC.

New York • Chichester • Weinheim • Brisbane • Singapore • Toronto

This book is printed on acid-free paper. ♾

Published simultaneously in Canada.

Library of Congress Cataloging-in-Publication Data:

Gersten, Joel I. (Joel Irwin)
The physics and chemistry of materials / Joel I. Gersten, Frederick W. Smith.
p. cm.
ISBN 0-471-05794-0 (cloth : alk. paper)
1. Solid state chemistry. 2. Solid-state physics. 3. Materials. I. Smith, Frederick W. (Frederick William), 1942–II. Title.
QD478 .G47 2001
541′.0421 — dc21 2001026009

Printed in the United States of America.

10 9 8 7 6 5 4 3 2 1

For Harriet and Françoise

WEB CONTENTS

PREFACE

As science has become more interdisciplinary and impinges ever more heavily on technology, we have been led to the conclusion that there is a great need now for a textbook that emphasizes the physical and chemical origins of the properties of solids while at the same time focusing on the technologically important materials that are being developed and used by scientists and engineers. A panel of physicists, chemists, and materials scientists who participated in the NSF Undergraduate Curriculum Workshop in Materials in 1989, which addressed educational needs and opportunities in the area of materials research and technology, issued a report that indicated clearly the need for advanced textbooks in materials beyond the introductory level. Our textbook is meant to address this need.

This textbook is designed to serve courses that provide engineering and science majors with their first in-depth introduction to the properties and applications of a wide range of materials. This ordinarily occurs at the advanced undergraduate level but can also occur at the graduate level. The philosophy of our approach has been to define consistently the structure and properties of solids on the basis of the local chemical bonding and atomic order (or disorder!) present in the material. Our goal has been to bring the science of materials closer to technology than is done in most traditional textbooks on solid-state physics. We have stressed properties and their interpretation and have avoided the development of formalism for its own sake. We feel that the specialized mathematical techniques that can be applied to predict the properties of solids are better left for more advanced, graduate-level courses.

This textbook will be appropriate for use in the advanced materials courses given in engineering departments. Such courses are widely taught at the junior/senior level with such titles as "Principles of Materials Science & Engineering," "Physical Electronics," "Electronics of Materials," and "Engineering Materials." This textbook is also designed to be appropriate for use by physics and chemistry majors. We note that a course in materials chemistry is a relatively new one in most chemistry undergraduate curricula but that an introductory course in solid-state physics has long been standard in physics undergraduate curricula.

To gain the most benefit from courses based on this textbook, students should have had at least one year each of introductory physics, chemistry, and calculus, along with a course in modern physics or physical chemistry. For optimal use of the textbook it would be helpful if the students have had courses in thermodynamics, electricity and magnetism, and an introduction to quantum mechanics.

As the title indicates, the range of topics covered in this textbook is quite broad. The 21 chapters are divided into five sections. The range of topics covered is comprehensive, but not exhaustive. For example, topics not covered in detail due to lack of space include biomaterials, a field with a bright future, and composites, examples of which are discussed only within specific classes of materials. Much more material is presented

than can be covered in a one-semester course. Actual usage of the text in courses will be discussed after the proposed subject matter has been outlined.

Following an introduction, which emphasizes the importance of materials in modern science and technology, Section I, on the "Structure of Materials," consists of four chapters on the structure of crystals, bonding in solids, diffraction and the reciprocal lattice, and order and disorder in solids.

Section II, on the "Physical Properties of Materials," consists of six chapters on phonons; thermally activated processes, phase diagrams, and phase transitions; electrons in solids: electrical and thermal properties; optical properties; magnetic properties; and mechanical properties.

Section III, titled "Classes of Materials," consists of eight chapters on semiconductors; metals and alloys; ceramics; polymers; dielectric and ferroelectric materials; superconductors; magnetic materials; and optical materials. In each chapter the distinctive properties of each class of materials are discussed using technologically-important examples from each class. In addition, the structure and key properties of selected materials are highlighted. In this way an indication of the wide spectrum of materials in each class is presented.

Section IV, titled "Surfaces, Thin Films, Interfaces, and Multilayers," consists of two chapters covering these important topics. Here the effects of spatial discontinuities in the physical and chemical structure on the properties of materials are presented, both from the point of view of creating materials with new properties and also of minimizing the potential materials problems associated with surfaces and interfaces.

Section V, titled "Synthesis and Processing of Materials," consists of a single chapter. Representative examples of how the structure and properties of materials are determined by the techniques used to synthesize them are presented. "Atomic engineering" is stressed. The tuning of structure and properties using postsynthesis processing is also illustrated.

Problem sets are presented at the end of each chapter and are used to emphasize the most important concepts introduced, as well as to present further examples of important materials. Illustrations are employed for the purpose of presenting crystal structures and key properties of materials. Tables are used to summarize and contrast the properties of related groups of materials.

We have created a home page that provides a valuable supplement to the textbook by describing additional properties of materials, along with additional examples of current materials and their applications. Chapter W22 on our home page emphasizes the structural and chemical characterization of materials, as well as the characterization of their optical, electrical, and magnetic properties. As new materials and applications are developed, the home page will be regularly updated.

Since this text will likely be used most often in a one-semester course, we recommend that Chapters 1–4 on structure be covered in as much detail as needed, given the backgrounds of the students. A selection of chapters on the properties of materials (5–10) and on the classes of materials (11–18) of particular interest can then be covered. According to the tastes of the instructor and the needs of the students, some of the remaining chapters (surfaces; thin films, interfaces, and multilayers; synthesis and processing of materials) can be covered. For example, a course on engineering materials could consist of the following: Chapters 1–4 on structure; Chapter 6 on thermally activated processes, etc.; Chapter 10 on mechanical properties; Chapter 12 on metals and

alloys; Chapter 13 on ceramics; Chapter 14 on polymers; and Chapter 21 on synthesis and processing.

Physics majors usually take an introductory course in solid-state physics in their senior year. Therefore in such a course it will be necessary to start at "the beginning," i.e., Chapter 1 on the structure of crystals. Students in MS&E or engineering departments who have already taken an introductory course on materials can quickly review (or skip) much of the basic material and focus on more advanced topics, beginning with Chapter 5 on phonons, if desired, or Chapter 7 on electrons in solids.

We owe a debt of gratitude to our colleagues at The City College and City University who, over the years, have shared with us their enthusiasm for and interest in the broad and fascinating subject of materials. They include R. R. Alfano, J. L. Birman, T. Boyer, F. Cadieu, H. Z. Cummins, H. Falk, A. Genack, M. E. Green, L. L. Isaacs, M. Lax, D. M. Lindsay (deceased), V. Petricevic, F. H. Pollak, S. R. Radel, M. P. Sarachik, D. Schmeltzer, S. Schwarz, J. Steiner, M. Tamargo, M. Tomkiewicz, and N. Tzoar (deceased). Colleagues outside CUNY who have shared their knowledge with us include Z. L. Akkerman, R. Dessau, H. Efstathiadis, B. Gersten, Y. Goldstein, P. Jacoby, L. Ley, K. G. Lynn, D. Rahoi, and Z. Yin. Our thanks also go to our students and postdocs who have challenged us, both in our research and teaching, to refine our thinking about materials and their behavior.

Special thanks are due to Gregory Franklin who served as our editor at John Wiley & Sons for the bulk of the preparation of this textbook. His unflagging support of this effort and his patience are deeply appreciated. Thanks are also due to our current editor, George Telecki, who has helped us with sound advice to bring this project to a successful conclusion. We acknowledge with gratitude the skill of Angioline Loredo who supervised the production of both the textbook and supplementary Web-based material. We have appreciated the useful comments of all the anonymous reviewers of our textbook and also wish to thank all the authors who granted permission for us to use their artwork.

Finally, we gratefully acknowledge the constant support, encouragement, and patience of our wives, Harriet and Françoise, and our families during the years in which this textbook was prepared. Little did we (or they) know how long it would take to accomplish our goals.

JOEL I. GERSTEN
FREDERICK W. SMITH

New York City

LIST OF TABLES

INTRODUCTION

The study of materials and their properties and applications is an important part of modern science and technology. As may be expected for such a wide-ranging subject, the study of materials is a multidisciplinary effort, encompassing segments of physics, chemistry, and essentially all branches of engineering, including aerospace, chemical, civil, electrical, and mechanical. In addition, the relatively new discipline of materials science and engineering focuses directly on the study of the properties and applications of materials.

Materials can be classified as being either natural or artificial, the latter corresponding to materials, not found in nature, that are prepared by humans. Important natural materials have included organic materials such as wood, ivory, bone, fiber, and rubber, along with inorganic materials such as minerals and ceramics (stone, flint, mica, quartz, clay, and diamond) and metals such as copper and gold. Different eras of civilization have been given names corresponding to the materials from which tools were made: for example, the Stone Age, the Chalcolithic (Copper–Stone) Age, the Bronze Age, and the Iron Age. Recently, the dominant technological materials have been manufactured, such as steels as structural materials and the semiconductor Si for electronics.

Although the use of solid materials extends to prehistory, the systematic study and development of materials have begun much more recently, within the last 100 years. Development of the periodic table of the elements in the nineteenth century and the resulting grouping of elements with similar properties played a crucial role in setting the stage for the development of materials with desired properties. The discovery that x-rays could be used to probe the internal structure of solids early in the twentieth century also played a key role in accelerating the study of materials.

The study of materials as presented in the textbook, *The Physics and Chemistry of Materials*, begins with in-depth discussions of the structure of materials in Chapters 1 to 4 and of the fundamental principles determining the physical properties of materials in Chapters 5 to 10. Following these discussions of structure and properties, which apply to all materials, eight essentially distinct classes of materials are discussed in Chapters 11 to 18, with emphasis placed on their special properties and applications. The surfaces of materials, interfaces between materials, and materials in the form of thin films and multilayers are then discussed in Chapters 19 and 20. A discussion of the synthesis and processing (S&P) of materials follows in Chapter 21, with emphasis both on general issues and also on the S&P of specific materials.

In addition to the text material, supplementary material for all the chapters is found here, our home page at the Wiley Web site. This material includes a wide range of additional discussions of the properties and applications of materials. Also, experimental techniques used for the characterization of a wide range of materials properties are discussed in Chapter W22. The following topics are reviewed briefly in

the appendices appearing at the Web site: thermodynamics, statistical mechanics, and quantum mechanics.

The eight classes of materials discussed in this book include semiconductors, metals and alloys, ceramics, polymers, dielectrics and ferroelectrics, superconductors, magnetic materials, and optical materials. Our discussions of these materials are meant to provide an introduction and solid grounding in the specific properties and applications of each class. Although each class of materials is often considered to be a separate specialty and the basis for a distinct area of technology, there are, in fact, many areas of overlap between the classes, such as magneto-optical materials, ceramic superconductors, metallic and ceramic permanent magnet materials, semiconductor lasers, dilute magnetic semiconductors, polymeric conductors, and so on.

There have been many materials success stories over the years, including the high-T_c superconductors, a-Si:H in photovoltaic solar cells, Teflon and other polymers, optical fibers, laser crystals, magnetic disk materials, superalloys, composite materials, and superlattices consisting of alternating layers of materials such as semiconductors or metals. These materials, most of which have found successful applications, are described throughout.

Our understanding of the structure of materials at the atomic level is well developed and, as a result, our understanding of the influence of atomic-level microstructure on the macroscopic properties of materials continues to improve. Between the microscopic and macroscopic levels, however, there exists an important additional level of structure at an intermediate length scale, often determined by defects such as grain boundaries, dislocations, inclusions, voids, and precipitates. Many of the critical properties of materials are determined by phenomena such as diffusion and interactions between defects that occur on this intermediate structural level, sometimes referred to as the mesoscopic level. Our understanding of phenomena occurring on this level in the heterogeneous (e.g., polycrystalline, amorphous, and composite) materials that are used in modern technology remains incomplete. Many of the properties of materials that are critical for their applications (e.g., mechanical properties) are determined by phenomena occurring on this level of microstructure.

Useful materials are becoming more complex. Examples include the high-T_c copper oxide–based ceramic superconductors, rare earth–based permanent magnets, bundles of carbon nanotubes, and even semiconductors such as Si–Ge alloys employed in strained layers and superlattices. Recent and continuing advances in the design and manipulation of materials atom by atom to create artificial structures are revolutionary steps in the development of materials for specific applications. This area of nanotechnology is an important focus of this book.

As we enter the twenty-first century and the world population and the depletion of resources both continue to increase, it is clear that the availability of optimum materials will play an important role in maintaining our quality of life. It is hoped that textbooks such as this one will serve to focus the attention of new students, as well as existing researchers, scientists, and engineers, toward the goals of developing and perfecting new materials and new applications for existing materials.

CHAPTER W1

Structure of Crystals

W1.1 Crystal Structures Based on Icosahedral Bonding Units

While the $A-A_{12}$(cub) and $A-A_{12}$(hex) bonding units appear in the FCC and HCP crystal structures, respectively, the crystal structures that include $A-A_{12}$(icos) and $A-B_{12}$(icos) *icosahedral* units are generally much more complicated. An example of a crystal structure based in part on the $A-B_{12}$(icos) unit, see Fig. 1.11 of the textbook,[†] is the *β-tungsten* (β-W) crystal structure, an interesting example of which is the intermetallic compound Nb_3Sn. This compound is of the *Frank–Kasper* tetrahedrally close-packed type, with each Sn atom surrounded icosahedrally by 12 Nb atoms at an interatomic distance of 0.296 nm and with each Nb atom at the center of a coordination number CN 14 polyhedron surrounded by four Sn atoms at 0.296 nm, two Nb atoms at 0.264 nm, and eight other Nb atoms at 0.324 nm. Frank–Kasper phases with CN 15 and CN 16 coordination polyhedra also exist (e.g., Fe_7W_6 with CN 12, CN 14, CN 15, and CN 16 coordination polyhedra). In general, larger atoms occupy the CN 15 and CN 16 central sites and smaller atoms occupy the CN 12 and CN 14 central sites.

Another family of close-packed structures based on both icosahedral units and polyhedral units with more than 12 NN is known as the *Laves phases*, the prototype of which is the intermetallic compound $MgCu_2$. In this structure each Mg atom is at the center of a CN 16 polyhedron with 12 Cu atoms at 0.292 nm and four Mg atoms at 0.305 nm, while each Cu atom is surrounded icosahedrally by six Mg atoms at 0.305 nm and six Cu atoms at 0.249 nm.

W1.2 Packing Fractions of BCC and CsCl Crystal Structures

The BCC crystal structure results when an identical atom is placed in the body-centered interstitial site of the SC crystal structure. Now $N(\text{atom}) = 2$ and, as can be seen in Fig. W1.2b,[†] three atoms are in contact along the body diagonal (of length $\sqrt{3}\,a$) of the unit cell in the [111] direction. The atoms along the cube edge are no longer in contact with each other. It follows that $\sqrt{3}\,a = r + 2r + r = 4r$, and therefore $V(\text{atom}) = \sqrt{3}\pi a^3/16$. Finally,

$$\text{PF(BCC)} = \frac{(2)(\sqrt{3}\pi a^3/16)}{a^3} = \frac{\sqrt{3}\pi}{8} = 0.68. \tag{W1.1}$$

[†] The material on this home page is supplemental to *The Physics and Chemistry of Materials* by Joel I. Gersten and Frederick W. Smith. Cross-references to material herein are prefixed by a "W"; cross-references to material in the textbook appear without the "W."

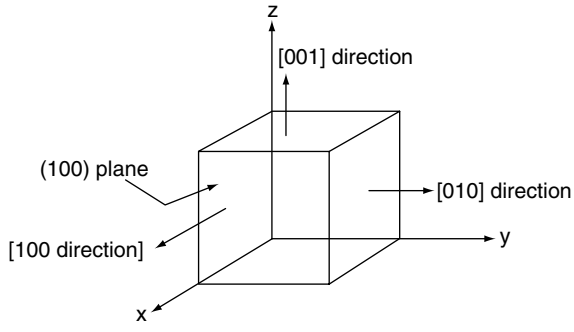

Figure W1.1. Directions in a lattice.

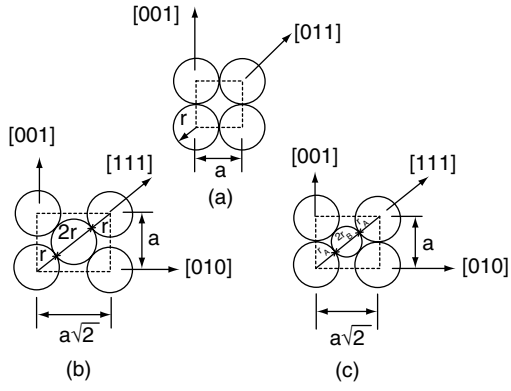

Figure W1.2. Diagrams used in the calculations of packing fractions for the following crystal structures: (*a*) simple cubic (SC), with the atoms lying in a (100) plane; (*b*) body-centered cubic (BCC), with the atoms lying in a $(\bar{1}10)$ plane; (*c*) cesium chloride (CsCl), with the atoms shown in a $(\bar{1}10)$ plane.

The CsCl crystal structure results when a smaller B atom is placed at the body-centered interstitial site of the SC crystal structure, so that it makes contact with the eight larger A atoms surrounding it. For the special case where $r_A = a/2$ and $r_B/r_A = (\sqrt{3} - 1)$, the two A atoms remain in contact along a cube edge, as shown in Fig. W1.2c. It follows, therefore, that $\sqrt{3}a = 2r_A + 2r_B$ along the cube body diagonal. The atom volumes are given by $V(\text{atom A}) = \pi a^3/6$ and $V(\text{atom B}) = (\sqrt{3} - 1)^3 \pi a^3/6$. With one A and one B atom per unit cell, the packing fraction is therefore

$$\begin{aligned} \text{PF} &= \frac{(1)(\pi a^3/6)}{a^3} + \frac{(1)(\sqrt{3} - 1)^3(\pi a^3/6)}{a^3} \\ &= 0.52 + 0.21 = 0.76. \end{aligned} \tag{W1.2}$$

This is the largest possible value for the packing fraction of two spherical atoms of different radii in the CsCl crystal structure and is higher than the value of PF = 0.74 for the FCC and HCP crystal structures.

W1.3 Density of CsCl

To illustrate the use of Eqs. (1.7) and (1.8) of the textbook, consider the case of CsCl where the lattice constant is $a = 0.411$ nm and the atomic masses are $m(\text{Cs}) = 2.207 \times 10^{-25}$ kg and $m(\text{Cl}) = 0.5887 \times 10^{-25}$ kg. Therefore,

$$n(\text{atom}) = \frac{2 \text{ atoms}}{(0.411 \times 10^{-9} \text{ m})^3} = 2.88 \times 10^{28} \text{ atoms/m}^3, \tag{W1.3}$$

$$\rho = \frac{(1)(2.207 \times 10^{-25} \text{ kg})}{(0.411 \times 10^{-9} \text{ m})^3} + \frac{(1)(0.5887 \times 10^{-25} \text{ kg})}{(0.411 \times 10^{-9} \text{ m})^3}$$

$$= 4027 \text{ kg/m}^3. \tag{W1.4}$$

PROBLEM

W1.1 Explain why icosahedral clusters of 13 atoms, corresponding to $A-A_{12}$(icos), are more stable (i.e., have a lower energy) than FCC or HCP clusters of 13 atoms [i.e., $A-A_{12}$(cub) and $A-A_{12}$(hex)]. [*Hint*: Count the number of "bonds" formed in each cluster between pairs of atoms that are in contact or, in the case of $A-A_{12}$(icos), nearly in contact with each other.]

CHAPTER W2

Bonding in Solids

W2.1 Atomic, Hybrid, and Molecular Orbitals Involved in Bonding in Solid-State Materials

When isolated atoms come together to form a solid, the atomic orbitals of the valence electrons are often modified as bonding between the atoms occurs. In this section the orbitals for electrons in isolated atoms (i.e., the atomic orbitals) are described first. The hybrid orbitals resulting from combinations of atomic orbitals on the same atom are described next, followed by a description of the molecular orbitals that result when atomic or hybrid orbitals on different atoms combine with each other as the atoms form bonds. It should be emphasized at the outset that the atomic, hybrid, and molecular orbitals described here are just useful approximations to the actual solutions of the Schrödinger equation for atoms and molecules. The derivations of mathematical expressions for these orbitals are not given here since it is outside the scope of this material to present in detail the physics and chemistry of atoms and molecules.

Atomic Orbitals. The *atomic orbitals* of the electrons in an atom correspond to the solutions of the Schrödinger equation for the wavefunctions ψ which are labeled with the three *quantum numbers* n, l, and m_l [i.e., $\psi(nlm_l)$]. (The magnetic quantum number m_s is discussed later.) The energies and spatial extents of the electrons in the atomic orbitals are determined by the *principal quantum number* n, which has allowed values $n = 1, 2, 3, \ldots, \infty$. For example, the binding energies of the $\psi(nlm_l)$ atomic orbitals in atomic hydrogen decrease as $1/n^2$ while their radii increase as n^2. The *orbital angular momentum quantum number* l specifies the angular momentum of the electron and can take on the values $l = 0, 1, 2, \ldots, n-1$. For example, for $n = 4$, the allowed values of l are 0 (for s states), 1 (for p states), 2 (for d states), and 3 (for f states). The *quantum number* m_l determines the *orientation* of the orbital in space and can have the $(2l + 1)$ integral values lying between $-l$ and $+l$. For d states with $l = 2$ the five allowed values of m_l are -2, -1, 0, $+1$, and $+2$.

The probability of finding the electron at a point in space is proportional to the value of $|\psi(nlm_l)|^2$ at that point. The charge density associated with the electron in this orbital is given by $-e|\psi|^2$. The *electronic charge densities* for one-electron or hydrogenic atoms and ions are shown schematically in Fig. W2.1 for the single s, three p (p_x, p_y, and p_z), and five d ($d_{x^2-y^2}$, d_{z^2}, d_{xy}, d_{yz}, and d_{xz}) atomic orbitals. The shapes of these orbitals as shown are only schematic (e.g., the orbitals do not actually have the sharp boundaries indicated in the figure).

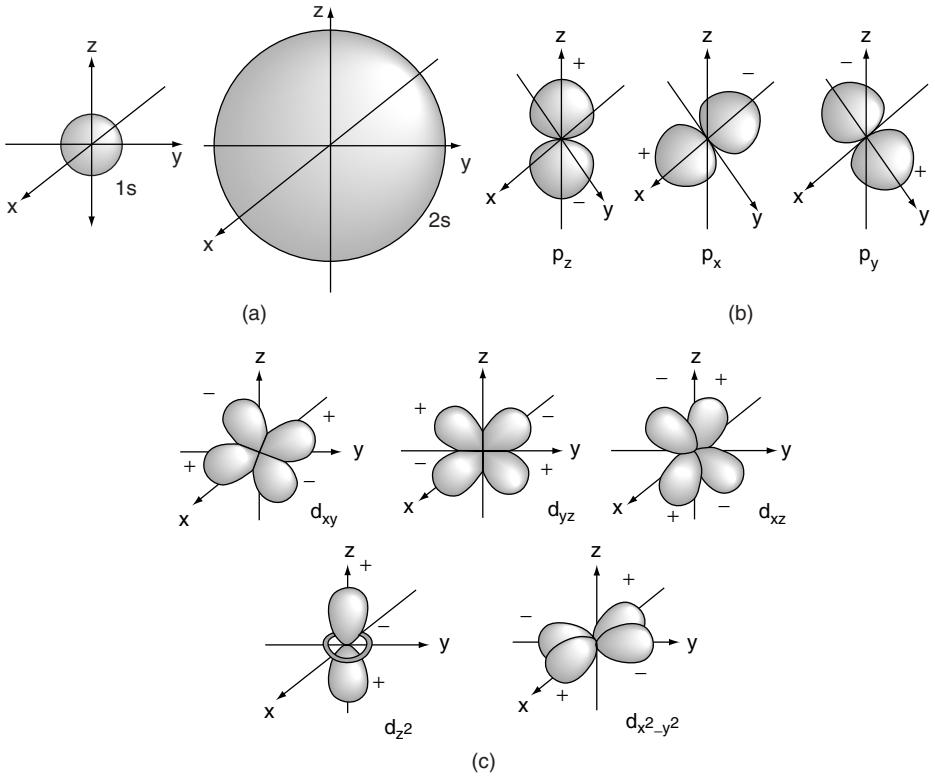

Figure W2.1. Electronic charge distribution in hydrogenlike s, p, and d atomic orbitals. The relative phases of the different lobes of the p and d orbitals are indicated with plus and minus signs. (Adapted from A. L. Companion, *Chemical Bonding*, 2nd ed., McGraw-Hill, 1979.)

It can be seen from Fig. W2.1 that the s orbital is spherically symmetric, whereas the p and d orbitals have preferred directions in space. In particular, the p_x, p_y, and p_z orbitals have two symmetric regions of high probability called *lobes* which are directed along the x, y, and z axes, respectively. The five d orbitals are more complicated. The d_{z^2} orbital has a shape that is similar to the p_z orbital but is much more extended in one direction in space. The four other d orbitals are similar to each other in shape, with four lobes as shown. It should be remembered that each orbital can accommodate no more than two electrons, no matter how many lobes it has. It is important to note that the phase of the wavefunction alternates between being positive in one lobe and negative in the adjacent lobes. The significance of this will become apparent when lobes of orbitals on different atoms overlap. Although rigorously correct in principle only for one-electron atoms and ions, these atomic orbitals are also used for multielectron atoms.

Some of the atomic orbitals that are important for bonding in solid-state materials are listed in Table W2.1. The spin of the electron is $s = \frac{1}{2}$, and in this table the allowed values $+\frac{1}{2}$ and $-\frac{1}{2}$ of the *magnetic quantum number* m_s which correspond to spin-up and spin-down electrons, respectively, are also given. A complete specification of the atomic orbital is therefore given by $\psi(nlm_lm_s)$. The maximum allowed occupancy of an atomic orbital is given by $2(2l + 1)$. A fully occupied or filled orbital or shell

TABLE W2.1 Important Atomic Orbitals for Bonding in Solids

Atomic Orbital	n	l	m_l	m_s	Maximum Occupancy
$1s$	1	0	0	$\pm\frac{1}{2}$	2 $(1s^2)$
$2s$	2	0	0	$\pm\frac{1}{2}$	2 $(2s^2)$
$2p_x$, $2p_y$, $2p_z$	2	1	0, ±1	$\pm\frac{1}{2}$	6 $(2p^6)$
$3s$	3	0	0	$\pm\frac{1}{2}$	2 $(3s^2)$
$3p_x$, $3p_y$, $3p_z$	3	1	0, ±1	$\pm\frac{1}{2}$	6 $(3p^6)$
$3d_{z^2}$, $3d_{x^2-y^2}$, $3d_{xy}$, $3d_{yz}$, $3d_{xz}$	3	2	0, ±1, ±2	$\pm\frac{1}{2}$	10 $(3d^{10})$

therefore contains $2(2l + 1)$ electrons. For example, a filled $3d^{10}$ shell corresponds to 10 electrons occupying all of the $n = 3$, $l = 2$ d orbitals of the atom. The fact that only 10 electrons can occupy an $l = 2$ orbital follows from the *Pauli exclusion principle* (PEP), which states that in a quantum system such as an atom, molecule, or solid, each electron must have a set of quantum numbers which is distinct from that of any other electron in the system.

It should be noted that p and d orbitals are actually linear combinations of wavefunctions with different values of m_l (except for p_z or d_{z^2}, which correspond to $m_l = 0$). The outer or valence electron configurations of neutral atoms in their ground states are presented in Table W2.2.

Two important aspects of the bonding of electrons in neutral atoms are illustrated in Fig. W2.2, where the energies of electrons are shown schematically as a function of the atomic number Z. Starting with the energy levels of the H atom on the left, it can be seen that:

1. Electrons are more tightly bound (i.e., their energies are more negative) as the charge $+Ze$ of the nucleus increases.
2. Electrons in the same shell [i.e., in the $n = 2$ shell ($2s$ and $2p$) or the $n = 3$ shell ($3s$, $3p$, and, for high enough Z, $3d$)] have similar energies which are usually quite different from the energies of electrons in other shells.

It is also clear from Fig. W2.2 that electrons outside closed shells (e.g., the single $3s$ electron of the Na atom with $Z = 11$), are much less strongly bound than those in filled shells. These less strongly bound electrons are the atomic valence electrons, which can participate readily in the hybrid or molecular orbitals described next.

Hybrid Orbitals. As atoms bond to each other in molecules and solids via covalent bonding (i.e., the sharing of electrons), it is often useful to think of the valence electron atomic orbitals having similar energies on a given atom (such as $2s$ and $2p$ or $3s$, $3p$, and $3d$) combining with each other to form *hybrid orbitals*. The bonding between the atoms can then involve the hybrid orbitals in addition to the atomic orbitals. An example of this type of bonding in the CH_4 molecule is discussed later.

TABLE W2.2 Outer or Valence Electron Configurations of Neutral Atoms in Their Ground State

1 H $1s^1$																	2 He $1s^2$
3 Li $2s^1$	4 Be $2s^2$											5 B $2s^2 2p^1$	6 C $2s^2 2p^2$	7 N $2s^2 2p^3$	8 O $2s^2 2p^4$	9 F $2s^2 2p^5$	10 Ne $2s^2 2p^6$
11 Na $3s^1$	12 Mg $3s^2$											13 Al $3s^2 3p^1$	14 Si $3s^2 3p^2$	15 P $3s^2 3p^3$	16 S $3s^2 3p^4$	17 Cl $3s^2 3p^5$	18 Ar $3s^2 3p^6$
19 K — $4s^1$	20 Ca — $4s^2$	21 Sc $3d^1 4s^2$	22 Ti $3d^2 4s^2$	23 V $3d^3 4s^2$	24 Cr $3d^5 4s^1$	25 Mn $3d^5 4s^2$	26 Fe $3d^6 4s^2$	27 Co $3d^7 4s^2$	28 Ni $3d^8 4s^2$	29 Cu $3d^{10} 4s^1$	30 Zn $3d^{10} 4s^2$	31 Ga $3d^{10} 4s^2 4p^1$	32 Ge $3d^{10} 4s^2 4p^2$	33 As $3d^{10} 4s^2 4p^3$	34 Se $3d^{10} 4s^2 4p^4$	35 Br $3d^{10} 4s^2 4p^5$	36 Kr $3d^{10} 4s^2 4p^6$
37 Rb — $5s^1$	38 Sr — $5s^2$	39 Y $4d^1 5s^2$	40 Zr $4d^2 5s^2$	41 Nb $4d^4 5s^1$	42 Mo $4d^5 5s^1$	43 Tc† $4d^5 5s^2$	44 Ru $4d^7 5s^1$	45 Rh $4d^8 5s^1$	46 Pd $4d^{10}$ —	47 Ag $4d^{10} 5s^1$	48 Cd $4d^{10} 5s^2$	49 In $4d^{10} 5s^2 5p^1$	50 Sn $4d^{10} 5s^2 5p^2$	51 Sb $4d^{10} 5s^2 5p^3$	52 Te $4d^{10} 5s^2 5p^4$	53 I $4d^{10} 5s^2 5p^5$	54 Xe $4d^{10} 5s^2 5p^6$
55 Cs — $6s^1$	56 Ba — $6s^2$	57 La $5d^1 6s^2$	72 Hf $4f^{14} 5d^2 6s^2$	73 Ta $4f^{14} 5d^3 6s^2$	74 W $4f^{14} 5d^4 6s^2$	75 Re $4f^{14} 5d^5 6s^2$	76 Os $4f^{14} 5d^6 6s^2$	77 Ir $4f^{14} 5d^7 6s^2$	78 Pt $4f^{14} 5d^9 6s^1$	79 Au $4f^{14} 5d^{10} 6s^1$	80 Hg $4f^{14} 5d^{10} 6s^2$	81 Tl $4f^{14} 5d^{10} 6s^2 6p^1$	82 Pb $4f^{14} 5d^{10} 6s^2 6p^2$	83 Bi $4f^{14} 5d^{10} 6s^2 6p^3$	84 Po $4f^{14} 5d^{10} 6s^2 6p^4$	85 At $4f^{14} 5d^{10} 6s^2 6p^5$	86 Rn $4f^{14} 5d^{10} 6s^2 6p^6$
87 Fr — $7s^1$	88 Ra — $7s^2$	89 Ac $6d^1 7s^2$															

58 Ce† $4f^1 5d^1 6s^2$	59 Pr $4f^3 6s^2$	60 Nd $4f^4 6s^2$	61 Pm $4f^5 6s^2$	62 Sm $4f^6 6s^2$	63 Eu $4f^7 6s^2$	64 Gd $4f^7 5d^1 6s^2$	65 Tb $4f^9 6s^2$	66 Dy $4f^{10} 6s^2$	67 Ho $4f^{11} 6s^2$	68 Er $4f^{12} 6s^2$	69 Tm $4f^{13} 6s^2$	70 Yb $4f^{14} 6s^2$	71 Lu $4f^{14} 5d^1 6s^2$
90 Th $6d^2 7s^2$	91 Pa $5f^2 6d^1 7s^2$	92 U $5f^3 6d^1 7s^2$	93 Np $5d^4 6d^1 7s^2$	94 Pu $5f^6 7s^2$	95 Am $5f^7 7s^2$	96 Cm $5f^7 6d^1 7s^2$	97 Bk $5f^9 7s^2$	98 Cf $5f^{10} 7s^2$	99 Es $5f^{11} 7s^2$	100 Fm $5f^{12} 7s^2$	101 Md $5f^{13} 7s^2$	102 No $5f^{14} 7s^2$	103 Lr $5d^{14} 6d^1 7s^2$

†Some compilations list ^{43}Tc as having a $4d^6 5s^1$ configuration and ^{58}Ce as having a $4f^2 6s^2$ configuration.

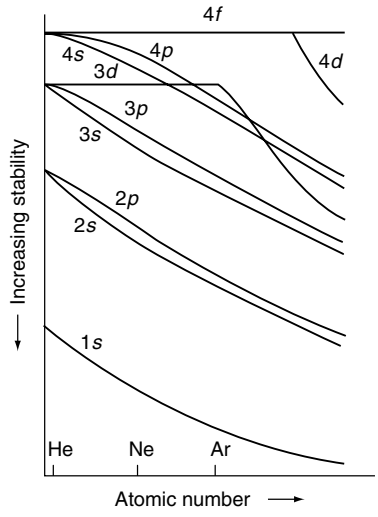

Figure W2.2. Dependence of the energies of electrons in atomic orbitals as a function of the atomic number Z. (Adapted from A. L. Companion, *Chemical Bonding*, 2nd ed., McGraw-Hill, 1979.)

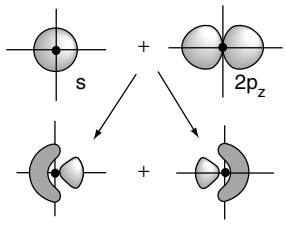

Figure W2.3. Formation of sp hybrid orbitals from s and p atomic orbitals on the same atom. (Adapted from A. L. Companion, *Chemical Bonding*, 2nd ed., McGraw-Hill, 1979.)

Consider now the linear combination of s and p atomic orbitals on the same atom, leading to the formation of two new, equivalent hybrid sp orbitals. This process is shown schematically in Fig. W2.3, where it can be seen that the resulting sp orbitals have the directional properties of the p orbital but are asymmetric. In addition, sp orbitals can also be formed from two s orbitals on the same atom if one of the electrons in an s orbital is first excited or promoted to a higher-lying p orbital. This p orbital then combines with the remaining s orbital to form two sp hybrid orbitals. The energy initially expended to excite the electron from the s to the p orbital can be recovered when the sp hybrid participates in a bond with another atom. This process of the *hybridization* of atomic orbitals can occur in principle because it leads to the formation of strong bonds between atoms and a lowering of the energy of the system.

The directionality of hybridized sp orbitals is due to the interference between the s and p orbitals. For example, the p_z orbital might have a phase corresponding to $\psi_p > 0$ if $z > 0$ and $\psi_p < 0$ if $z < 0$. If the phase of ψ_s is > 0, then $\psi_s + \psi_p$ will be larger (on average) for $z > 0$ than for $z < 0$. On the other hand, $\psi_s - \psi_p$ will be larger for $z < 0$ than for $z > 0$.

The hybrid sp^2 or sp^3 orbitals can be formed similarly when two s and one or two p atomic orbitals, respectively, combine on the same atom. The resulting three equivalent sp^2 hybrid orbitals have *trigonal* planar symmetry, while the four equivalent sp^3 hybrid orbitals have *tetrahedral* symmetry, as shown in Fig. W2.4. The sp^3 orbitals can be written approximately as linear combinations of the s, p_x, p_y, and p_z atomic orbitals (Borg and Dienes, 1992, p. 209). Note that the symmetric arrangements of these sp, sp^2, and sp^3 orbitals in space result from the mutual repulsion of the electrons occupying the orbitals.

Electrons in d atomic orbitals can also participate in the formation of hybrid orbitals. Two important examples are shown in Fig. W2.5. The four dsp^2 hybrid orbitals result from the linear combination of the $d_{x^2-y^2}$, s, p_x, and p_y atomic orbitals on an atom. These dsp^2 hybrids appear similar in shape and symmetry (*square planar*) to the $d_{x^2-y^2}$ orbital but can accommodate four times as many electrons. The six d^2sp^3 hybrid orbitals that result from the linear combination of the $d_{x^2-y^2}$, d_{z^2}, s, p_x, p_y, and p_z atomic orbitals have the symmetry of an *octahedron*, also shown in Fig. W2.5. Additional hybrids involving d orbitals are the three sd^2 orbitals with *trigonal planar* symmetry, the four sd^3 orbitals with *tetrahedral* symmetry, the five dsp^3 orbitals with

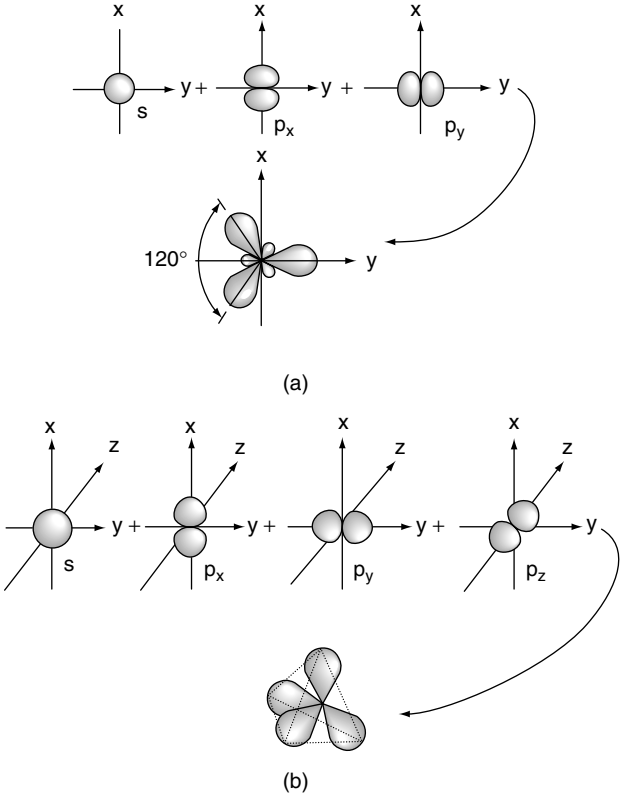

Figure W2.4. Formation of trigonal planar sp^2 and of tetrahedral sp^3 hybrid orbitals from s and p atomic orbitals on the same atom. (Adapted from A. L. Companion, *Chemical Bonding*, 2nd ed., McGraw-Hill, 1979.)

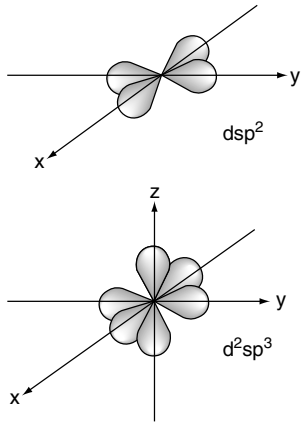

Figure W2.5. Square-planar dsp^2 and octahedral d^2sp^3 hybrid orbitals formed from *s, p*, and *d* atomic orbitals on the same atom. (Adapted from A. L. Companion, *Chemical Bonding*, 2nd ed., McGraw-Hill, 1979.)

TABLE W2.3 Important Hybrid Orbitals Involved in Bonding in Solids

Hybrid Orbital	Symmetry	Coordination Number CN (Number of Bonds)	Examples
sp	Linear	2	Cu_2O
sp^2	Trigonal planar	3	C (graphite)
sp^3	Tetrahedral	4	C (diamond)
dsp^2	Square planar	4	CuCl, CuO
d^2sp^3	Octahedral	6	FeS_2
sp^3d^3f	Cubic	8	

the symmetry of a *trigonal bipyramid*, the six d^4sp orbitals with the symmetry of a *trigonal prism*, and the eight sp^3d^3f orbitals with the symmetry of the vertices of a *cube*. The sd^3 orbitals are involved in the bonding of the Cr^{4+} ion (substituting for Si^{4+}) in tetrahedral coordination with four oxygen ions in crystals such as Mg_2SiO_4, forsterite.

Some of the hybrid orbitals that are important for bonding in solid-state materials are listed in Table W2.3. Also listed are the symmetries of the orbitals, the *coordination number* CN or number of bonds that can be formed by an atom using these orbitals and examples of crystals in which the hybrid orbitals are involved in the bonding. The formation of these hybrid orbitals is only a transitional step in the bonding process, since these orbitals are eigenstates of neither the isolated atom nor the resulting molecule or solid.

Molecular Orbitals and Chemical Bonds. The electrons involved in the chemical bonds between atoms in a molecule no longer occupy specific atomic or hybrid orbitals but rather, occupy *molecular orbitals* (MOs) that are associated with two or more

atoms. The wavefunctions of these MOs can be calculated in principle by solving the Schrödinger equation for the molecule. This is very difficult to do in practice since the potential experienced by the electrons due to the nuclei and the other electrons is not known a priori. As a result, the solutions for the MOs must be obtained in a self-consistent manner.

As an example, consider the simplest *chemical bond*, the bond between two H atoms in the H_2 molecule. In the formation of this molecule, the 1*s* atomic orbitals of each H atom begin to overlap in space as the atoms approach each other. If the phases of the two 1*s* orbitals are the same, *constructive interference* results and a *bonding molecular orbital* (BMO) is produced. If the phases are opposite, *destructive interference* occurs and an *antibonding state* results. In an occupied bonding orbital there is an excess electron density between the nuclei. In an occupied antibonding state there is a diminished electron density between the nuclei.

When the interaction is completed and the H_2 molecule is formed, the two 1*s* orbitals have combined into a single BMO known as a σ_{1s} MO, in which the two electrons are bound equally to both nuclei. In this doubly occupied σ_{1s}^2 MO, shown schematically in Fig. W2.6*a*, the electron charge density midway between the two nuclei is larger than the sum of the original charge densities in the two 1*s* atomic orbitals. When a σ MO is doubly occupied, the two electrons are required by the PEP to have their spins pointing in opposite directions, corresponding to a singlet state.

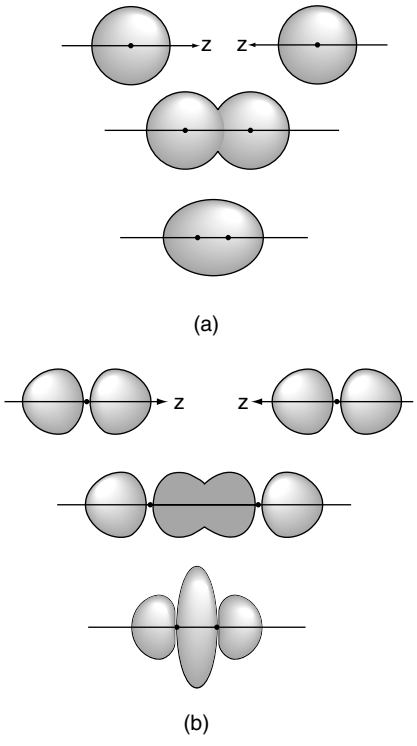

Figure W2.6. Formation of sigma molecular orbitals (σ MOs): (*a*) from two *s* atomic orbitals on different atoms; (*b*) from two p_z atomic orbitals on different atoms. (Adapted from A. L. Companion, *Chemical Bonding*, 2nd ed., McGraw-Hill, 1979.)

Stable molecules have lower energies than the initially isolated atoms. For example, the H_2 molecule is lower in energy than the two isolated H atoms by 4.52 eV (see Fig. 2.1 in the textbook[†]). This energy can be associated with the energy of the covalent H–H σ bond [i.e., $E(\text{H–H}) = 4.52$ eV]. The σ bonds correspond to the buildup of charge between the two atoms involved and are the strongest covalent bonds. Other σ MOs similar to the one shown in Fig. W2.6*a* can also be formed from any of the other atomic ($2s$, $2p$, $3s$, $3p$, $3d$, ...) or hybrid (sp, sp^2, sp^3, dsp^2, d^2sp^3, ...) orbitals. For example, when two $2p_z$ atomic orbitals (see Fig. W2.1) on different atoms overlap head-on and in phase, the σ_{2p} MO shown in Fig. W2.6*b* is formed.

Another important type of molecular orbital is the π MO formed from p or d atomic orbitals. For example, consider again the interaction of two $2p_z$ orbitals on different, identical atoms which are now aligned side by side with their phases synchronized, as shown schematically in Fig. W2.7. Their linear combination is known as a π MO and contains two equivalent regions of high probability, placed symmetrically with respect to the xy plane. When occupied by two electrons, the π MO corresponds to a covalent π bond. The π bonds are in general weaker than σ bonds because their charge distributions are more spread out.

The last type of MO to be discussed here is the δ MO formed from the head-on overlap of two $3d$ orbitals on different, identical atoms. An example is shown in Fig. W2.8, where two $3d_{x^2-y^2}$ orbitals overlap along the z axis. Four equivalent regions of high probability are formed symmetrically with respect to the z axis. When the δ MO contains its two allowed electrons, a covalent δ bond is formed. The δ bonds are in general weaker than σ or π bonds.

The methane molecule, CH_4, provides a simple example of σ bonding. Here four identical σ bonds are formed from the four electrons in the $1s$ H orbitals and the four electrons in each of the sp^3 hybrid orbitals on the C atom. The resulting tetrahedral σ

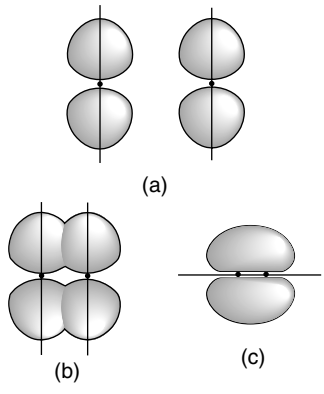

Figure W2.7. Formation of a π molecular orbital (π MO) from two p_z atomic orbitals on different atoms. (Adapted from A. L. Companion, *Chemical Bonding*, 2nd ed., McGraw-Hill, 1979.)

[†] The material on this home page is supplemental to *The Physics and Chemistry of Materials* by Joel I. Gersten and Frederick W. Smith. Cross-references to material herein are prefixed by a "W"; cross-references to material in the textbook appear without the "W."

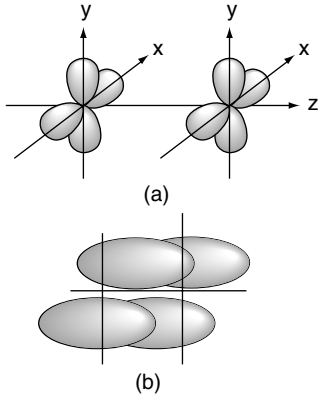

Figure W2.8. Formation of a δ molecular orbital (δ MO) from two $3d_{x^2-y^2}$ atomic orbitals on different atoms. (Adapted from A. L. Companion, *Chemical Bonding*, 2nd ed., McGraw-Hill, 1979.)

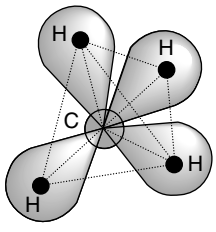

Figure W2.9. Model of the sp^3 tetrahedral σ bonding in the CH_4 (methane) molecule. (Adapted from A. L. Companion, *Chemical Bonding*, 2nd ed., McGraw-Hill, 1979.)

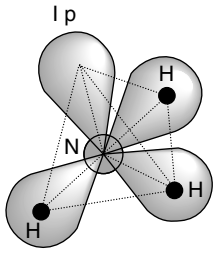

Figure W2.10. Model of the "sp^3 tetrahedral" σ bonding in the NH_3 (ammonia) molecule. (Adapted from A. L. Companion, *Chemical Bonding*, 2nd ed., McGraw-Hill, 1979.)

bonding in CH_4 is shown schematically in Fig. W2.9, where the angles between the σ bonds have the ideal value of 109.47°.

Examination of the bonding in the ammonia molecule, NH_3, illustrates the formation of nonbonding molecular orbitals (NBMOs). In NH_3 three σ bonds are formed between the H atoms and the N atom, as shown in Fig. W2.10. Since N has a valence of 5, the two remaining valence electrons form a *nonbonding*, or *lone pair* (*l p*), *orbital*, also shown in the figure. The NH_3 molecule does not have perfect tetrahedral symmetry since the three σ bonds and the nonbonding orbital are not equivalent. The reality

of the nonbonding orbital can be inferred from its transformation to a σ bond in the ammonium ion, NH_4^+. Here a proton H^+ bonds to the N atom through its attraction to the electrons in the NBMO, thereby converting this orbital into the fourth σ bond in the tetrahedral NH_4^+ ion. Non-bonding orbitals can also play important roles in the bonding of solids. NBMOs participate in hydrogen bonding (see Section 2.7), which helps to stabilize the structures of solid H_2O and DNA.

The interaction of two atomic or hybrid orbitals on different atoms can also lead to the formation of a less stable, *antibonding* MO (ABMO) lying higher in energy than the more stable BMO. In the case of the H_2 molecule the spins of the two electrons in the σ_{1s} BMO are antiparallel, corresponding to a singlet spin state, while in the σ_{1s} ABMO the spins are parallel, corresponding to a triplet spin state. The energy of the σ_{1s} ABMO state lies well above that of the σ_{1s} BMO in H_2, as shown in Fig. 2.1. The triplet state of this molecule is therefore unstable. Examples of stable molecules in which ABMOs are actually occupied by electrons are O_2 and NO.

W2.2 Absence of Covalent Bonding in White Sn (β-Sn) and Pb

The absence of covalent bonding and the existence instead of metallic bonding in the group IV elements white Sn (β-Sn) of row 5 and Pb of row 6 can be attributed to the increased separation between the s and p energy levels in these atoms. This results from the fact that the $5s$ and $6s$ electrons are relatively more strongly bound to the nuclei. It is therefore no longer energetically favorable for the $5s^2p^2$ and $6s^2p^2$ atomic electrons to undergo the hybridizations to $5sp^3$ and $6sp^3$ orbitals, respectively, which are necessary for covalent bonding to occur. Another specific indication of the relatively stronger binding of the $6s$ electrons is that Pb ($6s^26p^2$) often has a valence equal to 2 in solids (e.g., PbO and PbS), indicating that the more strongly bound $6s^2$ electrons do not participate in the bonding.

W2.3 Madelung Energy of Ionic Crystals

A general expression for the electrostatic energy (i.e., the *Madelung energy*) of an ionic crystal is obtained by adding together all the Coulomb interaction energies of the ions. Let z_ie denote the charge of the basis ion at position $\mathbf{s}_i$. Neutrality requires that $\Sigma_{i=1}^n z_i = 0$, where n is the number of ions in a unit cell. The Madelung energy is

$$U = \frac{e^2}{4\pi\epsilon_0}\left(\frac{N}{2}\sum_{i,j}^{n}\frac{z_iz_j}{|\mathbf{s}_i-\mathbf{s}_j|}+\frac{N}{2}\sum_{\mathbf{R}}\sum_{i,j}^{n}\frac{z_iz_j}{|\mathbf{R}+\mathbf{s}_i-\mathbf{s}_j|}\right), \tag{W2.1}$$

where $\mathbf{R}$ is a Bravais lattice vector and N is the number of unit cells in the crystal (assumed to be large). Note that $\mathbf{R} = 0$ is excluded from the sum. In the first sum the term $i = j$ is omitted. The evaluation of this sum is carried out by summing over "shells" of ions of given charge at a given distance from the central ion. The interactions involving the cell at $\mathbf{R} = 0$ are illustrated in Fig. W2.11.

This contribution of the electrostatic interaction to the cohesive energy of an ionic crystal containing $2N$ ions is usually expressed as $U = -NAe^2/4\pi\epsilon_0 d$, where $A > 0$ is the *Madelung constant* and the energy of interaction for a NN cation–anion pair separated by a distance d is $-e^2/4\pi\epsilon_0 d$. For the CsCl, NaCl, and cubic ZnS crystal structures, the values of A are 1.7627, 1.7476, and 1.6381, respectively. On this basis

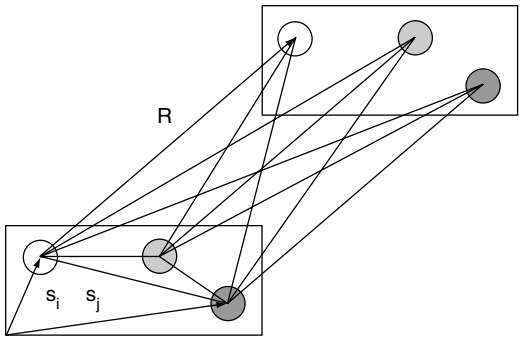

Figure W2.11. The lines within the box correspond to the intrabasis Coulomb interactions (within a given unit cell), while the lines joining the boxes denote the intercell interactions.

the CsCl crystal structure is expected to be slightly more stable than the NaCl crystal structure. Other effects not included here, where ions have been treated as point charges, such as overlap of charge clouds, make the very small calculated difference between the CsCl and NaCl crystal structures rather meaningless. The actual ion–ion interaction is more realistically modeled as the sum of a short-range repulsive potential and the long-range Coulomb interaction,

$$V(r) = \frac{B}{r^m} - \frac{z_c z_a e^2}{4\pi\epsilon_0 r}, \tag{W2.2}$$

where B and m are empirical parameters. Ionic bonding and the Madelung energy are described in more detail in Chapter 13.

W2.4 Hydrogen Bonding in Ice (Solid H_2O)

An example of a crystal in which hydrogen bonding plays an essential role is solid H_2O or ice, where the hydrogen-bonding unit can be written as O–H$\cdots$O. Each oxygen atom in ice is bonded by strong O–H σ bonds with the two H atoms in the H_2O molecule and by weaker H$\cdots$O hydrogen bonds to two H atoms in neighboring H_2O molecules. The arrangement of a central O atom with the four H atoms is tetrahedral (Fig. W2.12). The O–H distance in the O–H bond is about 0.10 nm and is about 0.175 nm in the weaker H$\cdots$O hydrogen bond. Ice has several stable crystal structures which share this tetrahedral orientation of each O atom with respect to the four H atoms surrounding it and also with respect to its four next-NN O atoms. At any given instant, two of the four H atoms in each of these tetrahedral O-centered units in ice are bonded to the central O atom by strong O–H bonds. The other two H atoms are bonded to the central O atom via the weaker H$\cdots$O bonds. Neutron diffraction studies of solid D_2O have shown, however, that the four D (or H) atoms associated with each O atom are constantly changing their positions so that each D (or H) atom spends half of its time in strong σ bonds to the central O atom and the other half in strong σ bonds with a neighboring O atom. These results are consistent with thermodynamic studies of the high residual entropy found in ice crystals, which reflects the "disorder" present in ice even at very low temperatures. Thus while H_2O molecules retain their identity in crystals of ice, it is not possible to say which two of the four H atoms are bonded via strong O–H σ bonds with the central O atom at any instant.

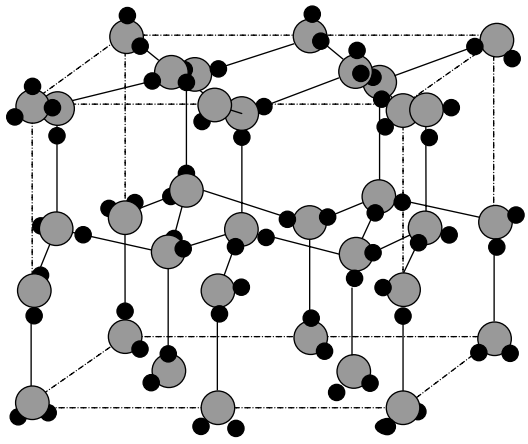

Figure W2.12. Crystal structure of ice (solid H_2O) illustrating hydrogen bonding and showing the disorder in the positions of the protons (H atoms). (From N. H. Fletcher, *The Chemical Physics of Ice*, Cambridge University Press, Cambridge, 1970. Reprinted with the permission of Cambridge University Press.)

The strengths of the two bonds in O–H···O bonding units are quite different, with the much stronger O–H σ bond having an energy $E(\text{O–H}) \approx 4.8$ eV, while the much weaker H···O hydrogen bond has an energy $E(\text{H}\cdots\text{O})$ of only about 0.4 eV. Thus the melting of ice (which involves the weakening of the H···O hydrogen bonds between H_2O molecules) and the boiling of water (which involves the breaking of the hydrogen bonds) occur at relatively low temperatures. The processes of melting and boiling leave the much stronger O–H σ bonds within each H_2O molecule intact.

W2.5 Standard Enthalpies of Formation

Cohesive energies ΔH_c must in general be distinguished from the *standard enthalpies of formation* $\Delta_f H^\circ$ of crystals, which are the changes in enthalpy involved in the formation of a crystal from the constituent elements in their standard states. For example, the standard enthalpy of formation at $T = 0$ K of α-SiO_2(s) (i.e., α-quartz), according to the reaction

$$\text{Si}(s) + \text{O}_2(g) \longrightarrow \text{SiO}_2(s) \tag{W2.3}$$

is equal to the *standard enthalpy change* $\Delta_r H^\circ$ for this reaction. Thus

$$\begin{aligned}\Delta_r H^\circ[\text{SiO}_2(s)] &= \Delta_f H^\circ[\text{SiO}_2(s)] - \Delta_f H^\circ[\text{Si}(s)] - \Delta_f H^\circ[\text{O}_2(g)] \\ &= -905.978 - 0 - 0 = -905.978 \text{ kJ/mol.}\end{aligned} \tag{W2.4}$$

Solid Si(s) and molecular $O_2(g)$ in Eq. (W2.3) are in their standard states with standard enthalpies of formation $\Delta_f H^\circ$, which by definition are equal to zero.[†] The negative

[†] Unless otherwise specified, the standard enthalpies of formation $\Delta_f H^\circ$ used in this section are from the NBS Tables of Chemical Thermodynamic Properties, *J. Phys. Chem. Ref. Data*, **11**, Suppl. 2 (1982).

value for $\Delta_f H^\circ[SiO_2(s)]$ indicates that energy is released when $SiO_2(s)$ is formed from $Si(s)$ and $O_2(g)$ (i.e., the reaction is exothermic).

The cohesive energy of α-SiO_2 at $T = 0$ K according to the reaction

$$SiO_2(s) \longrightarrow Si(g) + 2O(g) \tag{W2.5}$$

is given by

$$\begin{aligned}\Delta H_c[(SiO_2(s)] &= \Delta_f H^\circ[Si(g)] + 2\Delta_f H^\circ[O(g)] - \Delta_f H^\circ[SiO_2(s)] \\ &= 451.29 + 2(246.785) - (-905.978) \\ &= +1850.84 \text{ kJ/mol.}\end{aligned} \tag{W2.6}$$

Here $\Delta_f H^\circ[Si(g)]$ and $\Delta_f H^\circ[O(g)]$ are the standard enthalpies of formation of gas-phase Si and O atoms from solid $Si(s)$ and $O_2(g)$ at $T = 0$ K, respectively.

W2.6 Bond Energies

The cohesive energy $\Delta H_c[SiO_2(s)]$ was shown in Eq. (W2.6) to be equal to 1850.84 kJ/mol. If this energy is assumed to be shared by the $4N_A$ Si–O bonds per mole of $SiO_2(s)$ (N_A is Avogadro's number), the Si–O bond energy is then

$$E(\text{Si–O}) = 4.80 \text{ eV}. \tag{W2.7}$$

The bond energies for single bonds listed in Table W2.4 have been obtained from cohesive energies using this procedure. The crystals whose cohesive energies are used are also listed. The close connection between bond energies and the electronegativity scale is discussed in Section 2.8.

W2.7 Ionization Energies and Electron Affinities

It is clear from the discussions presented in Chapter 2 that the valence electrons play a critical role in the bonding of atoms in solids. Certain important properties and parameters pertaining to atoms (or ions) include ionization energy, electron affinity, valence,

TABLE W2.4 Bond Energies

Bond X–Y	E(X–Y) (eV)	Source
Si–Si	2.34	$Si(s)$
Si–C	3.21	β-SiC(s, cubic)
Si–Ge	2.14	Average of $Si(s)$ and $Ge(s)$
Si–N	3.45	$Si_3N_4(s)$
Si–O	4.80	α-$SiO_2(s)$
C–C	3.70	C(s,diamond)
Ge–Ge	1.95	$Ge(s)$
Ge–O	3.66	$GeO_2(s)$
B–N	3.32	β-BN(s, cubic)
Al–N	2.90	$AlN(s)$
Al–O	5.33	$Al_2O_3(s)$

and atomic or ionic radius. Of these important quantities, only the ionization energies and electron affinities are obtained directly from experiment. The other parameters (i.e., valence, electronegativity, and atomic radii), can only be inferred from the measured properties of atoms.

The first *ionization energy* IE(1) of an atom is the energy required to remove an electron from the neutral atom. IE(1) is also known as the *ionization potential*. Conversely, the *electron affinity* EA of an atom is the energy released when an additional electron is bound to a neutral atom, leading to the formation of a negative ion with charge $-e$. The quantity IE(1) is thus a measure of the ease with which atoms give up electrons (i.e., of their ability to become cations), while EA is the corresponding quantity for the formation of anions.

The reactivity of an atom (i.e., its tendency to combine with other atoms to form a solid), will be greater for atoms with low values of IE(1), such as Li and Na, or with high values of EA, such as F and Cl. Conversely, atoms with high values of IE(1) and low values of EA, such as He and Ne, will tend to be unreactive. Strongly ionic crystals with high ionicities will be formed from pairs of atoms in which one atom has a low IE(1) and the other atom has a high EA. The classic example is NaCl, where the Na atom has IE(1) = 5.15 eV, the Cl atom has EA = 3.62 eV, and the resulting ionicity (see Table 2.6) is $f_i = 0.94$.

Values of IE(1) and IE(2) for the elements are presented in Table 2.9, with IE(1) also shown graphically in Fig. 2.7*a* as a function of atomic number Z. It can be seen that IE(1) generally increases in a given row of the periodic table from left to right as Z, the resulting nuclear charge $+Ze$, and the attractive electrostatic potential felt by the electrons all increase. For example, at the beginning of the second row IE(1) = 5.39 eV for Li with $Z = 3$, while at the end of the same row IE(1) = 21.56 eV for Ne with $Z = 10$. Even though Z and the nuclear charge of atoms also increase down a given group, IE(1) generally decreases in this direction because of the increase in atomic size and the screening of the nuclear charge by electrons in filled inner shells.

The two atoms with the highest first ionization energies, He with IE(1) = 24.59 eV and Ne with IE(1) = 21.56 eV, both have filled outer-electron shells. These two elements, along with the other inert-gas elements in group VIII, are therefore quite stable and unreactive. Only at low temperatures are these elements able to form close-packed crystals in which the neutral atoms are bonded by the weak van der Waals interaction.

Atomic excitation energies can also play a role in chemical bonding, particularly in the formation of hybrid orbitals (see Section W2.1). For example, while IE(1) = 9.32 eV for Be is relatively high due to its $1s^2 2s^2$ filled-shell electron configuration, Be is nevertheless reactive due to the low first excitation energy of about 2.7 eV, which is required to excite a $2s$ electron to a $2p$ atomic level. The $2s$ and the $2p$ electrons of the excited Be atom can then form a pair of sp hybrid orbitals. Under these conditions, the Be atom can be considered to have a valence of 2. These sp orbitals can form bonds with other atoms, such as O in solid BeO, which has the wurtzite (i.e., hexagonal ZnS) crystal structure.

The electron affinities EA for the elements up to $Z = 87$ are presented in Table 2.10 and Fig. 2.7*b*. It can be seen that EA is much smaller than IE(1) for a given atom. Also, EA increases irregularly from left to right across each row of the periodic table, reaching its maximum value for the group VII elements, which require just one additional electron to achieve a filled-shell configuration. All the elements in group II (and

He) with filled s^2 shells and in group VIII with filled s^2 and p^6 shells have negative values of EA. These atoms are therefore unstable as negative ions.

W2.8 Valence

The *valence* z of an atom is usually defined either as the number of electrons it can share with other atoms in covalent bonds or as the number of electrons it can gain or lose in the formation of ionic bonds. These two definitions are often equivalent. For example, the H atom can share its single 1*s* electron in a covalent bond with another H atom or can give it up to a F atom during the formation of an ionic HF molecule. In either case the valence of the H atom is 1.

On the basis of this definition, the most common valences for atoms are given by the number of outer-shell *s* and *p* electrons and so can readily be predicted from their locations in the periodic table. For example, atoms from group I (H, Li, Na, ...) and VII (F, Cl, Br, ...) have valence 1, atoms from group II (Be, Mg, Ca, ...) and VI (O, S, Se, ...) have valence 2, atoms from group III (B, Al, Ga, ...) and V (N, P, As, ...) have valence 3, atoms from group IV (C, Si, Ge, ...) have valence 4, while atoms from group VIII (He, Ne, Ar, ...) have valence 0.

As with many such simple definitions, there are a large number of instructive exceptions. For the transition metals and the noble metals Cu, Ag, and Au, for example, there exist unfilled or just filled 3*d*, 4*d*, or 5*d* shells lying in energy just below the 4*s*, 5*s*, and 6*s* valence electrons. As a result, the *d* electrons may participate in bonding and thereby act as valence electrons. Oxides of the 3*d*, 4*d*, and 5*d* transition metals and of the noble metals illustrate this point since the valences for the metal cations can vary from oxide to oxide, depending on the crystal structure. Some examples are shown in Table W2.5. Note that in Fe_3O_4, magnetite, and Mn_3O_4, hausmannite, the Fe and Mn cations are observed to have two different valence states, +2 and +3, within the same oxide. Also included in the table are oxides of Pb, a metal with a $6s^26p^2$

TABLE W2.5 Valence, Bonding, and Crystal Structures of Some Oxide Crystals

Chemical Formula	Valence z of Metal Ion	Local Atomic Bonding Units	Crystal Structure
Cu_2O	+1	$Cu-O_2$, $O-Cu_4$	Cuprite (BCC)
CuO	+2	$Cu-O_4$, $O-Cu_4$	Tenorite (monoclinic)
MnO	+2	$Mn-O_6$, $O-Mn_6$	NaCl
Mn_2O_3	+3	$Mn-O_6$, $O-Mn_4$	Distorted fluorite
Mn_3O_4	+2 (1)	$Mn-O_4$, $O-Mn^{2+}Mn_3^{3+}$	Hausmannite (tetragonal)
	+3 (2)	$Mn-O_6$	
β-MnO_2	+4	$\approx Mn-O_6$, $O-Mn_3$	Rutile (tetragonal)
FeO	+2	$Fe-O_6$, $O-Fe_6$	NaCl
Fe_3O_4	+2 (1)	$Fe-O_6$, $O-Fe^{2+}Fe_3^{3+}$	Magnetite (inverse spinel)
	+3 (1)	$Fe-O_6$	
	+3 (1)	$Fe-O_4$, $O\text{-}Fe_2^{2+}Fe_2^{3+}$	
Fe_2O_3	+3	$\approx Fe-O_6$, $O-Fe_4$	Corundum (hexagonal)
Pb_2O	+1	$Pb-O_2$, $O-Pb_4$	Cuprite (BCC)
PbO	+2	$Pb-O_4$, $O-Pb_4$	Tetragonal
PbO_2	+4	$Pb-O_6$, $O-Pb_3$	Rutile (tetragonal)

electron configuration. The valence of Pb can vary due to the relatively large energy separation between the $6s^2$ and $6p^2$ atomic energy levels.

The overall electrical neutrality of these oxide crystals requires that the total positive charge of the metal cations be balanced by the total negative charge of the oxygen anions. This balance is clearly reflected in the chemical formulas, assuming a valence of oxygen equal to 2, and also in the local atomic bonding units, $M{-}O_m$ and $O{-}M_n$, where m and n are the integal numbers of NNs of the metal M cations and of the O anions, respectively. The following relationship involving the numbers of NNs and the valences of the metal cation, $z(M)$, and oxygen, $z(O)$, is found to be satisfied for all the oxides listed in the table:

$$mz(O) = nz(M). \tag{W2.8}$$

W2.9 Electronegativity

As an example of the use of Eq. (2.12), that is,

$$E(A{-}B) = \frac{E(A{-}A) + E(B{-}B)}{2} + k(X_A - X_B)^2, \tag{2.12}$$

consider quartz, SiO_2. The single-bond energies $E(Si{-}Si) = 2.34$ eV and $E(Si{-}O) = 4.80$ eV are derived from thermochemical data (see Table W2.4). Using the single-bond energy $E(O{-}O) \approx 1.48$ eV derived from similar data on H_2O and H_2O_2, Eq. (2.12) yields $(X_{Si} - X_O)^2 = 2.89$. It follows that $(X_{Si} - X_O) = -1.70$ since it is known that $X_{Si} < X_O$. To obtain an absolute scale for electronegativity, Pauling assigned the value $X = 4.0$ to F, the most electronegative atom. In this way, the values of electronegativity presented in Table 2.11 have been obtained from Eq. (2.12). From Table 2.11 it can be seen that $(X_{Si} - X_O) = 1.8 - 3.5 = -1.7$, as found above. These values of electronegativity reproduce fairly well the measured single-bond energies $E(A{-}B)$ in a wide range of materials. It should be noted that electronegativities have not been assigned to the elements in group VIII of the periodic table, since these atoms with filled outer-electron shells do not ordinarily form bonds with other atoms.

It can be seen from Tables 2.9, 2.10, and 2.11 that the atoms with the highest electronegativities [i.e., F (4.0), O (3.5), N (3.0), and Cl (3.0)] are also the atoms with some of the highest first ionization energies IE(1) and highest electron affinities EA. This observation is the basis of an alternative electronegativity scale proposed by Mulliken[†] in which these strictly atomic properties have been used to define X, as follows:

$$X = \frac{\text{IE}(1) + \text{EA}}{5.42}. \tag{W2.9}$$

Here IE(1) and EA are expressed in electron volts. When applied to Si and O using the data presented in Tables 2.9 and 2.10, the values $X_{Si} = 1.76$ and $X_O = 2.78$ are obtained from Eq. (W2.9), compared with Pauling's values of 1.8 and 3.5. Mulliken's scale of electronegativity is thus only reasonably consistent with that of Pauling.

Since electronegativity is a parameter that is neither directly measured from experiment nor precisely defined from first principles, it is not surprising that several scales

[†] R. S. Mulliken, *J. Chem. Phys.*, **2**, 782 (1934); **3**, 573 (1935).

of electronegativity exist in addition to those of Pauling and Mulliken. Scales based on different assumptions and using different physical properties as input have been proposed by Sanderson (1976) and by Phillips (1973). The Phillips electronegativity scale for elements in tetrahedrally coordinated environments is based on dielectric properties, in particular the optical dielectric function. The difference between the Pauling and Phillips electronegativities is that Phillips includes the effects of screening of ions by the valence electrons through use of the Thomas–Fermi screening factor $\exp(-k_{TF}r)$, defined in Chapter 7. These electronegativity scales have been found to be particularly useful when applied to physical properties closely related to those used in their definition.

One of the main uses of electronegativities has been in the prediction of the fraction of ionic character of a given bond (i.e., the ionicity of the bond). Ionicities as determined by Phillips have been presented in Table 2.6. With Pauling's definition of electronegativity given in Eq. (2.12), the ionicity of the binary compound AB is defined by Pauling to be

$$f_i(\text{Pauling}) = 1 - \exp\left[-\frac{(X_\text{A} - X_\text{B})^2}{4}\right]. \tag{W2.10}$$

While the Pauling and Phillips definitions of X agree for the elements in the first row of the periodic table, there are significant discrepancies for elements in lower rows.

A serious deficiency of Pauling's and other electronegativity scales is that a single value of X is typically assigned to an atom, independent of its valence in a solid. Since, as shown in Table W2.5, the valence of an atom can vary in different crystal structures, it should be expected that its electronegativity can also vary. Some examples of the dependence of electronegativity on valence include $X_\text{Cu} = 1.9$ for the normal Cu valence state of 1, [i.e., Cu(1)] but $X_\text{Cu} = 2.0$ for Cu(2), as well as $X_\text{Fe} = 1.8$ for Fe(2), but $X_\text{Fe} = 1.9$ for Fe(3).

W2.10 Atomic Radii

For the one-electron atom H and for one-electron ions (He^+, Li^{2+}, Be^{3+}, ...) with nuclear charge +Ze, the expectation value or most probable value for the radius of the electron in its ground-state orbital is given by

$$\langle r\rangle = \frac{a_1}{Z} = \frac{0.0529\ \text{nm}}{Z}, \tag{W2.11}$$

where $a_1 = 4\pi\epsilon_\text{o}\hbar^2/\text{me}^2$ is the first Bohr radius. The inverse dependence of $\langle r\rangle$ on Z reflects the increased attraction of the electron as the nuclear charge +Ze increases. A useful approximate expression for the radius of the outermost electron orbital with principal quantum number n in a neutral atom is

$$\langle r\rangle \approx n^2 a_1/Z_\text{eff}, \tag{W2.12}$$

where $+Z_\text{eff}e$ is the effective nuclear charge experienced by the outermost electrons. Note that Z_eff will be less than Z as a result of the screening of the nuclear charge by the electrons in filled inner shells.

Some general observations concerning the radii presented in Table 2.12 can be made (note that the only anions listed in the table are O^{2-}, S^{2-}, Se^{2-}, Te^{2-}, F^-, Cl^-, Br^-, and I^-; the rest are cations):

1. The radii of atoms and ions increase as one moves down the periodic table, in qualitative agreement with the dependence on the principal quantum number n expressed in Eq. (W2.12).
2. For a given atom the radii r_{cov} and r_{met} are closer in value to each other than to the radius r_{ion} of the same atom.
3. Anions such as O^{2-} or F^- which have gained additional electrons have $r_{ion} > r_{cov}$, whereas the reverse is true for cations such as Be^{2+} and Mg^{2+} which have given up electrons.
4. In the case of Si the three radii presented in Table 2.12 are quite different (i.e., $r_{ion} = 0.040$ nm, $r_{cov} = 0.118$ nm, and $r_{met} = 0.132$ nm). These values apply, in principle, to the Si^{4+} ion in crystalline SiO_2 or in the SiF_4 molecule, to crystalline Si with the diamond crystal structure, and to metal silicides such as V_3Si in which the Si atom has 12 NNs, respectively.
5. Values of r_{ion} will depend on the valence of the ion (see Table 2.4 and also the sources listed in this table for values of r_{ion} for other valences). For example, the values of r_{ion} presented in Table 2.12 for the group V elements are appropriate for the cations N^{5+}, P^{5+}, and so on. The values of r_{ion} for the corresponding anions N^{3-}, P^{3-}, As^{3-}, and Sb^{3-} are much larger (i.e., 0.150, 0.190, 0.200, and 0.220 nm, respectively).

As an example of the use of these radii, consider again SiO_2 and the question of its ionicity. Assuming ionic bonding, the interatomic distance d(Si–O) in SiO_2 is predicted to be equal to the sum of the radii r_{ion} for Si and O (i.e., 0.040 nm + 0.140 nm = 0.180 nm). For the case of covalent bonding, the corresponding sum of the radii r_{cov} is 0.118 nm + 0.066 nm = 0.184 nm. The actual Si–O interatomic distance in SiO_2 has in fact been measured to be 0.161 nm (independent of the actual crystal structure). Therefore, neither the ionic nor the covalent radii listed in Table 2.12 are in fact completely appropriate for SiO_2. The actual situation is that the bonding in SiO_2 is of the mixed ionic–covalent type, with the ionicity of the Si–O bond close to 50%.

The van der Waals atomic radii r_{vdW} are appropriate for neutral atoms with filled outer shells which are effectively in contact with other atoms in solids but which are not bonded to them. In such cases the internuclear distance d(A–B) can be set equal to the sum of the van der Waals radii of atoms A and B. Examples include atoms such as He and Ne in inert-gas crystals, nonbonded atoms in adjacent molecules in molecular crystals such as solid H_2, Cl_2, or solid hydrocarbons, and nonbonded atoms such as C in adjacent planes in the layered crystal graphite. Selected values of r_{vdW} are presented in Table 2.13. These values for r_{vdW} were chosen by Pauling to be essentially the same as the values of r_{ion} for the corresponding anions. This choice should not be surprising since, for example, in the Cl_2 molecule "the bonded (Cl) atom presents the same face to the outside world in directions away from its bond as the ion, Cl^-, does in all directions" (Pauling, 1960, p. 258).

REFERENCES

Borg, R. J., and G. J. Dienes, *The Physical Chemistry of Solids*, Academic Press, San Diego, Calif., 1992.

Burns, G., *Solid State Physics*, Academic Press, San Diego, Calif., 1985.

Companion, A. L., *Chemical Bonding*, McGraw-Hill, New York, 1979.

Cotton, F. A., *Chemical Applications of Group Theory*, 3rd ed., Wiley, New York, 1990.

Jaffe, H. W., *Crystal Chemistry and Refractivity*, 2nd ed., Dover, Mineola, N.Y., 1996.

McKie, D., and C. McKie, *Crystalline Solids*, Wiley, New York, 1974.

Pauling, L., *The Nature of the Chemical Bond*, 3rd ed., Cornell University Press, Ithaca, N.Y., 1960.

Phillips, J. C., *Bonds and Bands in Semiconductors*, Academic Press, San Diego, Calif., 1973.

Sanderson, R. T., *Chemical Bonds and Bond Energy*, 2nd ed., Academic Press, San Diego, Calif., 1976.

PROBLEMS

W2.1 To see how rapidly the summation involved in the calculation of the Madelung energy U converges, use Eq. (W2.1) to calculate the contributions to the summation from the first five shells of ions surrounding a central ion in the NaCl and CsCl crystal structures.

W2.2 Compare the electronegativity difference $|X_C - X_{Si}|$ calculated from Eq. (2.12) and the Si–Si, C–C, and Si–C bond energies listed in Table W2.4 with the Pauling electronegativities for Si and C listed in Table 2.11.

W2.3 Calculate the Pauling ionicities f_i for SiC, GaAs, AlN, ZnS, HgS, and NaCl. Compare your results with the Phillips ionicities listed in Table 2.6 for the same compounds. Are there any systematic differences between the two scales?

CHAPTER W3

Diffraction and the Reciprocal Lattice

W3.1 Voronoi Polyhedra

The concept of Wigner–Seitz cells that is used for periodic structures may be carried over to amorphous solids except that it is given a different name, the *Voronoi polyhedra*. Select a given atom and draw lines to all other atoms. Create bisecting planes perpendicular to each of these lines. All points that can be reached from the given atom without crossing one of these planes lie within the Voronoi polyhedron of that atom. The various Voronoi polyhedra all have differing sizes and shapes, but they do collectively fill all space without overlap. In the case of a periodic solid, translational symmetry demands that the polyhedra all have the same size and shape and they reduce to the Wigner–Seitz cell. An example of a Voronoi polyhedron is given in Fig. W3.1.

W3.2 Molecular Geometry and Basis Structure from Diffraction Data

The location of the diffraction maxima for a crystalline sample provides information that allows determination of the symmetry of the reciprocal lattice and measurement of the lattice constants (i.e., the diffraction pattern specifies the Bravais lattice). In itself, it does not provide information as to the location or identity of the basis atoms comprising the unit cell. Such information, however, may be extracted from an analysis of the intensity of the diffraction spots. Since scattering experiments measure the intensity only and not the phase, the extraction of this information turns out to be a relatively difficult problem. (If an x-ray laser could be constructed, presumably an x-ray hologram could be produced that would contain both amplitude and phase information.) Imagine that one could hypothetically measure the full scattering amplitude, including the phase:

$$\begin{aligned} F(\mathbf{q}) &= \sum_{\mathbf{R}} \sum_{j} f_j(\mathbf{q}) e^{i\mathbf{q}\cdot(\mathbf{R}+\mathbf{s}_j)} \\ &= N \sum_{j} f_j(\mathbf{q}) e^{i\mathbf{q}\cdot\mathbf{s}_j} \sum_{\mathbf{G}} \delta_{\mathbf{q},\mathbf{G}} \end{aligned} \tag{W3.1}$$

and assume that the atomic form factors, $f_j(\mathbf{q})$, are known from independent experiments. Restricting $\mathbf{q}$ to lie on the reciprocal lattice gives

$$F(\mathbf{G}) = N \sum_{j} f_j(\mathbf{G}) e^{i\mathbf{G}\cdot\mathbf{s}_j}. \tag{W3.2}$$

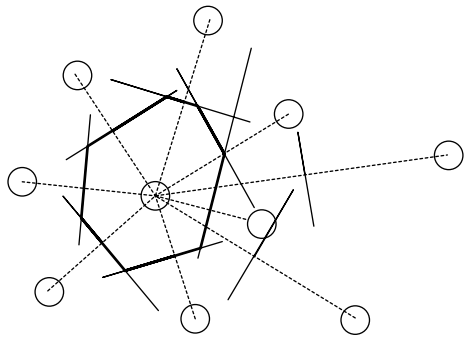

Figure W3.1. Voronoi polyhedron for a given atom in a disordered two-dimensional solid.

The unknowns are the set of vectors $\{\mathbf{s}_j\}$ and the identity of the atoms at each $\mathbf{s}_j$. One way to find them is to construct a mismatch function

$$\Delta(\mathbf{s}_1, \ldots, \mathbf{s}_{n_s}) = \left| F(\mathbf{G}) - N \sum_j f_j(\mathbf{G}) e^{i\mathbf{G}\cdot\mathbf{s}_j} \right|^2 \tag{W3.3}$$

and search for the global minimum. At this minimum, if the data are perfectly accurate, $F = 0$. In principle, if one measures the complex amplitudes at $3n_s$ points in the reciprocal lattice, one should be able to determine the n_s vectors $\{\mathbf{s}_j\}$

In a realistic case, only the intensities,

$$I(\mathbf{G}) = |F(\mathbf{G})|^2, \tag{W3.4}$$

are measured and phase information is lost. Nevertheless, it is still possible to construct a mismatch function

$$\phi(\mathbf{s}_1, \ldots, \mathbf{s}_{n_s}) = \left| I(\mathbf{G}) - N^2 \left| \sum_j f_j(\mathbf{G}) e^{i\mathbf{G}\cdot\mathbf{s}_j} \right|^2 \right|^2 \tag{W3.5}$$

and again search for a minimum by adjusting the set $\{\mathbf{s}_j\}$. The search for this minimum can be an arduous numerical task and limits the size of the unit cell that can be analyzed.

It is useful to introduce the *Patterson function*,

$$P(\mathbf{r}) = \sum_{\mathbf{G}} I(\mathbf{G}) e^{i\mathbf{G}\cdot\mathbf{r}}. \tag{W3.6}$$

Before simplifying this, recall some elementary properties of Fourier series. A periodic function in one dimension may be expanded as a Fourier series [(see Eq. (3.2) in the

textbook[†]]:

$$\phi(x) = \sum_{n=-\infty}^{\infty} \phi_n e^{i(2\pi n/a)x}, \tag{W3.7}$$

where the Fourier coefficients are [see Eq. (3.4)]

$$\phi_n = \frac{1}{a}\int_0^a \phi(x')e^{-i(2\pi n/a)x'}\,dx'. \tag{W3.8}$$

Inserting this into formula (W3.8) yields

$$\phi(x) = \int_0^a \phi(x')\frac{1}{a}\sum_{n=-\infty}^{\infty} e^{i(2\pi n/a)(x-x')}\,dx', \tag{W3.9}$$

implying the formula

$$\delta(x-x') = \frac{1}{a}\sum_{n=-\infty}^{\infty} e^{i(2\pi n/a)(x-x')}. \tag{W3.10}$$

The three-dimensional generalization of the formulas above, involving sums over the reciprocal lattice, leads to the result

$$\delta(\mathbf{r}-\mathbf{r}') = \frac{1}{V_{\mathrm{WS}}}\sum_{G} e^{i\mathbf{G}\cdot(\mathbf{r}-\mathbf{r}')}, \tag{W3.11}$$

where V_{WS} is the volume of the Wigner–Seitz cell.

The Patterson function becomes

$$P(\mathbf{r}) = N^2 \sum_{j,j'} f_{j'}^*(\mathbf{G}) f_j(\mathbf{G}) V_{\mathrm{WS}}\delta(\mathbf{r} - (\mathbf{s}_{j'} - \mathbf{s}_j)). \tag{W3.12}$$

This function is seen to possess sharp peaks whenever the vector $\mathbf{r}$ matches an interatomic displacement vector $\mathbf{s}_{j'} - \mathbf{s}_j$. Thus, by studying the *Patterson map*, one may locate these vectors and attempt to reconstruct the geometric shape of the unit cell.

The use of the methods described above permit one to obtain short-range structural information about the basis of the crystal. This method is of particular value in determining the structure of crystals of biological molecules. It is also of use in studying materials with complex unit cells, such as catalysts. It is of somewhat less use in obtaining information concerning intermediate-range order.

[†] The material on this home page is supplemental to *The Physics and Chemistry of Materials* by Joel I. Gersten and Frederick W. Smith. Cross-references to material herein are prefixed by a "W"; cross-references to material in the textbook appear without the "W."

REFERENCE

Cantor, C. R., and P. R. Schimmel, *Biophysical Chemistry, Part II, Techniques for the Study of Biological Structure and Function*, W. H. Freeman, New York, 1980.

PROBLEM

W3.1 Define the normalized form factor for a basis by $\phi_j(\mathbf{G}) = f_j(\mathbf{G})/\Sigma_i f_i(\mathbf{G})$ and assume that it is positive and does not depend on $\mathbf{G}$. Let the normalized scattering amplitude be given by $\alpha(\mathbf{G}) = F(\mathbf{G})/N\Sigma_i f_i(\mathbf{G})$. Use the *Schwarz inequality*,

$$\left|\sum_i u_i^* v_i\right|^2 \leq \sum_i |u_i|^2 \sum_j |v_j|^2,$$

to prove the following inequalities. Show that

$$|\alpha(\mathbf{G})|^2 \leq 1.$$

Assuming inversion symmetry of the basis, show that

$$|\alpha(\mathbf{G})|^2 \leq \tfrac{1}{2}[1 + \alpha(2\mathbf{G})],$$

which is known as the *Harker–Kasper inequality*. Also prove that

$$|\alpha(\mathbf{G}) \pm \alpha(\mathbf{G}')| \leq [1 \pm \alpha(\mathbf{G} - \mathbf{G}'][1 \pm \alpha(\mathbf{G} + \mathbf{G}')].$$

As an example of the applicability of inequalities to the determination of the phase of the scattering amplitude, suppose it is known that $|\alpha(\mathbf{G})| = 0.8$ and $|\alpha(2\mathbf{G})| = 0.6$. Determine whether $\alpha(2\mathbf{G})$ is positive or negative.

CHAPTER W4

Order and Disorder in Solids

W4.1 Further Discussion of the Random Close-Packing Model

That the *random close-packing model* (RCP) is a more appropriate microscopic structural model for metallic glasses than, for example, a nanocrystalline model can be demonstrated using the results of diffraction studies of metallic glasses. To illustrate the differences between diffraction from amorphous and crystalline materials, the transmission electron-diffraction patterns of thin films of amorphous and recrystallized microcrystalline Fe are shown in Fig. W4.1. These two diffraction patterns can be seen to be qualitatively different, with microcrystalline Fe showing sharp diffraction rings and amorphous Fe showing instead only a few broad, diffuse diffraction rings.

The next-NN atomic configurations which are responsible for the second peak in the reduced radial distribution function $G(r)$ for the metallic glass $Ni_{0.76}P_{0.24}$, shown in Fig. 4.11 of the textbook[†] are shown schematically in Fig. W4.2 for a planar, hexagonal array of close-packed atoms. It should be noted that in the RCP model such an array would not actually be planar, and the corresponding distances would be somewhat less than $\sqrt{3}$ and 2. These distances are actually close to those expected in icosahedra (see Fig. 1.11). The overlapping structure of this second peak is thus a characteristic signature of metallic glasses with an RCP structure and may be considered to provide indirect evidence for the existence of icosahedral clusters of atoms in metallic glasses.

The fact that the RCP structural model is successful in predicting that two distinct types of atomic configurations contribute to the second peak in the radial distribution function $g(r)$ provides strong evidence for its validity. In contrast, nanocrystalline models of metallic glasses are unable to explain the details of the observed $g(r)$. These models, based on the existence of nanocrystallites in the metallic glass, are able to predict the sharpness of the first peak. They predict, however, that the second and higher peaks will be sharper than actually observed. Thus the intermediate-range order predicted to extend beyond NN atoms by nanocrystalline models is not generally observed in amorphous solids.

One final observation concerning the RCP model is that it can be said to represent an "ideal" close-packed amorphous solid. This observation follows from the fact that in the RCP model the spheres are packed as densely as possible, consistent with the nature of amorphous solids. Achieving a higher density of packing of hard spheres would

[†] The material on this home page is supplemental to *The Physics and Chemistry of Materials* by Joel I. Gersten and Frederick W. Smith. Cross-references to material herein are prefixed by a "W"; cross-references to material in the textbook appear without the "W."

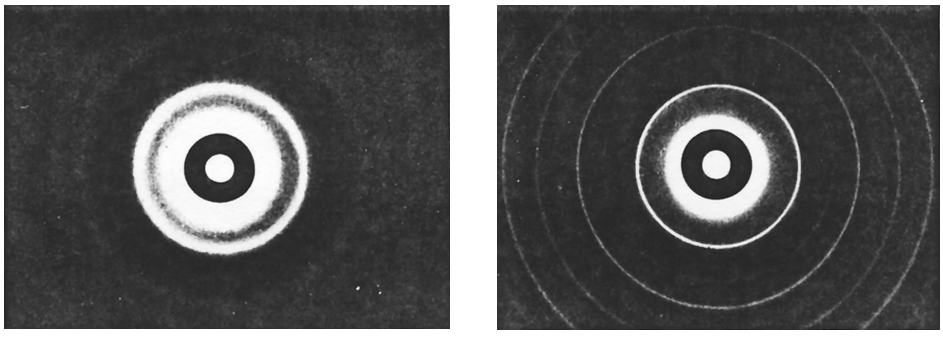

(a) (b)

Figure W4.1. Transmission electron-diffraction patterns for thin films of (*a*) amorphous and (*b*) recrystallized microcrystalline Fe. (From T. Ichikawa, Phys. Stat. Solidi a, 19, 707 (1973). Reprinted by permission of Wiley-VCH Verlag Berlin.)

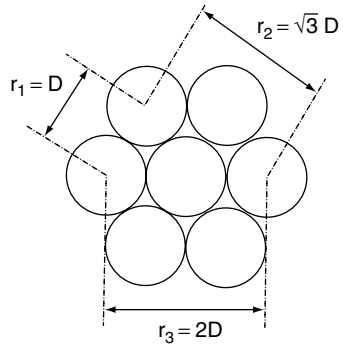

Figure W4.2. NN and two types of next-NN configurations of atoms in metallic glasses. A planar, hexagonal array of close-packed atoms is shown.

require that a form of crystallization occur locally, corresponding to the nucleation of clusters of spheres with either the FCC or HCP crystal structures or as icosahedra. The resulting solid would then, however, no longer be completely amorphous. A lower density of packing could easily be achieved by removing spheres, thereby creating vacancies and causing the resulting structure to be even more disordered than the ideal amorphous solid represented by the RCP model.

Even though it can be argued that the RCP model is in some sense ideal, it nevertheless defines an amorphous structure only in a statistical way. This follows from the fact that there can be an infinite number of possible amorphous solids with structures that are consistent with the RCP structural model, whereas a crystalline solid has a single, unique structure.

W4.2 Further Discussion of the Continuous Random Network Model

In the case of amorphous carbon, a-C, there is little doubt that a *continuous random network model* (CRN) is appropriate, but there is great difficulty in knowing how to

construct such a model. The difficulty resides in the fact that there are two common forms of crystalline C: graphite, based on $C-C_3$ trigonal bonding units, and diamond, based on $C-C_4$ tetrahedral bonding units. Both graphitelike and diamondlike types of SRO are believed to be present in a-C.

The validity of CRN models for amorphous solids such as a-Si, a-SiO_2, and a-Ge has been verified by comparing the experimentally determined radial distribution functions with those calculated from "ball-and-stick" CRN models constructed by hand and "relaxed" by computer to minimize network strain. The agreement between experiment and the predictions of the CRN models has been found to be impressive.[†] These comparisons also demonstrate that nanocrystalline models for amorphous covalent (or nearly covalent) glasses are inappropriate, as was also found to be the case for metallic glasses.

W4.3 Illustrations of the Law of Mass Action

For Schottky defects (i.e., vacancies) the process of creating a vacancy V_A without a corresponding interstitial I_A involves the movement of an A atom from a lattice site to a surface site (i.e., S_A). The defect reaction for this process is

$$A \longleftrightarrow V_A + S_A. \tag{W4.1}$$

At the same time, an existing surface atom S_A is covered. The net effect is that an additional bulk atom is created below the surface, yielding

$$S_A \longleftrightarrow A. \tag{W4.2}$$

The net defect reaction is therefore the sum of reactions (W4.1) and (W4.2); that is,

$$0 \longleftrightarrow V_A. \tag{W4.3}$$

The law of mass action for the creation of a Schottky defect is therefore

$$a_L(V) = \frac{N_L(V)}{N_L(A)} = K_V(T), \tag{W4.4}$$

which yields

$$N_L(V) = N_L(A) \exp\left(-\frac{\Delta G_r}{k_B T}\right). \tag{W4.5}$$

The process of creating an interstitial without a corresponding lattice vacancy involves the movement of a surface atom S_A into an empty interstitial position V_I, thus creating an interstitial A atom I_A. At the same time, a new surface atom is uncovered. The resulting interstitial number or concentration is given by

$$N_I(A) = N_I(V) \exp\left(-\frac{\Delta G_r}{k_B T}\right). \tag{W4.6}$$

[†] An excellent summary of these comparisons appears in Zallen (1983, Chap. 2).

When taken together, the processes just described for the creation of a Schottky defect and of an interstitial atom are equivalent to the creation of a Frenkel defect (i.e., a vacancy–interstitial pair). It can be shown that the equilibrium constant for Frenkel defect formation K_F is equal to $K_V K_I$ (i.e., to the product of the equilibrium constants K_V for vacancy formation and K_I for interstitial formation).

The generation of charged defects (i.e., ionized donors and acceptors in semiconductors) is described in detail in Chapter 11. The requirement of electrical neutrality plays an important role in determining the concentrations of ionized dopant atoms and, consequently, of charge carriers.

W4.4 Nonstoichiometry

Solids such as SiO_2, NaCl, V_3Si, and $YBa_2Cu_3O_7$, which have a well-defined chemical formula are stoichiometric compounds. When the composition of a solid deviates from the standard chemical formula, the resulting solid is said to be *nonstoichiometric*, and as a result, defects are present. Examples include SiO_{2-x}, Fe_3O_{4-x}, $YBa_2Cu_3O_{7-x}$, and $Mn_{1-x}O$. Additional examples of nonstoichiometric solids are discussed in Chapter 4, with further examples presented in Chapters 11 to 18, where specific classes of materials are addressed.

Nonstoichiometry often results when a solid comes into equilibrium with external phases. For example, the first three solids just listed are all oxygen-deficient, possibly resulting from being in equilibrium with an oxygen-deficient atmosphere either during growth or during subsequent processing at elevated temperatures. The fourth example, $Mn_{1-x}O$, is likely to have been formed in an oxygen-rich atmosphere. In all four cases, the actual composition of the solid is determined by the oxygen activity of the ambient (i.e., the partial pressure of O_2), by the temperature, and by the chemical potentials of the components.

Nonstoichiometry and the existence of point defects in a solid are often closely related. Anion vacancies are the source of the nonstoichiometry in SiO_{2-x}, Fe_3O_{4-x}, and $YBa_2Cu_3O_{7-x}$, and cation vacancies are present in $Mn_{1-x}O$. In some cases the vacancies within the structure are ordered. Nonstoichiometry in ionic solids usually corresponds to at least one of the ions occurring in more than one charge state. For example, if all the oxygen ions in $Mn_{1-x}O$ are O^{2-}, then for every Mn^{2+} vacancy in the solid there must also be two Mn^{3+} ions present to preserve overall electrical neutrality.

REFERENCE

Zallen, R., *The Physics of Amorphous Solids*, Wiley, New York, 1983.

CHAPTER W5

Phonons

5.1 Monatomic Lattice with Random Interactions

In a disordered material the periodicity of the solid is broken, and this affects the phonon spectrum. Various types of disorder are possible, including bond disorder, isotopic mass disorder, or a breaking of the lattice periodicity. In this section a simple model exhibiting bond disorder is studied: a monatomic lattice in one dimension with nearest-neighbor (NN) interactions but with random spring constants. These are assumed to have only two values, K_A or K_B, with probabilities p_A and $p_B = 1 - p_A$, respectively.

The squares of the mode frequencies, ω_μ^2, are determined by finding the eigenvalues of the random matrix $\mathbf{D}$ defined by

$$D_{n,n} = \frac{K_n + K_{n-1}}{M}, \qquad D_{n,n+1} = -\frac{K_n}{M}, \qquad D_{n,n-1} = -\frac{K_{n-1}}{M}, \tag{W5.1}$$

where $n = 1, 2, \ldots, N$ labels the atoms in the monatomic lattice (with the subscript convention $0 \to N$ and $N + 1 \to 1$). All other matrix elements are zero. Rapid numerical techniques are available for diagonalizing such matrices.

The density of states (per unit frequency) per atom,

$$\rho(\omega) = \frac{1}{N} \sum_\mu \delta(\omega - \omega_\mu), \tag{W5.2}$$

will be compared with the corresponding function expected for the uniform lattice with an average spring constant $K = p_A K_A + p_B K_B$. The density of states per atom for the uniform lattice is obtained using the dispersion relation of the book,[†] Eq. (5.7). Thus

$$\begin{aligned} \rho(\omega) &= \frac{1}{N} \int_{-\pi/a}^{\pi/a} \frac{L dk}{2\pi} \delta\left(\sqrt{\frac{4K}{M}} \left| \sin \frac{ka}{2} \right| - \omega \right) \\ &= \frac{2}{\pi} \frac{1}{\sqrt{(4K/M) - \omega^2}}, \end{aligned} \tag{W5.3}$$

[†] The material on this home page is supplemental to *The Physics and Chemistry of Materials* by Joel I. Gersten and Frederick W. Smith. Cross-references to material herein are prefixed by a "W"; cross-references to material in the textbook appear without the "W."

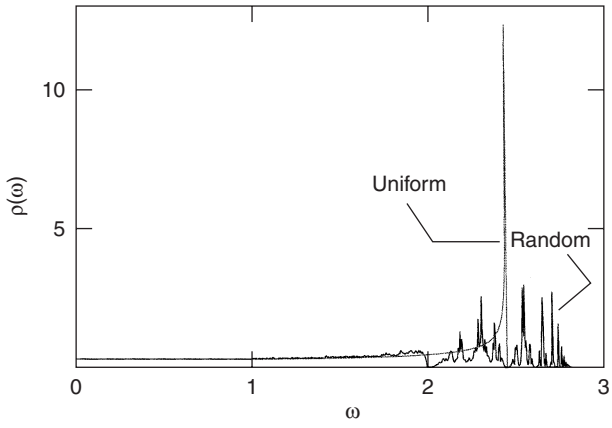

Figure W5.1. Phonon densities of states for random and uniform lattices. The calculation was performed with $N = 125$.

where $\omega^2 \leq 4K/M$. The results are presented in Fig. W5.1, where units are chosen so that $M = 1$, $K_A = 1$, $K_B = 2$, and $p_A = p_B = 0.5$. An $N = 125$ lattice was used and an ensemble average over different sets of random bonds was made. The frequencies corresponding to the pure K_A or pure K_B lattices are $\omega_A = 2(K_A/M)^{1/2}$ and $\omega_B = 2(K_B/M)^{1/2}$ (2 and 2.828 in the figure). The differences between the random and uniform lattice (with $K = 0.5K_A + 0.5K_B = 1.5$) are striking. At low frequencies the density of states follows the trend expected for the infinite uniform lattice. In the high-frequency region ($\omega_A < \omega < \omega_B$) there is a irregular structure for the density of states. It is found that as N increases, the high-frequency structure remains basically unchanged, except for the appearance of finer irregular features.

W5.2 Debye–Waller Factor

In this section the derivation of the Debye–Waller factor is sketched. For the sake of simplicity consider a monatomic lattice of atoms with mass M. Let the instantaneous position of the atom be denoted by $\mathbf{R} + \mathbf{u}(\mathbf{R}, t)$. The electron density is

$$n(\mathbf{r}, t) = n_{\text{atom}}(\mathbf{r} - \mathbf{R} - \mathbf{u}(\mathbf{R}, t)). \tag{W5.4}$$

The analysis proceeds as in Chapter 3. The scattering amplitude $F(\mathbf{q}, t)$ is

$$F(\mathbf{q}, t) = f_{\text{atom}}(\mathbf{q}) \sum_{\mathbf{R}} \exp[-i\mathbf{q} \cdot (\mathbf{R} + \mathbf{u}(\mathbf{R}, t))] = f_{\text{atom}}(\mathbf{q}) S(\mathbf{q}, t). \tag{W5.5}$$

When evaluated at a reciprocal lattice vector $\mathbf{q} = \mathbf{G}$, the geometric structure factor becomes

$$S(\mathbf{G}, t) = \sum_{\mathbf{R}} \exp[-i\mathbf{G} \cdot \mathbf{u}(\mathbf{R}, t)]. \tag{W5.6}$$

The strength of the coherent x-ray scattering is proportional to the absolute square of $S(\mathbf{G})$. It is useful to work in the *interaction representation* of quantum mechanics, in

which the operators are not time dependent. Begin by writing

$$|S(\mathbf{G})|^2 = \sum_{\mathbf{R}\mathbf{R}'} \exp[i\mathbf{G}\cdot(\mathbf{u}(\mathbf{R}') - \mathbf{u}(\mathbf{R}))]. \tag{W5.7}$$

In the absence of fluctuations, this would be N^2. In the presence of fluctuations, expand the displacements as a sum of phonon modes [see Eq. (W5A.5)]:

$$\mathbf{u}(\mathbf{R}) = \sqrt{\frac{1}{N}} \sum_{\vec{Q}} \hat{\epsilon}_{\mathbf{Q}} [u_{\mathbf{Q}} \exp(i\mathbf{Q}\cdot\mathbf{R}) + u^{+}_{\mathbf{Q}} \exp(-i\mathbf{Q}\cdot\mathbf{R})], \tag{W5.8}$$

where $u_{\mathbf{Q}}$ and $\hat{\epsilon}_{\mathbf{Q}}$ are the amplitude and polarization of a phonon with wave vector $\mathbf{Q}$ and frequency $\omega_{\mathbf{Q}}$. It follows that

$$|S(\mathbf{G})|^2 = \sum_{\mathbf{R}\mathbf{R}'} \prod_{\mathbf{Q}} \exp\left(\frac{i}{\sqrt{N}} \mathbf{G}\cdot\hat{\epsilon}_{\mathbf{Q}} \{u_{\mathbf{Q}}[\exp(i\mathbf{Q}\cdot\mathbf{R}') - \exp(i\mathbf{Q}\cdot\mathbf{R})] + \text{h.c.}\}\right), \tag{W5.9}$$

where h.c. is the Hermitian conjugate of the first term. This must be averaged over a thermal distribution of phonons. The exponential is expanded into a power series. Note that $u_{\mathbf{Q}}$ is a Gaussian random variable with the first two moments being

$$\langle u_{\mathbf{Q}} \rangle = 0, \qquad \langle |u_{\mathbf{Q}}|^2 \rangle = \frac{N\hbar}{2M\omega_{\mathbf{Q}}} \left(n_{\mathbf{Q}} + \frac{1}{2}\right). \tag{W5.10}$$

Averages of products of Gaussian random variables are expressible in terms of the first two moments alone,

$$\langle u_{\mathbf{Q}_1} u_{\mathbf{Q}_2} u_{\mathbf{Q}_3} u_{\mathbf{Q}_4} \rangle = \langle u_{\mathbf{Q}_1} u_{\mathbf{Q}_2} \rangle \langle u_{\mathbf{Q}_3} u_{\mathbf{Q}_4} \rangle + \langle u_{\mathbf{Q}_1} u_{\mathbf{Q}_3} \rangle \langle u_{\mathbf{Q}_2} u_{\mathbf{Q}_4} \rangle + \langle u_{\mathbf{Q}_1} u_{\mathbf{Q}_4} \rangle \langle u_{\mathbf{Q}_2} u_{\mathbf{Q}_3} \rangle, \tag{W5.11}$$

where the expansion includes all distinct permutations of the indices. Thus only even powers in the power series are nonvanishing. The series may then be resummed to give

$$\langle |S(\mathbf{G})|^2 \rangle = \sum_{\mathbf{R}\mathbf{R}'} \prod_{\mathbf{Q}} \exp\left\{-\frac{2}{N} (\mathbf{G}\cdot\hat{\epsilon}_{\mathbf{Q}})^2 |u_{\mathbf{Q}}|^2 [1 - \cos \mathbf{Q}\cdot(\mathbf{R} - \mathbf{R}')]\right\}. \tag{W5.12}$$

In a three-dimensional crystal the term $[1 - \cos(\cdot)]$ averages to $\frac{1}{2}$ and one obtains

$$\langle |S(\mathbf{G})|^2 \rangle = N^2 \exp\left[-\sum_{\mathbf{Q}} (\mathbf{G}\cdot\hat{\epsilon}_{\mathbf{Q}})^2 \frac{\left(n_{\mathbf{Q}} + \frac{1}{2}\right)\hbar}{M\omega_{\mathbf{Q}}}\right] = N^2 e^{-2W}. \tag{W5.13}$$

This gives the desired expression for the Debye–Waller factor, $\exp(-2W)$. In the high-temperature limit, the Bose–Einstein distribution function may be replaced by $n_{\mathbf{Q}} \to k_B T/\hbar\omega_Q$. It is also possible to use the Debye theory, used in Chapter 5 to evaluate the specific heat, to evaluate the Debye–Waller factor.

Appendix W5A: Quantization of Elastic Waves

In this appendix the classical elastic field will be *quantized*, that is, replaced by a set of phonons. It is a twofold procedure. First the elastic field is replaced by a set of independent harmonic oscillators, one for each normal mode. Then each of these is quantized in the same way that the simple harmonic oscillator is quantized. For the sake of simplicity, attention is restricted in this appendix to the one-dimensional monatomic lattice.

The starting point is the classical equation of motion for the particle displacements, given by Eq. (5.2):

$$M\ddot{u}_n = K(u_{n+1} - u_n) - K(u_n - u_{n-1}), \qquad n = 1, 2, \ldots, N. \tag{W5A.1}$$

The energy of the system, or Hamiltonian, is the sum of the kinetic energy and the potential energy:

$$H = \frac{1}{2M}\sum_{n=1}^{N} p_n^2 + \frac{K}{2}\sum_{n=1}^{N}(u_{n+1} - u_n)^2. \tag{W5A.2}$$

Here p_n represents the momentum conjugate to u_n. The equation of motion is obtained from Hamilton's equations of mechanics:

$$\dot{u}_n = \frac{\partial H}{\partial p_n} = \frac{p_n}{M}, \tag{W5A.3}$$

$$\dot{p}_n = -\frac{\partial H}{\partial u_n} = K(u_{n+1} + u_{n-1} - 2u_n). \tag{W5A.4}$$

Eliminating p_n from these equations gives Eq. (W5A.1).

Introduce a new set of coordinates $\{Q_j\}$ and momenta $\{P_j\}$, which we call *normal-mode coordinates* and *momenta*, defined by

$$u_n = \frac{1}{\sqrt{N}}\sum_{j=1}^{N} Q_j e^{inak_j}, \tag{W5A.5}$$

$$p_n = \frac{1}{\sqrt{N}}\sum_{j=1}^{N} P_j e^{inak_j}, \tag{W5A.6}$$

where a is the lattice constant and k_j is defined in Eq. (5.4). It is convenient to impose periodicity and define $Q_{N+j} = Q_j$ and $P_{N+j} = P_j$. Two powerful identities may be proved. The first involves a sum over lattice positions:

$$\sum_{n=1}^{N} \exp[ina(k_j - k_l)] = N\delta_{j,l}, \tag{W5A.7}$$

and the second involves a sum over modes:

$$\sum_{j=1}^{N} \exp[ik_j a(n - m)] = N\delta_{n,m}. \tag{W5A.8}$$

As Figs. W5A.1 and W5A.2 show, the sums will be zero when summed either over lattice positions with a given wave vector or summed over modes with a given lattice position. The one exception to both cases is when the lattice position is zero or when the wave vector is zero. For u_n and p_n to be real numbers, one can show from Eqs. (W5A.5) and (W5A.6) that

$$Q^*_{N-j} = Q^*_{-j} = Q_j, \qquad P^*_{N-j} = P^*_{-j} = P_j. \tag{W5A.9}$$

By making use of the identities (W5A.7) and (W5A.8), the Hamiltonian may be rewritten in terms of the P's and Q's:

$$H = \sum_{j=1}^{N} \left(\frac{P^*_j P_j}{2M} + \frac{M\omega_j^2}{2} Q^*_j Q_j \right). \tag{W5A.10}$$

In this form, the Hamiltonian is expressed as the sum of N independent harmonic oscillators, each representing one of the normal modes of the lattice. The P_j and Q_j

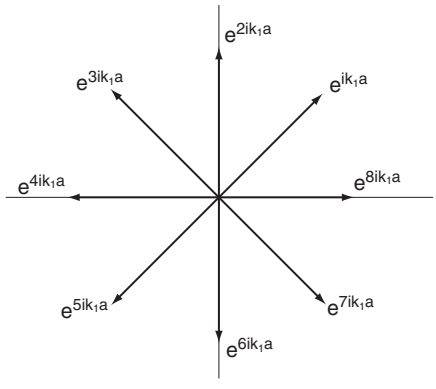

Figure W5A.1. Representation of the sum over lattice positions given in Eq. (W5A.7). Note that the vector sum is zero. In this diagram $N = 8$ and $j - l = 1$.

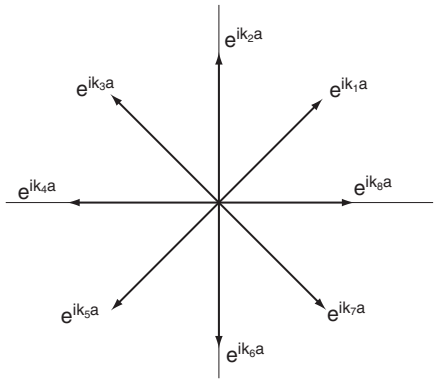

Figure W5A.2. Representation of the sum over modes given in Eq. (W5A.8). Note that the vector sum is zero. In this diagram $N = 8$ and $n - m = 1$.

coordinates are also expressible in terms of p_n and u_n:

$$Q_j = \frac{1}{\sqrt{N}} \sum_{n=1}^{N} u_n e^{-inak_j}, \tag{W5A.11}$$

$$P_j = \frac{1}{\sqrt{N}} \sum_{n=1}^{N} p_n e^{-inak_j}. \tag{W5A.12}$$

The quantization procedure is straightforward. One regards $\{u_n\}$ and $\{p_n\}$ as sets of quantum-mechanical operators obeying the usual equal-time commutation relations (see Appendix WC):

$$[u_n, u_m] = 0, \qquad [p_n, p_m] = 0, \qquad [p_n, u_m] = -i\hbar\delta_{m,n}. \tag{W5A.13}$$

Hamilton's equations of motion are regarded as equations governing the time evolution of these operators. The Hamiltonian H, given above, is now an operator. Using the commutation rules, it can be shown that

$$[P_j, Q_l] = -i\hbar\delta_{j,l}, \qquad [P_j, P_l] = 0, \qquad [Q_j, Q_l] = 0. \tag{W5A.14}$$

A further simplification of the problem results from introducing specific linear combinations of the P's and Q's,

$$a_j = \frac{1}{\sqrt{2M\omega_j\hbar}}(M\omega_j Q_j + iP_j), \qquad a_j^+ = \frac{1}{\sqrt{2M\omega_j\hbar}}(M\omega_j Q_{N-j} - iP_{N-j}). \tag{W5A.15}$$

These operators are referred to as *ladder operators*. They obey the commutation rules

$$[a_j, a_l] = 0, \qquad [a_j^+, a_l^+] = 0, \qquad [a_j, a_l^+] = \delta_{j,l}. \tag{W5A.16}$$

The P and Q operators become

$$Q_j = \sqrt{\frac{\hbar}{2M\omega_j}}(a_j + a_{-j}^+), \tag{W5A.17}$$

$$P_j = -i\sqrt{\frac{M\hbar\omega_j}{2}}(a_j - a_{-j}^+). \tag{W5A.18}$$

The Hamiltonian finally becomes

$$H = \sum_{j=1}^{N} \hbar\omega_j (a_j^+ a_j + \tfrac{1}{2}). \tag{W5A.19}$$

The quantity $n_j = a_j^+ a_j$ is the number operator for phonons in mode j. Its eigenvalues are the non negative integers $0, 1, 2, \ldots$. Its eigenfunctions are states with a definite

number of phonons of mode j. Thus a given phonon mode may be unoccupied, have one phonon, two phonons, and so on. The corresponding energy is

$$E_j = \left(n_j + \tfrac{1}{2}\right)\hbar\omega_j. \tag{W5A.20}$$

The problem has thus been reduced to a system of noninteracting harmonic oscillators, each corresponding to a different mode, j. Note the presence of energy even in the absence of phonons ($n_j = 0$). This is called *zero-point energy*.

Appendix W5B: Dispersion Relations in the General Case

Consider a crystal structure and select any point O in the crystal to serve as an origin. Translate it through the Bravais lattice, thereby replicating O through the set of translation vectors $\{\mathbf{R}\}$. Denote the replicated points by $\{O_R\}$. The set of points in space which are closer to O than any other O_R is called the *Wigner–Seitz* (WS) *cell* and has a polyhedral shape. (Note that this definition is slightly more general than the previous definition of the WS cell in Chapter 3. in that point O need not be on an atom). Due to the periodicity of the lattice, the WS cell contains exactly s atoms. Around each of the origins $\{O_R\}$ one may similarly construct a WS cell, thereby filling all of space.

In a phonon excitation the amplitude of vibration of atoms in a neighboring cell $\{O_R\}$ is simply related to the excitations of atoms in the base cell O:

$$\mathbf{u}^\sigma(\mathbf{R}) = \mathbf{u}^\sigma \exp(i\mathbf{k}\cdot\mathbf{R}), \qquad \sigma = 1, 2, \ldots, s. \tag{W5B.1}$$

Rather than using the spring constants directly, note that the expression for the elastic energy [see Eq. (5A.2)] is written as a quadratic form. This permits the introduction of an alternative set of elastic coefficients and expressing the energy in a simpler form. Let the αth component of the displacement of the σth atom of cell $\mathbf{R}$ be denoted by $u_\alpha^\sigma(\mathbf{R})$. Expand the elastic energy of the crystal in terms of the atomic displacements and truncate the expansion at second order, a procedure known as the *harmonic approximation*. The zeroth-order term is just a constant added to the energy and may be neglected. The first-order term vanishes because the elastic energy has a minimum at the equilibrium state. The second-order term is thus

$$U = \frac{1}{2}\sum_{\sigma,\sigma'}\sum_{\alpha,\alpha'}\sum_{\mathbf{R},\mathbf{R}'} u_\alpha^\sigma(\mathbf{R}) L_{\alpha,\alpha'}^{\sigma,\sigma'}(\mathbf{R}-\mathbf{R}') u_{\alpha'}^{\sigma'}(\mathbf{R}'), \tag{W5B.2}$$

where the set of elastic coefficients is defined in terms of the second derivatives:

$$L_{\alpha,\alpha'}^{\sigma,\sigma'}(\mathbf{R}-\mathbf{R}') = \frac{\partial^2 U}{\partial u_\alpha^\sigma(\mathbf{R})\partial u_{\alpha'}^{\sigma'}(\mathbf{R}')}. \tag{W5B.3}$$

The indices σ and σ' range over $\{1, 2, \ldots, s\}$, and the indices α and α' over $\{1, 2, 3\}$. Note that invariance of the crystal under Bravais lattice translations dictates that L depends only on $\mathbf{R}-\mathbf{R}'$. One sees from the definition that L is symmetric, that is,

$$L_{\alpha,\alpha'}^{\sigma,\sigma'}(\mathbf{R}-\mathbf{R}') = L_{\alpha',\alpha}^{\sigma',\sigma}(\mathbf{R}'-\mathbf{R}). \tag{W5B.4}$$

The dynamical equations become

$$M_\sigma \ddot{u}_\alpha^\sigma(\mathbf{R}, t) = -\sum_{\sigma'} \sum_{\alpha'} \sum_{\mathbf{R}'} L_{\alpha,\alpha'}^{\sigma,\sigma'}(\mathbf{R} - \mathbf{R}') u_{\alpha'}^{\sigma'}(\mathbf{R}', t). \tag{W5B.5}$$

This represents a set of $3Ns$ coupled second-order differential equations for the amplitudes.

If the atomic displacements were all made equal [i.e., $u_\alpha^\sigma(\mathbf{R}) = d_\alpha$ (for all σ and $\mathbf{R}$)], there would be no restoring force and both sides of the equation would be zero. Thus

$$0 = -\sum_{\sigma'} \sum_{\alpha'} \sum_{\mathbf{R}'} L_{\alpha,\alpha'}^{\sigma,\sigma'}(\mathbf{R} - \mathbf{R}') d_{\alpha'}. \tag{W5B.6}$$

This is true for any vector $\mathbf{d}$. Also note that as $\mathbf{R}'$ sweeps over the Bravais lattice, so does the vector $\mathbf{R} - \mathbf{R}'$. Thus one obtains the sum rule:

$$\sum_{\sigma', \mathbf{R}'} L_{\alpha,\alpha'}^{\sigma,\sigma'}(\mathbf{R}') = 0. \tag{W5B.7}$$

Using the symmetry of the L matrix [Eq. (W5B.4)] this may also be written as

$$\sum_{\sigma, \mathbf{R}'} L_{\alpha',\alpha}^{\sigma',\sigma}(\mathbf{R}') = 0. \tag{W5B.8}$$

For a mode with frequency ω and wave vector $\mathbf{k}$ the dynamical equations become

$$M_\sigma \omega^2 u_\alpha^\sigma = \sum_{\sigma'} \sum_{\alpha'} D_{\alpha,\alpha'}^{\sigma,\sigma'}(\mathbf{k}) u_{\alpha'}^{\sigma'}, \tag{W5B.9}$$

where the *dynamical matrix* is defined as

$$D_{\alpha,\alpha'}^{\sigma,\sigma'}(\mathbf{k}) = \sum_{\mathbf{R}'} L_{\alpha,\alpha'}^{\sigma,\sigma'}(-\mathbf{R}') \exp(i\mathbf{k} \cdot \mathbf{R}'). \tag{W5B.10}$$

Equation (W5B.9) is a set of only $3s$ coupled algebraic equations, so considerable simplification has been achieved. A solution to these equations determines the phonon frequencies as the eigenvalues and the polarizations of the phonons as the eigenvectors. This procedure usually involves the numerical diagonalization of a matrix with $3s$ rows and $3s$ columns.

Appendix W5C: Van Hove Singularities

In this appendix an analysis is made of the density of states in the neighborhood of a van Hove singularity at position $\mathbf{k}_0$. The first-order term in the expansion of the frequency vanishes so, to second order

$$\omega_\mu(\mathbf{k}) = \omega_\mu(\mathbf{k}_0) + \frac{1}{2} \sum_{\alpha,\beta} (k - k_0)_\alpha (k - k_0)_\beta \frac{\partial^2 \omega_\mu}{\partial k_\alpha \partial k_\beta} + \cdots . \tag{W5C.1}$$

Introduce a new coordinate system which is both translated, so that the new origin is $\mathbf{k}_0$, and rotated, so that the matrix

$$h_{\alpha\beta} = \frac{1}{2}\frac{\partial^2 \omega_\mu(\mathbf{k})}{\partial k_\alpha \partial k_\beta} \tag{W5C.2}$$

is diagonalized. In this new $\{\mathbf{k}'\}$ coordinate system

$$\omega_\mu(\mathbf{k}) = \omega_\mu(\mathbf{k}_0) + \sum_\alpha h_\alpha k_\alpha'^2, \tag{W5C.3}$$

where h_α are the eigenvalues of $h_{\alpha\beta}$. Assuming that none of the h_α vanishes, one may further rescale the coordinates by defining

$$k_\alpha'' = |h_\alpha|^{1/2} k_\alpha'. \tag{W5C.4}$$

Note that translating or rotating a vector does not alter the size or shape of a volume element in $\mathbf{k}$ space, but the scale transformation does, so $d\mathbf{k}'' = |h_1 h_2 h_3|^{1/2} d\mathbf{k}$. Let

$$\omega_\mu(\mathbf{k}) = \omega_\mu(\mathbf{k}_0) + \Delta\omega, \tag{W5C.5}$$

so

$$\rho(\omega) = \sum_\mu{}' \frac{V}{(2\pi)^3 |h_1 h_2 h_3|^{1/2}} \int d\mathbf{k}'' \delta \left[\sum_\alpha k_\alpha''^2 \mathrm{sgn}(h_\alpha) - \Delta\omega \right]. \tag{W5C.6}$$

The $\{\mathrm{sgn}(h_\alpha)\}$ numbers are ± 1, depending on the nature of the extremum. For an absolute minimum the signature is $\{+1, +1, +1\}$. For an absolute maximum it is $\{-1, -1, -1\}$. Saddle points are characterized by having mixed signs [e.g., $\{+1, +1, -1\}$, $\{+1, -1, +1\}$, etc.]. Thresholds occur at the van Hove singularities. On one side of the threshold there is an added (or subtracted) density which varies as $|\Delta\omega|^{1/2}$. Depending on the type of extremum, it could rise, fall, lie to the left, or lie to the right of the critical point.

CHAPTER W6

Thermally Activated Processes, Phase Diagrams, and Phase Transitions

W6.1 Concentration Profiles Resulting from Diffusion

The following physical situations are often important in experimental measurements of the diffusion coefficient D and also in processes in which impurities are intentionally introduced into materials (e.g., the diffusion of dopants such as P and B into Si). The first case involves the presence of a thin layer of material on a solid surface, the second involves bringing two "thick" samples of different materials into intimate contact with each other, and the third corresponds to modifying the composition profile near the surface of a solid by maintaining a source of atoms with constant activity at the surface. In all three cases the one-dimensional form of Fick's second law, Eq. (6.8) in the textbook,[†] is solved to obtain a prediction for the concentration profiles that result after diffusion has been allowed to occur.

1. Consider a thin layer of A atoms of thickness d and with N_A atoms per unit area, deposited on the surface of a second material B. When the diffusion coefficient D_A of A atoms in B is assumed to be independent of concentration, and hence of x, the concentration profile of A atoms in B for long diffusion times, such that the diffusion length $\sqrt{D_A t} \gg d$, will be given by

$$C_A(x \geq 0, t) = \frac{N_A}{\sqrt{\pi D_A t}} \exp\left(-\frac{x^2}{4D_A t}\right). \tag{W6.1}$$

   The resulting *Gaussian* profiles for the normalized concentration $C_A(x, t)/N_A$ are shown in Fig. W6.1 for several values of the diffusion length $2\sqrt{D_A t}$ on both linear and logarithmic scales. Note that the normalized surface concentration $C_A(x = 0, t)/N_A = 1/\sqrt{\pi D_A t}$ decreases with increasing time, due to the finite source of A atoms available at the surface.
2. Consider two thick solids composed of A and B atoms that are in intimate contact with each other. The source of A atoms diffusing into B is now essentially unlimited, so that the concentration of A atoms at the interface, $C_A(0, t)$, can be assumed to be constant, C_{Ao}. Other boundary conditions are $C_A(\infty, t) = 0$ and

[†] The material on this home page is supplemental to *The Physics and Chemistry of Materials* by Joel I. Gersten and Frederick W. Smith. Cross-references to material herein are prefixed by a "W"; cross-references to material in the textbook appear without the "W."

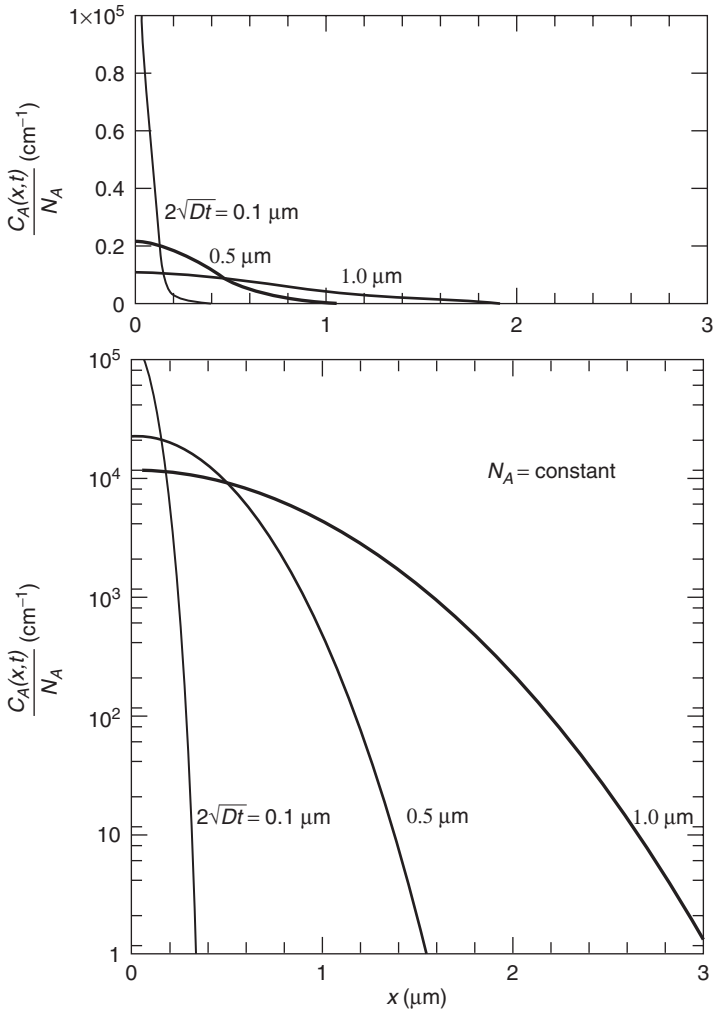

Figure W6.1. Normalized Gaussian concentration profiles originating from a thin layer of atoms on the surface of a solid at $x = 0$ for several values of $2\sqrt{D_A t}$ on both linear and logarithmic scales. (From A. S. Grove, *Physics and Technology of Semiconductor Devices*, copyright 1967 by John Wiley & Sons, Inc. Reprinted by permission of John Wiley & Sons, Inc.)

$C_A(x, 0) = 0$. After interdiffusion is allowed to occur, the concentration profile of A atoms in B is given by

$$C_A(x, t) = C_{Ao}\left[1 - \text{erf}\left(\frac{x}{2\sqrt{D_A t}}\right)\right] = C_{Ao}\,\text{erfc}\left(\frac{x}{2\sqrt{D_A t}}\right). \qquad \text{(W6.2)}$$

Here the chemical diffusion coefficient D_A is again assumed to be independent of x. The function erf(x), called the *error function*, is one of the most important functions in diffusion theory and erfc(x) = 1 − erf(x) is the *complementary*

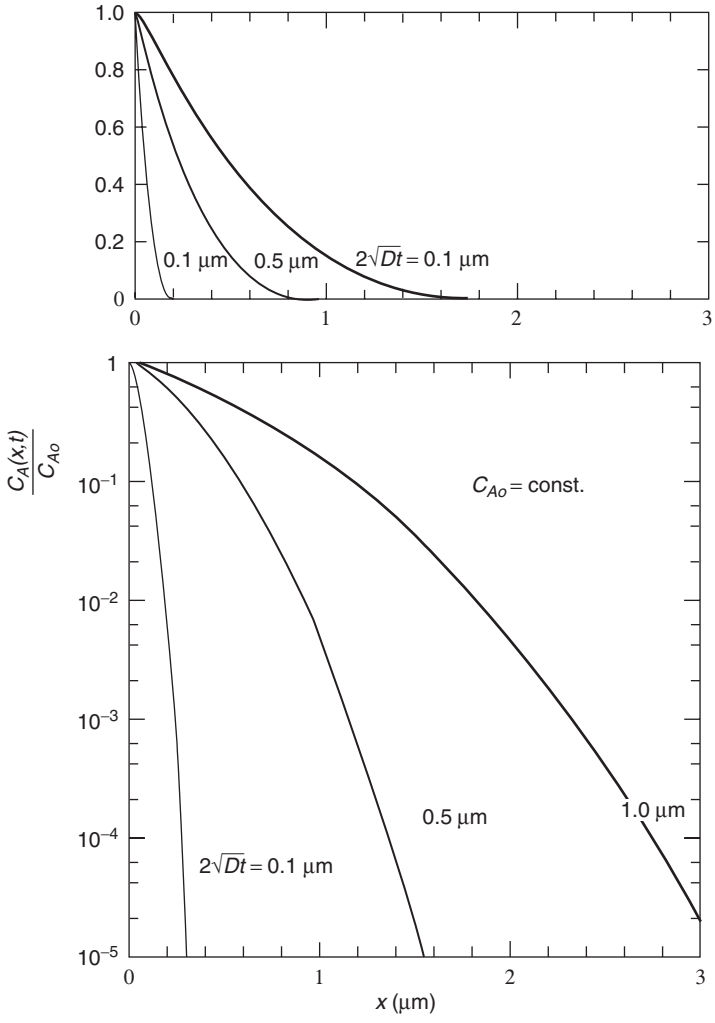

Figure W6.2. Normalized concentration profiles originating from an essentially unlimited source of atoms for several values of the diffusion length $\sqrt{D_A t}$ on both linear and logarithmic scales. (From A. S. Grove, *Physics and Technology of Semiconductor Devices*, copyright 1967 by John Wiley & Sons, Inc. Reprinted by permission of John Wiley & Sons, Inc.)

error function.[†] The resulting normalized concentration profiles $C_A(x, t)/C_{Ao}$ are shown in Fig. W6.2 for several values of $\sqrt{D_A t}$ on both linear and logarithmic scales.

3. Another important situation corresponds to modifying the concentration profile near the surface of a solid by maintaining a constant concentration C_A of A atoms at the surface of an initially homogeneous solid of composition C_{Ao}. This can be accomplished, for example, by exposing the solid to a source of A atoms

[†] $\text{erf}(x) = (2/\sqrt{\pi}) \int_0^x e^{-a^2}\, da$, with $\text{erf}(0) = 0$ and $\text{erf}(\infty) = 1$.

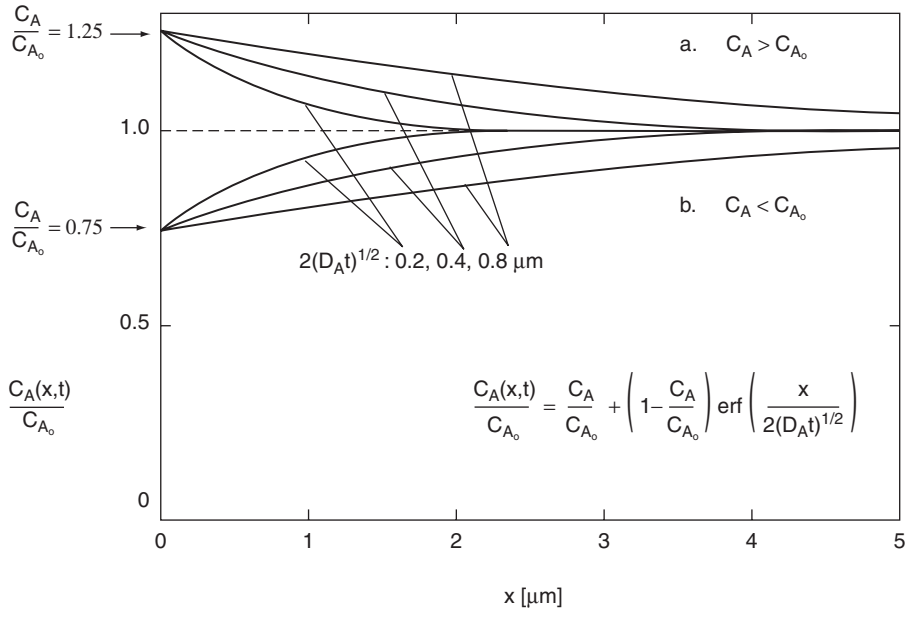

Figure W6.3. Normalized concentration profiles in a solid obtained when its surface is exposed to a source of atoms in the vapor phase with constant activity for several values of the diffusion length $2\sqrt{D_A t}$ using only a linear scale. Here C_A is the constant concentration at the surface and C_{Ao} is the initial concentration in the solid. Data used to generate these plots: for B diffusing into Si at $T \approx 1025°C$, $D_A = 10^{-2}$ μm^2/h, and $t = 1$, 4, 16 h.

in the vapor phase with constant activity. The net diffusion of A atoms either into the solid ($C_A > C_{Ao}$) or out of the solid ($C_A < C_{Ao}$) is then allowed to take place. If the solid has a thickness $d \gg \sqrt{D_A t}$, the resulting concentration profile of A atoms is given by

$$\frac{C_A(x,t) - C_A}{C_{Ao} - C_A} = \text{erf}\left(\frac{x}{2\sqrt{D_A t}}\right). \tag{W6.3}$$

These normalized concentration profiles are shown in Fig. W6.3 for several values of $2\sqrt{D_A t}$ using only a linear scale but for $C_A > C_{Ao}$ and $C_A < C_{Ao}$. When $C_{Ao} = 0$ this result is identical to that given in Eq. (W6.2). Note that $C_A = 0$ for desorption of A atoms into a vacuum.

W6.2 Examples of Diffusion Studies

Self-Diffusion in Cu. Experimental results for the self-diffusion coefficient $D(T)$ of Cu are presented in Fig. W6.4 together with data on the fractional vacancy concentration $n_v(T)$, also shown in Fig. 4.23. As discussed in Section 4.7, Schottky defects (i.e., simple vacancies) are identified as the dominant intrinsic defect in FCC metals such as Cu and are responsible for the self-diffusion process. As a result, the following

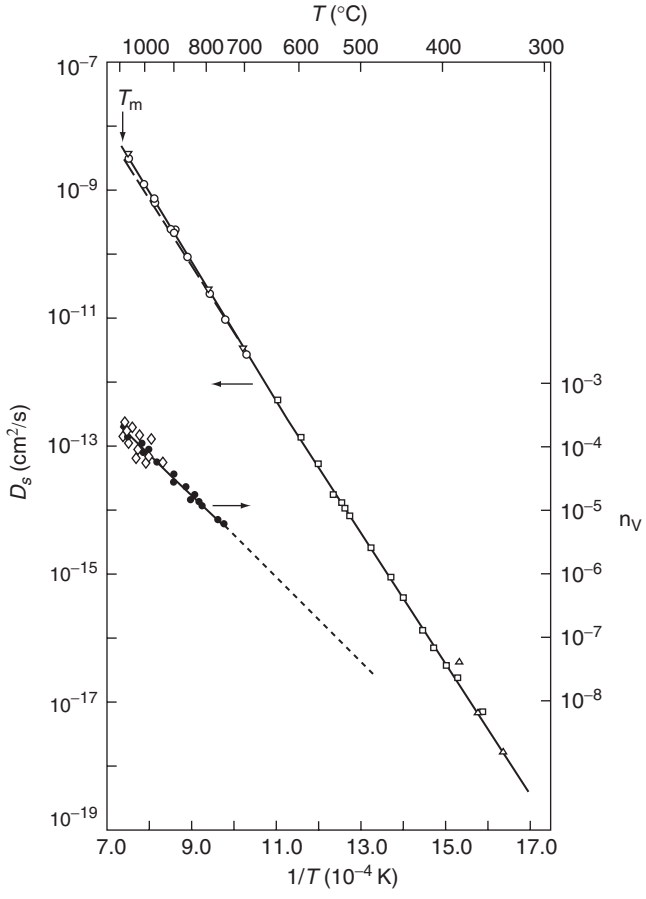

Figure W6.4. Experimental results for the self-diffusion coefficient $D(T)$ of Cu along with data on the vacancy concentration $n_v(T)$. [from A. S. Berger et al., *J. Phys. F: Met Phys.*, **9**, 1023 (1979). Reprinted by permission of the Institute of Physics.]

expressions from the textbook, Eqs. (6.14), (6.18), and (6.19),

$$D(T) = D_o \exp\left(-\frac{E_a}{k_B T}\right),$$

$$D_o = f a^2 \frac{\omega_D}{2\pi} \exp\left(\frac{\Delta S_f + S_m}{k_B}\right),$$

$$E_a = \Delta H_f + H_m,$$

can be used to analyze these data, except just below T_m, where there appears to be some upward curvature in $D(T)$, possibly due to a contribution from divacancies. Self-diffusion data such as these are often obtained using the *tracer method*, in which the motion of radioactive isotopes of the host crystal atoms are "traced" using radiochemical analysis.

The activation energy for self-diffusion in Cu is found from the data presented in Fig. W6.4 to be $E_a = 2.07$ eV. From this result and the value of $\Delta H_f = 1.28$ eV for vacancy formation in Cu presented in Section 4.7, it follows that the enthalpy of migration of vacancies in Cu is given by

$$H_m = E_a - \Delta H_f = 2.07 - 1.28 = 0.79 \text{ eV}. \tag{W6.4}$$

This value of H_m is typical for the noble metals. The prefactor D_o for self-diffusion in Cu obtained from Fig. W6.4 is 10^{-5} m^2/s. It is difficult to obtain a more precise value for D_o due to the lengthy extrapolation involved.

An interesting correlation exists between measured values of E_a for self-diffusion in metals and their melting temperatures T_m. The observed empirical relationship is given, to within about $\pm 10\%$, by

$$E_a(\text{eV}) \approx \frac{T_m(\text{K})}{700}. \tag{W6.5}$$

This correlation results from the fact that both T_m and E_a are determined by the strength of the bonding of atoms in the solid. Typical values of D_o for self-diffusion in metals are in the range 10^{-5} to 10^{-4} m^2/s, and typical diffusion coefficients $D(T_m)$ at the melting temperature are on the order of 10^{-12} m^2/s.

An important diffusion-related phenomenon occurring in Si-based electronic devices is the *electromigration* of Al and Cu ions in the metal lines connecting various elements and levels within the planar structure. The diffusion of the metal ions in this case is driven by the electrical current in the interconnect lines, the mechanism being the transfer of momentum from the electrons to the ions. In this respect Cu has an advantage over Al due to its higher atomic mass. The higher resistances and voids created in the metal lines due to electromigration can lead to the failure of the device. Electromigration is described in more detail in Chapter 12.

Self-Diffusion and Impurity Diffusion in Si. Experimental results for self-diffusion and for the diffusion of several substitutional and interstitial impurities in Si are summarized in Fig. W6.5. Concentration profiles and diffusion coefficients for dopant impurities in semiconductors are typically measured using electrical techniques (e.g., the measurement of capacitance–voltage characteristics of p-n junctions). Self-diffusion in Si remains an area of active research, with the question of whether the diffusion is via vacancies or interstitials still under discussion. Recent calculations[†] have indicated that only the self-interstitial diffusion mechanism can explain the magnitude of the observed self-diffusion of Si that occurs with an activation energy E_a in the range 4.5 to 5 eV and a prefactor $D_o \approx 0.01$ to 0.1 m^2/s. This value of D_o is much higher than the values typically observed for diffusion in metals. The dominance of the self-interstitial, corresponding to a "dumbbell" configuration of two Si atoms occupying a single lattice site, has been attributed to its predicted lower enthalpy of formation, $\Delta H_f = 3.3$ eV, compared with a predicted value of $\Delta H_f = 4.1$ eV for the vacancy.

[†] P. E. Bloechl et al., *Phys. Rev. Lett.*, **70**, 2435 (1993).

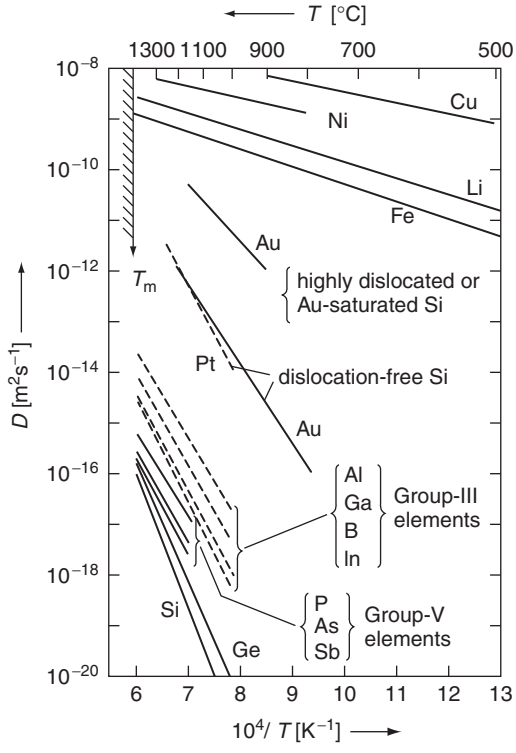

Figure W6.5. Experimental results for self-diffusion and for the diffusion of several substitutional and interstitial impurities in Si. (From W. Frank, *Defect and Diffusion Forum* 75, 121 (1991). Reprinted by permission of Scitec Publications.)

The diffusion of substitutional dopant impurities in Si is mediated by self-interstitials and vacancies and is an essential part of the processing of Si-based devices. It can be seen from Fig. W6.5 that the group III and V elements all diffuse faster in Si than does Si itself, with values of E_a in the range 3.4 to 3.6 eV for acceptors and 3.9 to 4.2 eV for donors. Donors and acceptors diffuse much slower, however, than the metal impurities shown, which have values of E_a in the range 0.4 to 0.8 eV and which diffuse via the direct interstitial mechanism. These observations are consistent with the group III and V elements entering the Si lattice substitutionally, thus participating in the covalent bonding, while the metal atoms enter interstitial sites. The rapid diffusion of unwanted metallic impurities in Si also plays an important role in their removal or trapping near dislocations or other extended defects in the process known as *gettering*.

A recent study has found that in Si near $T = 800°C$, the acceptor ion B^- diffuses via an interstitial mechanism, while the donor ion Sb^+ diffuses via a vacancy mechanism.[†] This is consistent with a net negative charge for vacancies in Si, which therefore attract donor ions such as Sb^+ and repel acceptor ions such as B^-. In addition, the larger atomic size of group V donors makes them less likely to diffuse through the interstitial sites in Si compared to smaller group III acceptors such as B^-.

[†] H.-J. Grossman et al., *Appl. Phys. Lett.*, **71**, 3862 (1997).

W6.3 Examples of Vaporization Studies

Typical experimental methods employed for the determination of the vaporization flux $J_{\text{vap}}(T)$ or, equivalently, of the equilibrium vapor pressure $P_{\text{eq}}(T)$ involve direct measurement of the weight loss of the crystal and the detection of the evaporated species via mass spectrometry.

The equilibrium vapor pressures $P_{\text{eq}}(T)$ for Fe and Si presented in Fig. W6.6 are the recommended values from a critical review[†] of the data for the thermodynamic properties of Fe and Si. It can be seen that vaporization is indeed thermally activated for Fe and Si. From these data the enthalpies and entropies of vaporization, defined in terms of $\Delta_r G^{\text{o}}$ by

$$\Delta_r G^{\text{o}} = \Delta H_{\text{vap}} - T\Delta S_{\text{vap}}, \tag{W6.6}$$

can be determined. The enthalpy of vaporization $\Delta H_{\text{vap}} = H(\text{vapor}) - H(\text{solid})$ is simply equal to the standard enthalpy of formation $\Delta_f H^\circ$ of the vapor [i.e., Fe(g) or Si(g)] since the solid is in its standard state, where $\Delta_f H^\circ$ is defined to be zero. Values of ΔH_{vap} and ΔS_{vap} at $T = 298.15$ K for Fe and Si are presented in Table W6.1 along with the melting temperature T_m and the equilibrium vapor pressure at T_m. Note that, as expected, $\Delta H_{\text{vap}} = 4.66$ eV/atom for Si is quite close to 2E(Si–Si), where $E(\text{Si–Si}) = 2.34$ eV is the Si–Si covalent bond energy (see the discussion of bond

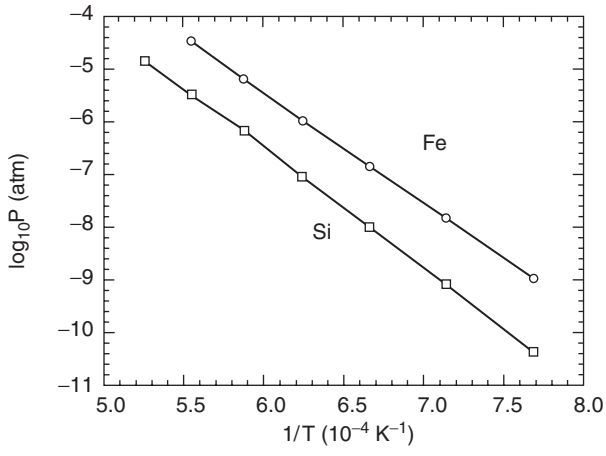

Figure W6.6. Equilibrium vapor pressures $P_{\text{eq}}(T)$ of Fe and Si. [Data from P. D. Desai, *J. Phys. Chem. Ref. Data*, **15**, 967 (1986).]

TABLE W6.1 Vaporization Results for Fe and Si

	$\Delta H_{\text{vap}}(298.15\ \text{K})$ (kJ/mol; eV/atom)	$\Delta S_{\text{vap}}(298.15\ \text{K})$ (J/mol·K)	T_m (K)	$P_{\text{eq}}(T_m)$ (atm)
Fe	415.5 ± 1.3; 4.31 ± 0.01	180.49	1811	3.58×10^{-5}
Si	450 ± 4; 4.66 ± 0.04	167.98	1687	5.41×10^{-7}

Source: Data from P. D. Desai, *J. Phys. Chem. Ref. Data*, **15**, 967 (1986).

[†] P. D. Desai, *J. Phys. Chem. Ref. Data*, **15**, 967 (1986).

energies in Chapter 2). Mass spectrometry has shown that the Si_2 dimer and Si_3 trimer represent about 0.4% and 0.1%, respectively, of the equilibrium vapor of Si at T_m.

When determining the vapor pressure of Si, care must be taken to ensure that the vaporization of Si atoms occurs from a clean surface. The presence of carbon atoms on the Si surface can retard vaporization due to the formation of the high-melting-point compound SiC. The presence of oxygen atoms, on the other hand, can lead to greatly enhanced vaporization rates due to the formation of the volatile molecule SiO.

W6.4 Gibbs Phase Rule

In a binary eutectic alloy such as Pb–Sn there are three separate phases whose compositions can be varied. In addition, the temperature and pressure of the alloy can be varied. There would thus appear to be five quantities or *degrees of freedom* that can be controlled independently (i.e., x_l, x_α, x_β, T, and P). In practice, however, these degrees of freedom are not all independent, as illustrated by the *Gibbs phase rule*.

Consider a system of C components, labeled $c = 1, 2, \ldots, C$, with P possible phases, labeled $p = 1, 2, \ldots, P$. Let μ_{cp} be the chemical potential for component c in phase p. At thermal equilibrium the system has a common pressure and temperature, and the chemical potential for each component is the same in every phase. Thus

$$\begin{aligned} \mu_{11} &= \mu_{12} = \cdots \mu_{1P} \\ \mu_{21} &= \mu_{22} = \cdots \mu_{2P} \\ &\vdots \\ \mu_{C1} &= \mu_{C2} = \cdots \mu_{CP}, \end{aligned} \tag{W6.7}$$

for a total of $C(P-1)$ independent equations.

Let x_{cp} denote the mole fraction of component c in phase p. There are C times P compositional variables, x_{cp}, and for each phase there is the constraint that

$$\sum_{c=1}^{P} x_{cp} = 1, \qquad p = 1, 2, \ldots, P. \tag{W6.8}$$

There are thus a total of $(C-1)P$ independent mole fractions. Including the pressure and temperature, the number of independent variables is $(C-1)P + 2$. The number of degrees of freedom F (sometimes called the *variance*) is the difference between the number of independent variables and the number of equations relating them to each other, that is,

$$F = (C-1)P + 2 - C(P-1) = C - P + 2, \tag{W6.9}$$

which proves the Gibbs phase rule.

PROBLEMS

W6.1 Show that the total number of atoms diffusing either into or out of the surface of a solid of area A in time t is given by $\Delta N_A(t) = 2(C_A - C_{Ao})A\sqrt{Dt/\pi}$ when

the concentration profile $C_A(x, t)$ in the solid is given by Eq. (W6.3). Note that $\int_0^\infty \text{erfc}(x)\,dx = 1/\sqrt{\pi}$.

W6.2 Using the fact that the average distance of diffusion of an atom in a solid in time t is given approximately by $L = \sqrt{\langle X^2 \rangle} \approx \sqrt{Dt}$, calculate the average time $\langle t \rangle$ it takes for a Cu atom (see Fig. W6.4) to "diffuse" one NN distance at $T = 1000$ K. On average, what is the order of magnitude of the number of oscillations that a Cu atom undergoes during this time?

CHAPTER W7

Electrons in Solids: Electrical and Thermal Properties

W7.1 Boltzmann Equation

In Section 7.2 of the textbook,[†] formulas were derived on the basis of Newtonian mechanics and the assumption that all of the conduction electrons contribute to the electrical current. In the Sommerfeld theory this is not correct. Electrons with energies less than $\approx E_F - k_B T$ have difficulty being accelerated by the electric field since the states above them are already filled. Only those electrons in the immediate vicinity of the Fermi surface are excitable. The question is how to rederive the conductivity formula taking into account the Pauli exclusion principle. Here a semiclassical approach is adopted.

One introduces a distribution function $f(\mathbf{r}, \mathbf{p}, t)$ to describe the system of electrons in phase space. The quantity $2f(\mathbf{r}, \mathbf{p}, t)\, d\mathbf{r}\, d\mathbf{p}/h^3$ gives the number of electrons within volume element $d\mathbf{r}$ and within a momentum bin of size $d\mathbf{p}$ at time t (the factor of 2 is for spins). The distribution function evolves in time due to collisions. The Boltzmann equation relates the total time derivative of f to the difference between f and the equilibrium distribution function $f_0 = F(E, T)$, where E is the energy,

$$\frac{df}{dt} = \frac{\partial f}{\partial t} + \frac{d\mathbf{r}}{dt} \cdot \frac{\partial f}{\partial \mathbf{r}} + \frac{d\mathbf{p}}{dt} \cdot \frac{\partial f}{\partial \mathbf{p}} = \frac{\partial f}{\partial t} + \mathbf{v} \cdot \nabla f + \mathbf{F} \cdot \frac{\partial f}{\partial \mathbf{p}} = -\frac{f - f_0}{\tau(\mathbf{p})}, \quad \text{(W7.1)}$$

where $\mathbf{v}$ is the velocity and $\mathbf{F} = -e\mathbf{E}_0$ is the force on the electron. This equation has been written in what is called the *relaxation-time approximation*: it is assumed that the relaxation of f to f_0 occurs in a time $\tau(\mathbf{p})$ as a result of collisions. Interest here is in the steady-state behavior, so $\partial f/\partial t = 0$ and $f = f(\mathbf{r}, \mathbf{p})$. Attention will also be restricted to the case of an infinite medium where a spatially homogeneous solution is sought, so $f = f(\mathbf{p})$. It will also be assumed that τ depends only on E.

An approximate expression for f is developed by substituting f_0 for f in the left-hand side of Eq. (W7.1):

$$f = f_0 - \tau \left(\mathbf{v} \cdot \nabla f_0 - e\mathbf{E}_0 \cdot \frac{\partial f_0}{\partial \mathbf{p}} \right) + \cdots . \quad \text{(W7.2)}$$

[†] The material on this home page is supplemental to *The Physics and Chemistry of Materials* by Joel I. Gersten and Frederick W. Smith. Cross-references to material herein are prefixed by a "W"; cross-references to material in the textbook appear without the "W."

Since $f_0 = F(E, T)$, the derivatives may be reexpressed in terms of energy derivatives:

$$f = f_0 - \tau \frac{\partial f_0}{\partial E} \mathbf{v} \cdot \left[\frac{1}{\beta} \nabla(\beta(E - \mu)) - e\mathbf{E}_0 \right]. \tag{W7.3}$$

The electrical-current density is

$$\mathbf{J}(\mathbf{r}, t) = -2e \int \mathbf{v} f(\mathbf{r}, \mathbf{p}, t) \frac{d\mathbf{p}}{h^3}, \tag{W7.4}$$

and the heat-current density is

$$\mathbf{J}_Q(r, t) = 2 \int (E - \mu) \mathbf{v} f(\mathbf{r}, \mathbf{p}, t) \frac{d\mathbf{p}}{h^3}. \tag{W7.5}$$

Note that the thermal energy transported is positive when E exceeds μ and negative when E is less than μ. Upon inserting Eq. (W7.3) into Eqs. (W7.4) and (W7.5), the need to angular-average a product of two velocities over momentum space is encountered. One uses $\langle \mathbf{v}\mathbf{v} \cdot \mathbf{A} \rangle = v^2 \mathbf{A}/3 = 2 < E\mathbf{A} > /3m$, where $\mathbf{A}$ is a constant vector, and obtains

$$\mathbf{J} = -\frac{16\pi e\sqrt{2m}}{3h^3} \int E^{3/2} \tau(E) \frac{\partial f_0}{\partial E} \left(\frac{E - \mu}{T} \nabla T + \nabla \mu + e\mathbf{E}_0 \right) dE, \tag{W7.6}$$

$$\mathbf{J}_Q = \frac{16\pi\sqrt{2m}}{3h^3} \int E^{3/2} (E - \mu) \tau(E) \frac{\partial f_0}{\partial E} \left(\frac{E - \mu}{T} \nabla T + \nabla \mu + e\mathbf{E}_0 \right) dE. \tag{W7.7}$$

An expression for μ is given in Eq. (7.24). Evaluation of the integrals leads to the formulas

$$\mathbf{J} = \sigma \mathbf{E}_0 - \sigma S \nabla T, \tag{W7.8}$$

$$\mathbf{J}_Q = \sigma S T \mathbf{E}_0 - \kappa \nabla T, \tag{W7.9}$$

which are called the *Onsager relations*.

W7.2 Random Tight-Binding Approximation

In this section we study the behavior of $\rho(E)$ for a random one-dimensional solid. Two models for randomness are studied: the first with "bond" randomness and the second with "site" randomness. In the bond case the tunneling integral, t, varies randomly from bond to bond, but the site energy, ϵ, remains constant. As an example, let t assume two values, t_1 and t_2, with probabilities p_1 and p_2, respectively. Numerical results are displayed in Fig. W7.1, where results are shown for $\rho(E)$ for the case where $N = 125$ sites, $t_1 = 1$, $t_2 = 2$, and $p_1 = p_2 = \frac{1}{2}$. A suitable average over many independent configurations has been made. A comparison is made with the uniform case involving an average tunneling integral $\langle t \rangle = p_1 t_1 + p_2 t_2$. It is apparent that near the band center the densities of states are the same, while near the band edges the

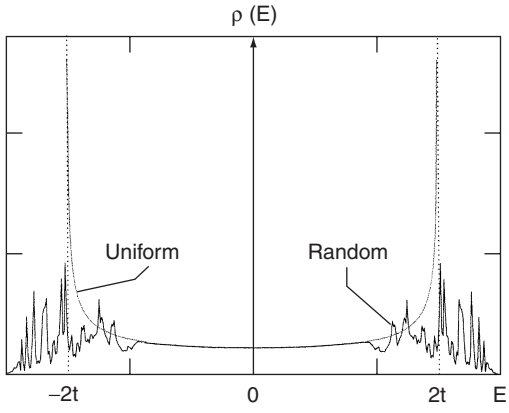

Figure W7.1. Comparison of electron densities of states for the random-bond and uniform one-dimensional solids.

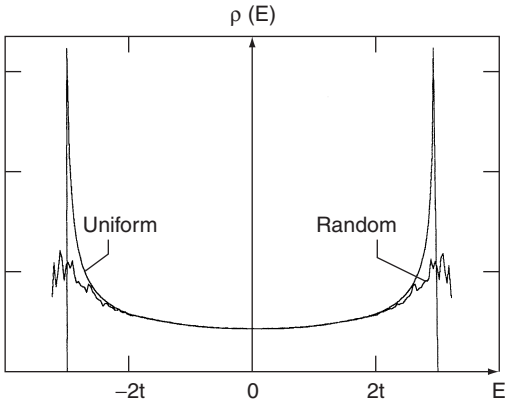

Figure W7.2. Comparison of electron densities of states for the random-site and uniform one-dimensional solids.

random solid exhibits an irregular behavior in contrast to the smooth but divergent behavior of the uniform solid.

In Fig. W7.2 the result for the random-site model is presented. In this model the site energy is allowed to have one of two values, ϵ_1 or ϵ_2, with probabilities p_1 and p_2, respectively. The tunneling integral is held fixed at $t = 1.5$. As before, there is some rough but reproducible behavior near the band edges. Note that in both the random-site and random-bond cases there is a tailing off of the density of states beyond the band edges.

W7.3 Kronig–Penney Model

An analytic solution to Bloch's difference equation can be found when all Fourier coefficients are equal (i.e., $V_{\mathbf{G}} = U$) and the problem is one-dimensional. Then Eq. (7.54)

becomes

$$\left[\frac{\hbar^2}{2m}(\mathbf{k}+\mathbf{G})^2 - E\right] u_{\mathbf{G}}(\mathbf{k}) + U\sum_{\mathbf{G}'} u_{\mathbf{G}-\mathbf{G}'}(\mathbf{k}) = 0. \tag{W7.10}$$

Let $S = \sum u_{\mathbf{G}}$. If $S = 0$, then $u_{\mathbf{G}} = 0$ and there is no nonzero solution. If $S \neq 0$, dividing by the first factor and summing over all $\mathbf{G}$ yields

$$S + U\sum_{\mathbf{G}} \frac{1}{(\hbar^2/2m)(\mathbf{k}+\mathbf{G})^2 - E} S = 0. \tag{W7.11}$$

This will have a non-trivial solution when

$$1 + U\sum_{\mathbf{G}} \frac{1}{(\hbar^2/2m)(\mathbf{k}+\mathbf{G})^2 - E} = 0. \tag{W7.12}$$

In one dimension $G_n = 2\pi n/a$, where n is an integer, and the sum converges. The dispersion relations are given by the roots $E(k)$ of the equation

$$1 + \sum_{n=-\infty}^{\infty} \frac{U}{(\hbar^2/2m)(k + 2\pi n/a)^2 - E} = 0. \tag{W7.13}$$

Note some simple properties of the left-hand side of this equation: (1) it is periodic under the replacement $k \to k \pm 2\pi/a$; (2) it is an analytic function of k except for simple poles at $k = -2\pi n/a \pm \sqrt{2mE/\hbar^2}$; and (3) as $k \to \pm i\infty$ in the complex plane, the left-hand side approaches 1. From the theory of complex variables (Carlson's theorem) it follows that these properties are uniquely shared by the function on the left-hand side of the following equation:

$$1 + \frac{Ua}{2\hbar}\sqrt{\frac{m}{2E}}\left\{\cot\left[\frac{a}{2}\left(k - \sqrt{\frac{2mE}{\hbar^2}}\right)\right] - \cot\left[\frac{a}{2}\left(k + \sqrt{\frac{2mE}{\hbar^2}}\right)\right]\right\} = 0. \tag{W7.14}$$

Letting $y = a\sqrt{2mE/\hbar^2}$, one has, after some trigonometric manipulation,

$$\cos ka = \cos y + \frac{ma^2U}{4\hbar^2}\frac{\sin y}{y}. \tag{W7.15}$$

It is important to note that the left-hand side of this equation is bounded by ± 1. For arbitrary y, the right-hand side can exceed these bounds. No real solution is possible for such values. Thus there are certain y values, and consequently certain energies, for which no solution exists. These are called *forbidden bands* or *gaps*. Correspondingly, the regions of energy for which solutions exist are called *allowed bands*.

An example of the energy spectrum for the Kronig–Penney model is given in Fig. W7.3. As before, the energy gaps open at the boundaries of the first Brillouin zone. The Kronig–Penney model considered here corresponds to the case where the

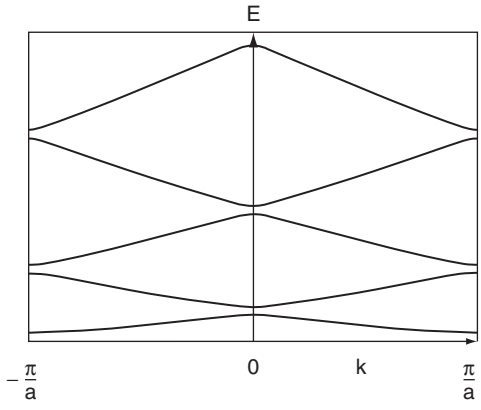

Figure W7.3. Energy spectrum for the one-dimensional Kronig-Penney model. Here $ma^2U/(4\hbar^2) = -10$.

potential consists of a periodic array of delta-function potentials for which

$$V(x) = U \sum_{n=-[N/2]}^{[N/2]} e^{i(2\pi n/a)x} = UN \sum_{n=-[N/2]}^{[N/2]} \delta_{x,na}, \tag{W7.16}$$

where N has been assumed to be odd and $[N/2]$ stands for the integer part of $N/2$. It is also possible to formulate the Kronig–Penney model for the case of a periodic square-well potential.

W7.4 Hall Effect in Band Theory

A discussion of the Hall effect from the perspective of band theory predicts a more complicated behavior than that of classical Drude theory. The Boltzmann equation for the distribution function, f_n, in a given band n is

$$\mathbf{v}_n \cdot \nabla f_n + \mathbf{F}_n \cdot \frac{\partial f_n}{\partial \mathbf{p}} = -\frac{f_n - f_{n_0}}{\tau_n(\mathbf{p})}, \tag{W7.17}$$

with $\mathbf{F}_n = -e(\mathbf{E} + \mathbf{v}_n \times \mathbf{B})$ and $\mathbf{v}_n = \partial\varepsilon_n/\partial\mathbf{p}$ [see Eq. (W7.1)]. Henceforth the band index n will be suppressed. Equation (W7.17) is rewritten as

$$f = f_0 - \tau\mathbf{v} \cdot \nabla f + e\tau\mathbf{E} \cdot \frac{\partial f}{\partial \mathbf{p}} + e\tau\mathbf{v} \times \mathbf{B} \cdot \frac{\partial f}{\partial \mathbf{p}} \tag{W7.18}$$

and is iterated to produce an expansion in increasing powers of the fields:

$$f = f_0 + e\tau\mathbf{E} \cdot \mathbf{v}\frac{\partial f_0}{\partial \varepsilon} + e^2\tau\mathbf{v} \times \mathbf{B} \cdot \frac{\partial}{\partial \mathbf{p}}\left(\tau\mathbf{E} \cdot \mathbf{v}\frac{\partial f_0}{\partial \varepsilon}\right) + \cdots . \tag{W7.19}$$

It is seen from this expression that filled bands do not contribute to the currents, since $\partial f_0/\partial\varepsilon = 0$, and no current is supported by the equilibrium distribution. The current

density from Eq. (W7.4) is

$$\mathbf{J} = -2e \int \frac{d\mathbf{p}}{h^3} f\mathbf{v}$$

$$= \sigma\mathbf{E} - \frac{2e^3}{h^3} \int d\mathbf{p} \frac{\partial f_0}{\partial \varepsilon} \tau \mathbf{v}\mathbf{v} \times \mathbf{B} \cdot \frac{\partial}{\partial \mathbf{p}} (\tau \mathbf{E} \cdot \mathbf{v}). \tag{W7.20}$$

Attention here is restricted to the case of an isotropic metal. Assume $\tau = \tau(\varepsilon)$ and write $\mathbf{p} = m(\varepsilon)\mathbf{v}$, so

$$\mathbf{J} = \sigma\mathbf{E} + \lambda\mathbf{E} \times \mathbf{B}, \tag{W7.21}$$

where

$$\lambda = \frac{2e^3}{3h^3} \int d\mathbf{p} \frac{\partial f_0}{\partial \varepsilon} \frac{(\tau v)^2}{m(\varepsilon)}. \tag{W7.22}$$

In a multiband case one would sum this expression over all partially occupied bands. For a perpendicular geometry ($\mathbf{E} \perp \mathbf{B}$), the Hall coefficient may be expressed as

$$R_H = \frac{\lambda}{\sigma^2}. \tag{W7.23}$$

The expression for λ shows that its magnitude and sign depends on the effective mass at the Fermi level. This mass may be either positive or negative, depending on the curvature of the energy band. For example, in the case of aluminum, the Fermi surface lies outside the first Brillouin zone and has contributions from the second, third, and fourth Brillouin zones. The net contributions from these bands produces a net positive value for the Hall coefficient, opposite to that predicted by the classical Drude theory. The Hall effect in semiconductors is discussed in Section 11.8.

W7.5 Localization

A measure of the ease with which a carrier can move through a crystal is the mobility $\mu = \langle v \rangle / E$, where $\langle v \rangle$ is the drift velocity and E is the electric field strength. In a metal the mobility is determined by the collision time through the formula $\mu = e\tau/m$. The connection between the mobility and the conductivity differs in two and three dimensions. In $d = 3$ the relation is $\sigma = ne\mu$, whereas in $d = 2$ it is $\sigma = Ne\mu$, where n and N are the number of electrons per unit volume and per unit area, respectively. Obviously, the units for are different in the two cases, being Ω^{-1} m^{-1} and Ω^{-1}, respectively. For a thin film of thickness t, $n = N/t$.

In this section, disordered solids, in which the electron mean free path is determined by the amount of disorder, are studied. The mean free path is related to the collision time by $\lambda = v_F \tau$, v_F being the Fermi velocity. There is a minimum value that λ can have for the solid still to have finite conductivity. Ioffe and Regel[†] (1960) argued that for conductivity, the electron waves would have to be able to propagate throughout the metal. The presence of a mean free path introduces an uncertainty in the wave vector, $\Delta k \approx 1/\lambda$, as may be inferred from Heisenberg's uncertainty principle. However, for the wave vector to have a meaning, $\Delta k < k \approx k_F$. Using $mv_F = \hbar k_F$, this gives $\mu_{\min} = e/\hbar k_F^2$ as

[†] A. F. Ioffe and A. R. Regel, Prog. Semicond., **4**, 237 (1960).

the minimum metallic mobility. The Ioffe–Regel criterion for localization is $k_F\lambda < 1$. The Fermi wave vector is given by $k_F = (2\pi N)^{1/2}$ and $k_F = (3\pi n)^{1/3}$ for $d = 2$ and 3, respectively. This implies the existence of a minimum metallic conductivity given by

$$\sigma > \sigma_{\min} \equiv \begin{cases} \dfrac{e^2}{2\pi\hbar} = \dfrac{1}{25,813\ \Omega} & \text{if} \quad d = 2, \qquad \text{(W7.24}a\text{)} \\ \dfrac{e^2 k_F}{3\pi^2\hbar} & \text{if} \quad d = 3. \qquad \text{(W7.24}b\text{)} \end{cases}$$

Note that in $d = 2$, $\sigma_{\min}$ is independent of the properties of the metal. In $d = 3$, $\sigma_{\min} = 1.12 \times 10^5\ \Omega^{-1}\text{m}^{-1}$ for Cu, compared with $\sigma = 5.88 \times 10^7\ \Omega^{-1}\text{m}^{-1}$at $T = 295$ K.

Quantum-mechanical effects modify the classical Drude expression for the conductivity. For weak disorder the rate for elastic backscattering is enhanced due to constructive interference of direct and time-reversed scattering events. Thus, suppose that there is a sequence of scattering events for the electron from ion sites labeled A, B, C, . . . , X that lead to the electron being backscattered. The time-reversed scattering sequence, X, . . . , C, B, A, also leads to backscattering of the electron. In quantum mechanics one must add together all amplitudes for a given process to determine the total amplitude. Adding the above-mentioned amplitudes before squaring leads to constructive interference and an enhanced backscattering. If the backscattering is increased, probability conservation implies that it comes at the expense of forward scattering, and hence the conductivity. This effect is called *weak localization*. One may show that the conductivity change is approximately

$$\frac{\Delta\sigma}{\sigma} \approx -\frac{3}{\pi(k_F\lambda)^2}. \qquad \text{(W7.25)}$$

Suppose that one looks at impurities in a solid with a distribution of electron site energies $\{E_i\}$ whose width is W. The sites are coupled by tunneling matrix elements, which decay exponentially with distance. In the familiar tight-binding model, all the site energies are degenerate and the bandwidth, B, is determined by the NN tunneling matrix element. All the states are extended Bloch waves and the conductivity is infinite.

In the disordered solid, things are not as simple. For conduction to occur, an electron must tunnel from one site to another, and this requires a mixing of the local site wavefunctions. From perturbation theory, two conditions must be satisfied for this to occur: There must be a sizable tunneling matrix element connecting the sites, and the energy difference between the site levels must be very small. These conditions are not likely to occur simultaneously for any given pair of states. The problem is to explore this competition as the size of the system becomes large. This is usually best done by computer experiment. The results depend on the dimensionality of the system.

As disorder is introduced, some of the states separate from the allowed band and reside in what was previously the forbidden region (e.g., the bandgap). This phenomenon was seen in the discussion of the one-dimensional tight-binding solid when randomness was present and there was an irregular component to the density of states (see Section W7.2). These states are localized in space, meaning that their wavefunctions die off rapidly with distance away from a given point in the crystal. As more disorder is introduced, some of the previously occupied band states are converted to localized states. The line of demarcation between the localized and extended states is called the *mobility edge*. With increasing disorder, W is increased, and a critical value

of W/B is ultimately reached for which all states become localized. This is called the *Anderson localization transition*. The solid then becomes an insulator.

An estimate of the critical value of W/B can be made as follows. For electrons to hop from site to site, one needs degeneracy. What determines whether two states are degenerate or not is the size of the tunneling matrix element t compared with their energy separation ΔE. If t is larger than ΔE, the states will mix and one may consider them to be effectively degenerate. Since W represents the full spread of site energies, the probability that two states will be "degenerate" is given by $p = 2t/W$. Delocalization may be interpreted as a percolation phenomenon and it is possible for the electron to propagate a large distance by following a percolation cluster. In the discussion of percolation in Section 7.16 it was found that the percolation transition occurs when $p = d/Z(d-1)$ [see Eq. (7.130)]. It was also found in the discussion of the tight-binding approximation in Section 7.9 that the bandwidth is $B = 2Zt$ [see Eq. (7.94)]. Thus the transition occurs when

$$\frac{W}{B} = \frac{d-1}{d}. \tag{W7.26}$$

For $d = 3$ this gives $B/W = 1.5$, in rough agreement with computer experiments. For $B/W < 1.5$ the states are localized, while for $B/W > 1.5$ they are extended. For $d = 1$ the critical value of B/W is infinite, meaning that unless $W = 0$, all states will be localized.

It is also useful to compare this formula to the Ioffe–Regel criterion. A measure of the size of the bandwidth B is the Fermi energy. For example, a metal with a half-filled band would have $B \approx 2E_F$, where the Fermi energy is measured with respect to the bottom of the band. If the mean free path is λ, one may think of the electron as effectively bound in a spherical box of mean size λ. The confinement energy would then be a measure of the spread of energies brought about by the inhomogeneities, so $W \approx \hbar^2/2m\lambda^2$ since $k \approx 1/\lambda$. Combining these formulas with Eq. (W7.26) and using $E_F = \hbar^2 k_F^2/2m$ gives the condition when localization occurs as

$$k_F\lambda < \sqrt{\frac{d}{2(d-1)}}. \tag{W7.27}$$

Note that in $d = 3$, $k_F\lambda < \sqrt{3/4} \approx 1$. For a metal such as Cu, $k_F \approx 5/a$, where a is the lattice constant, and so $\lambda < a/5$ for localization of electrons to occur.

It must be cautioned, however, that the current theoretical picture is not completely understood. There are theoretical arguments based on single-electron scattering from random potentials which say that in two dimensions there is only localization. There are also some experiments that seem to point to the existence of conductivity in two dimensions. There are also recent experiments suggesting that the M–I transition may be associated with the formation of a Wigner crystal (i.e., a two-dimensional crystallization of the electrons). Just what possible role many-body effects play in conductivity has yet to be clarified.

There are two factors involved in localization. One is, as has been seen, percolation. The other is phase interference of electrons traveling along different paths but connecting the same pair of points. In a random medium the phase differences

can be quite large, resulting in destructive interference. The effects of phase interference in lower dimensions are more extreme and may contribute to suppression of the conductivity.

W7.6 Properties of Carbon Nanotubes

Termination of Nanotubes. The nanotube must be capped at both ends for it not to have dangling bonds. An understanding for how this capping comes about can be had from examining Euler's theorem. Consider a polyhedron with N_v vertices, N_f faces, and N_e edges. Then for a simply connected body, $N_e - N_f - N_v = -2$. It will be assumed that each vertex connects to three adjoining polygons and each edge to two adjoining polygons. Let N_i denote the number of i-sided polygons in the structure. Then

$$N_e = \frac{1}{2}\sum_{i=3}^{\infty} iN_i, \tag{W7.28a}$$

$$N_v = \frac{1}{3}\sum_{i=3}^{\infty} iN_i, \tag{W7.28b}$$

$$N_f = \sum_{i=3}^{\infty} N_i. \tag{W7.28c}$$

Combining these equations with Euler's theorem gives

$$\sum_{i=3}^{\infty}(i-6)N_i = -12. \tag{W7.29}$$

For example, using only pentagons with $i = 5$ to terminate the ends of the nanotube, then $N_5 = 12$ and $N_i = 0$ for $i \neq 5$. Thus six pentagons are needed at each end since only half of the 12-sided polyhedron is needed. The fullerene molecule C_{60} has $N_5 = 12$ and $N_6 = 20$, so $(N_e, N_v, N_f) = (90, 60, 32)$.

Conductivity of Carbon Nanotubes. Adding a single electron to the nanotube costs electrostatic charging energy $E_c = e^2/8\pi\epsilon_0 C$, where C is the capacitance (relative to infinity) of the nanotube ($\approx 3 \times 10^{-17}$ F). Unless the potential bias across the tubule satisfies the condition $-eV + E_c < 0$, no current will flow. One refers to this as a *Coulomb blockade*. Similar phenomena occur in granular metals. However, if a quantum state of the wire overlaps the occupied states of one electrode and an empty state of the second electrode, conduction can occur via resonant tunneling through the quantum state. In this case there is zero-bias conductance. The conductance will be temperature dependent, being proportional to

$$\begin{aligned} G &\propto \int dE \int dE' \rho(E)\rho(E'+V) f(E)[1 - f(E'+V)]\delta(E - \Delta E)\delta(E' - \Delta E + V) \\ &\propto \operatorname{sech}^2\left[\frac{\beta}{2}(\Delta E - \mu)\right], \end{aligned} \tag{W7.30}$$

where the value of the quantum energy level relative to the chemical potential can be changed by a gate voltage $\Delta E - \mu = e\Delta V_{\text{gate}}/\alpha$, α being a constant determined by capacitance ratios. Thus there is a rapid variation of conductance with gate voltage.

Appendix W7A: Evaluation of Fermi Integrals

The Fermi integral to be evaluated is

$$I_j(\beta, \beta\mu) = \int_0^\infty \frac{E^{j+1/2}}{e^{\beta(E-\mu)} + 1}\, dE. \tag{W7A.1}$$

Let $x = \beta(E - \mu)$, so

$$I_j(\beta, \beta\mu) = \int_{-\beta\mu}^\infty \frac{dx}{\beta} \frac{(u + x/\beta)^{j+1/2}}{e^x + 1}. \tag{W7A.2}$$

Integrate this by parts to obtain

$$I_j(\beta, \beta\mu) = \frac{1}{(j + \frac{3}{2})\beta^{j+3/2}} \int_{-\beta\mu}^\infty (\beta\mu + \mathrm{x})^{j+3/2} \frac{e^x}{(e^x + 1)^2} dx. \tag{W7A.3}$$

Make a power series development in x and extend the lower limit of the integral to $-\infty$, to obtain

$$I_j(\beta, \beta\mu) = \frac{1}{(j + \frac{3}{2})\beta^{j+3/2}} \int_{-\infty}^\infty \left((\beta\mu)^{j+3/2} + \frac{1}{2}\left(j + \frac{3}{2}\right)\left(j + \frac{1}{2}\right) \times (\beta\mu)^{j-1/2} x^2 + \cdots \right) \frac{e^x}{(e^x + 1)^2} dx, \tag{W7A.4}$$

where the term linear in x integrates to zero. The integrals required are

$$\int_{-\infty}^\infty \frac{e^x}{(e^x + 1)^2} dx = 1, \tag{W7A.5}$$

$$\int_{-\infty}^\infty \frac{x^2 e^x}{(e^x + 1)^2} dx = 2\int_0^\infty \frac{x^2 e^{-x}}{(1 + e^{-x})^2} dx = 2\int_0^\infty dx\, x^2 \sum_{n=1}^\infty (-)^{n+1} n e^{-nx}$$

$$= 4\sum_{n=1}^\infty \frac{(-)^{n+1}}{n^2} = \frac{\pi^2}{3}. \tag{W7A.6}$$

The final result is

$$I_j(\beta, \beta\mu) = \frac{1}{(j + \frac{3}{2})\beta^{j+3/2}} \left[(\beta\mu)^{j+3/2} + \frac{\pi^2}{6}\left(j + \frac{1}{2}\right)\left(j + \frac{3}{2}\right)(\beta\mu)^{j-1/2} + \cdots \right]. \tag{W7A.7}$$

Using Eq. (W7A.7), two useful formulas may be derived. If $\psi(E)$ is a function of the form $\psi(E) = \sum p_j E^{j+1/2}$ with $j \geq 0$, then

$$\int_0^\infty \psi(E) f(E, T)\, dE = \int_0^\mu \psi(E)\, dE + \frac{\pi^2}{6} k_B^2 T^2 \left.\frac{\partial \psi}{\partial E}\right|_{E=\mu} + \cdots , \qquad \text{(W7A.8)}$$

where $f(E, T)$ is the Fermi–Dirac distribution. Also, letting $\psi(E) = \partial\phi(E)/\partial E$ and integrating by parts, one obtains

$$\int_0^\infty \phi(E) \frac{\partial f(E, T)}{\partial E}\, dE = -\phi(\mu) - \frac{\pi^2}{6} k_B^2 T^2 \left.\frac{\partial^2 \phi}{\partial E^2}\right|_{E=\mu} + \cdots . \qquad \text{(W7A.9)}$$

CHAPTER W8

Optical Properties of Materials

W8.1 Index Ellipsoid and Phase Matching

In the discussions so far[†] the effect of the crystalline lattice has been omitted. The description of light propagation in solids must take account of the breaking of rotational symmetry by the solid. In this section such effects are considered.

Light propagation in an anisotropic medium is often accompanied by birefringence (i.e., a speed of light that depends on the polarization of the light as well as its direction of propagation). In this section it is shown how the concept of the index ellipsoid can be utilized to determine the index of refraction. Then it is demonstrated how, by cleverly making use of birefringence, one may achieve the phase-matching condition, which is necessary for efficient nonlinear optical effects.

Start with Maxwell's equations, Eqs. (W8A.1) to (W8A.4), in a nonmagnetic material and imagine a plane electromagnetic wave, such as that drawn in Fig. 8.1 of the textbook with frequency ω and wave vector $\mathbf{k}$ propagating through it. Assuming that the fields vary as $\exp[i(\mathbf{k}\cdot\mathbf{r}-\omega t)]$, the equations become

$$\mathbf{k}\times\mathbf{E}=\omega\mathbf{B}, \qquad \frac{1}{\mu_0}\mathbf{k}\times\mathbf{B}=-\omega\mathbf{D}, \tag{W8.1}$$

$$\mathbf{k}\cdot\mathbf{D}=0, \qquad \mathbf{k}\cdot\mathbf{B}=0. \tag{W8.2}$$

For a linear, anisotropic dielectric

$$\mathbf{D}=\epsilon_0\overleftrightarrow{\epsilon}_r\cdot\mathbf{E}, \tag{W8.3}$$

where $\overleftrightarrow{\epsilon}_r$ is the dielectric tensor. Taking the vector product of Faraday's law with $\mathbf{k}$ and combining it with the other equations leads to an algebraic form of the wave equation:

$$\mathbf{k}\times(\mathbf{k}\times\mathbf{E})=\mathbf{k}(\mathbf{k}\cdot\mathbf{E})-k^2\mathbf{E}=-\mu_0\omega^2\mathbf{D}. \tag{W8.4}$$

Form the scalar product of this equation with $\mathbf{D}$ to obtain

$$\mathbf{D}\cdot\frac{1}{\overleftrightarrow{\epsilon}_R}\cdot\mathbf{D}=\left(\frac{\omega}{kc}\right)^2D^2=\left(\frac{D}{n}\right)^2. \tag{W8.5}$$

[†] The material on this home page is supplemental to *The Physics and Chemistry of Materials* by Joel I. Gersten and Frederick W. Smith. Cross-references to material herein are prefixed by a "W"; cross-references to material in the textbook appear without the "W."

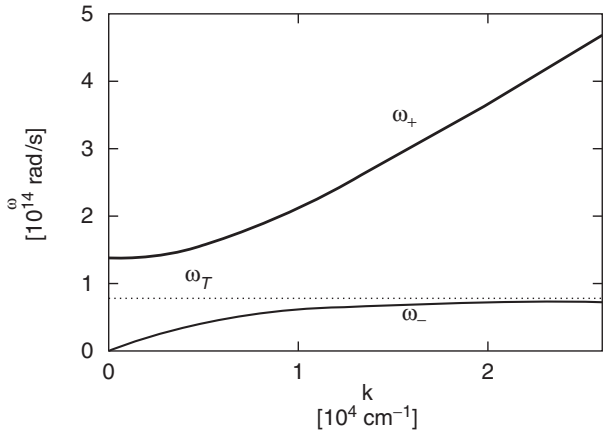

Figure W8.1. Polariton branches for MgO, from Eq. (W8.16) using $\epsilon(0) = 9.8$, $\epsilon(\infty) = 2.95$, and $\omega_T = 7.5 \times 10^{13}$ rad/s.

Here $1/\overleftrightarrow{\epsilon}_r$ is the inverse of the $\overleftrightarrow{\epsilon}_r$ matrix. The dielectric tensor is symmetric and will therefore be diagonal in some reference frame (called the *principal axis coordinate system*). Choose that frame, defined by the mutually perpendicular unit vectors $\{\hat{u}_i\}$, and write, using dyadic notation,

$$\overleftrightarrow{\epsilon}_r = n_1^2 \hat{u}_1 \hat{u}_1 + n_2^2 \hat{u}_2 \hat{u}_2 + n_3^2 \hat{u}_3 \hat{u}_3, \tag{W8.6}$$

where $n_i = \sqrt{\overleftrightarrow{\epsilon}_{r_i}}$. Usually, the set $\{\hat{u}_i\}$ will coincide with the symmetry axes of the crystal. Thus one finally obtains the pair of equations

$$\sum_i \left(\frac{n\hat{D} \cdot \hat{u}_i}{n_i} \right)^2 = 1, \tag{W8.7}$$

where $\hat{D} = \mathbf{D}/D$ is the direction of the displacement vector, and

$$\sum_i \hat{D}_i \cdot \hat{u}_i \hat{u}_i \cdot \mathbf{k} = 0. \tag{W8.8}$$

The first formula is the equation of an ellipsoid in **D** space whose axes are aligned with the principal axes and centered at the origin. It is called the *index ellipsoid*. The second equation is that of a plane through the origin in **D** space. The intersection of the plane with the ellipsoid produces the polarization ellipse. The intersection of this ellipse with the unit sphere determines the two pairs of possible directions for polarization of the wave.

Suppose that the vectors **D** and **k** are projected onto the principal axes:

$$\hat{D} = \hat{u}_1 \sin\theta \cos\psi + \hat{u}_2 \sin\theta \sin\psi + \hat{u}_3 \cos\theta, \tag{W8.9}$$

$$\mathbf{k} = k(\hat{u}_1 \sin\alpha \cos\beta + \hat{u}_2 \sin\alpha \sin\beta + \hat{u}_3 \cos\alpha). \tag{W8.10}$$

Then the two conditions become

$$\cos\theta \cos\alpha + \sin\theta \sin\alpha \cos(\beta - \psi) = 0, \tag{W8.11}$$

$$\left(\frac{\sin\theta\cos\psi}{n_1}\right)^2 + \left(\frac{\sin\theta\sin\psi}{n_2}\right)^2 + \left(\frac{\cos\theta}{n_3}\right)^2 = \frac{1}{n^2}. \tag{W8.12}$$

If one were to choose a direction of propagation perpendicular to one of the principal axes (e.g., $\hat{u}_3$), then $\alpha = \pi/2$ and $\sin\theta\cos(\psi - \beta) = 0$. There are two possibilities:

$$\sin\theta = 0, \qquad n = n_3 \equiv n_o, \tag{W8.13a}$$

or

$$|\psi - \beta| = \frac{\pi}{2}, \qquad \left(\frac{\sin\theta\sin\beta}{n_1}\right)^2 + \left(\frac{\sin\theta\cos\beta}{n_2}\right)^2 + \left(\frac{\cos\theta}{n_3}\right)^2 \equiv \frac{1}{n_e^2(\theta)}. \tag{W8.13b}$$

Here n_o is referred to as the *ordinary* index and $n_e(\theta)$ as the *extraordinary* index.

For crystals, the number of independent indices of refraction depends on the symmetry. For the monoclinic, triclinic, and orthorhombic crystals there are three independent indices. For the hexagonal, tetragonal, and trigonal crystals there are two independent indices. For the cubic class there is only one independent index. For amorphous materials the number of independent elements depends on whether or not there is any remnant orientational or positional order. A glass, which is random on the scale of the wavelength of light, is isotropic and has only one independent element. Liquid crystals may have two independent elements. Quantum-well devices may have two or even three independent elements, depending on the symmetry of the structure. One refers to materials with two independent components as being uniaxially symmetric. In that case, if $n_1 = n_2$, the extraordinary index is given by

$$\left(\frac{\sin\theta}{n_1}\right)^2 + \left(\frac{\cos\theta}{n_3}\right)^2 = \frac{1}{n_e^2(\theta)}. \tag{W8.14}$$

A list of indices of refraction for various optical materials is given in Table W8.1. A list of indices of refraction for various semiconductors is given in Table 11.7.

As discussed in Section 8.9, in any nonlinear optical process there are input waves and output waves. One constructs a net input wave by forming the product of the input waves. A similar construct may be formed for the output waves. Associated with these net waves are phases. For the nonlinear process to proceed efficiently, these phases must match each other. There can then be coherent transformation of the net input wave to the output waves over a considerable length in space. The necessity for phase matching occurs in nonlinear optics in processes where photons interact with each other by means of a nonlinear optical material. For example, one may have second-harmonic generation (SHG), where two ordinary wave photons of frequency ω and wave vector $k = \omega n_o(\omega)/c$ combine to form an extraordinary wave photon of frequency 2ω and wave vector $2\omega n_e(2\omega, \theta)/c$. Conservation of momentum then determines the angle θ for which phase matching occurs, via $n_o(\omega) = n_e(2\omega, \theta)$. Other possibilities exist, such as when an ordinary and an extraordinary photon at frequency ω combine to produce an extraordinary photon at 2ω, where $n_e(2\omega, \theta) = [n_e(\omega, \theta) + n_o(\omega)]/2$, and so on.

All nonlinear optical processes make use of phase matching to increase their efficiency. These include third-harmonic generation, three- and four-wave mixing, parametric down-conversion, and stimulated Raman and Brillouin scattering.

TABLE W8.1 Indices of Refraction for Materials at $\lambda = 589$ nm (in Vacuum) at $T = 300$ K

Material	Symmetry	n_1	n_2	n_3
AgCl	Cubic	2.071	—	—
AgBr	Cubic	2.253	—	—
NaCl	Cubic	1.544	—	—
KCl	Cubic	1.490	—	—
ZnSe	Cubic	2.89	—	—
MgO	Cubic	1.736	—	—
C (diamond)	Cubic	2.417	—	—
$SrTiO_3$	Cubic	2.403	—	—
Al_2O_3 (alumina)	Hexagonal	1.768	1.760	—
$CaCO_3$ (calcite)	Trigonal or hexagonal	1.658	1.486	—
MgF_2	Tetragonal	1.378	1.390	—
TiO_2 (rutile)	Tetragonal	2.616	2.903	—
As_2S_3 (orpiment)	Monoclinic	2.40	2.81	3.02
SiO_2 (α-quartz)	Hexagonal	1.544	1.553	—
SiO_2 (fused silica)	Amorphous	1.458	—	—
SiO_2 (trydimite)	Trigonal	1.469	1.470	1.471
Na_3AlF_6 (cryolite)	Monoclinic	1.338	1.338	1.339
$Cu_2CO_3(OH)_2$ (malachite)	Monoclinic	1.875	1.655	1.909
KH_2PO_4	—	1.510	1.469	—
PMMA	—	1.491	—	—
Polycarbonate	—	1.586	—	—
Polystyrene	—	1.590	—	—

Source: Data from M. J. Weber, *Handbook of Laser Science and Technology*, Vol. III, CRC Press, Boca Raton, Fla., 1986, and other sources.

W8.2 Polaritons

Infrared radiation propagating through crystals at frequencies close to the optical phonon frequencies propagates as coupled photon–phonon modes, called *polaritons*. Consider, for example, transverse modes. A simple description of these modes follows from combining the optical dispersion formula $\omega = kc/\sqrt{\epsilon_r(\omega)}$ with a Lorentz oscillator model for the dielectric function introduced in Eqs. (8.23), (8.25), and (8.28). It may be rewritten as

$$\epsilon_r(\omega) = \epsilon_r(0) + \frac{[\epsilon_r(\infty) - \epsilon_r(0)]\omega_T^2}{\omega^2 - \omega_T^2 + i\gamma\omega} \tag{W8.15}$$

for the case of a single oscillator of frequency ω_T. Solving the resulting quadratic equation in the variable ω^2 yields two branches:

$$\omega_\pm^2 = \frac{\epsilon_r(0)\omega_T^2 + k^2c^2 \pm \sqrt{(\epsilon_r(0)\omega_T^2 + k^2c^2)^2 - 4\epsilon_r(\infty)(kc\omega_T)^2}}{2\epsilon_r(\infty)}, \tag{W8.16}$$

where $\gamma \to 0$. These branches are plotted in Fig. W8.1 for the case of MgO. The lower branch has long-wavelength behavior given by $\omega = kc/\sqrt{\epsilon_r(0)}$, corresponding to a low-frequency photon. The upper branch has the asymptotic behavior $\omega = kc/\sqrt{\epsilon_r(\infty)}$, as for a high-frequency photon. The polaritons display the reststrahl gap, discussed in Section 8.4, between the frequencies ω_T and $\omega_L = \omega_T\sqrt{\epsilon_r(0)/\epsilon_r(\infty)}$. The fact that there is no polariton mode between these two frequencies means that propagation of light through the crystal is blocked there and it behaves as a good mirror in that frequency range.

Appendix W8A: Maxwell's Equations

The laws governing electricity and magnetism are Maxwell's equations. They consist of four equations, which will be presented in SI units:

1. Gauss's law,
$$\nabla \cdot \mathbf{D} = \rho, \tag{W8A.1}$$
where $\mathbf{D}$ is the electric displacement vector and ρ is the charge density
2. Gauss's law for magnetism
$$\nabla \cdot \mathbf{B} = 0, \tag{W8A.2}$$
where $\mathbf{B}$ is the magnetic flux density
3. Faraday's law
$$\nabla \times \mathbf{E} = -\frac{\partial \mathbf{B}}{\partial t}, \tag{W8A.3}$$
where $\mathbf{E}$ is the electric field
4. Ampère's law, as generalized by Maxwell:
$$\nabla \times \mathbf{H} = \mathbf{J} + \frac{\partial \mathbf{D}}{\partial t}, \tag{W8A.4}$$
where $\mathbf{H}$ is the magnetic field intensity and $\mathbf{J}$ is the current density

These equations are supplemented by the constitutive equations

$$\mathbf{D} = \epsilon_0\mathbf{E} + \mathbf{P}, \tag{W8A.5}$$

where $\epsilon_0 = 10^7/(4\pi c^2) \approx 8.854 \times 10^{-12}\text{C}^2\text{N}^{-1}\text{m}^{-2}$ is the permittivity of free space and $\mathbf{P}$ is the electric polarization vector (the electric dipole moment per unit volume). In addition,

$$\mathbf{B} = \mu_0(\mathbf{H} + \mathbf{M}), \tag{W8A.6}$$

where $\mu_0 = 4\pi \times 10^{-7}$ Wb $\text{A}^{-1}\text{m}^{-1}$ is the magnetic permeability of free space and $\mathbf{M}$ is the magnetization vector (the magnetic dipole moment per unit volume).

For linear isotropic materials, one writes Eq. (W8A.5) as

$$\mathbf{D} = \epsilon\mathbf{E} = \epsilon_r\epsilon_0\mathbf{E}, \tag{W8A.7}$$

where ϵ is the permittivity of the material and ϵ_r is its dielectric function or *relative permittivity*. The electric susceptibility is defined as $\chi_e = \epsilon_r - 1$, so $\mathbf{P} = \chi_e \epsilon_0 \mathbf{E}$. Thus $\epsilon = (1 + \chi_e)\epsilon_0$ and $\epsilon_r = 1 + \chi_e$. Also, Eq. (W8A.6) is written as

$$\mathbf{B} = \mu \mathbf{H} = \mu_r \mu_0 \mathbf{H}, \tag{W8A.8}$$

where μ is the permeability of the material and μ_r is its relative permeability. The magnetic susceptibility is defined as $\chi_m = \mu_r - 1$.

Two useful theorems follow from Maxwell's equations. The first is the *continuity equation*, the microscopic form of the law of conservation of charge. Equations (W8A.7) and (W8A.8) will be assumed to apply. Then

$$\nabla \cdot \mathbf{J} + \frac{\partial \rho}{\partial t} = 0, \tag{W8A.9}$$

which follows from taking the divergence of Eq. (W8A.4) and combining it with the time derivative of Eq. (W8A.1), using the identity $\nabla \cdot \nabla \times \mathbf{H} = 0$. The second is *Poynting's theorem*, the microscopic form of the law of conservation of energy:

$$\nabla \cdot \mathbf{S} + \frac{\partial u}{\partial t} = -\mathbf{E} \cdot \mathbf{J}, \tag{W8A.10}$$

where $\mathbf{S}$ is the Poynting vector, whose magnitude is the power per unit area (intensity) carried by the electromagnetic field, defined by

$$\mathbf{S} = \mathbf{E} \times \mathbf{H}, \tag{W8A.11}$$

and u is the electromagnetic field energy density, given by

$$u = \frac{1}{2} \int (\mathbf{E} \cdot \mathbf{D} + \mathbf{B} \cdot \mathbf{H})\, d\mathbf{r}. \tag{W8A.12}$$

The right-hand side of Eq. (W8A.10) gives the work done by the currents on the fields. Equation (W8A.10) follows from taking the scalar product of $\mathbf{E}$ with Eq. (W8A.4), subtracting the scalar product of $\mathbf{H}$ with Eq. (W8A.3), and making use of the identity $\nabla \cdot (\mathbf{E} \times \mathbf{H}) = \mathbf{H} \cdot \nabla \times \mathbf{E} - \mathbf{E} \cdot \nabla \times \mathbf{H}$.

Appendix W8B: Nonlocal Dielectric Function

The nonlocal relation between the electric displacement vector and the electric field vector (for linear isotropic materials) is

$$\mathbf{D}(\mathbf{r}, t) = \iint \epsilon(\mathbf{r} - \mathbf{r}', t - t')\mathbf{E}(\mathbf{r}', t')\, d\mathbf{r}'\, dt'. \tag{W8B.1}$$

Since the wavelength is much larger than the interatomic spacing, it is reasonable to assume that the dielectric function relating the fields at two points should depend only on the displacement between the two points. The assumption concerning its dependence

on the time difference is valid at frequencies low compared with electronic excitation frequencies. It is an approximation at higher frequencies.

One makes a Fourier expansion of the fields,

$$\mathbf{D}(\mathbf{r}, t) = \iint \mathbf{D}(\mathbf{q}, \omega) e^{i(\mathbf{q}\cdot\mathbf{r}-\omega t)}\, d\mathbf{q}\, d\omega, \tag{W8B.2}$$

$$\mathbf{E}(\mathbf{r}, t) = \iint \mathbf{E}(\mathbf{q}, \omega) e^{i(\mathbf{q}\cdot\mathbf{r}-\omega t)}\, d\mathbf{q}\, d\omega, \tag{W8B.3}$$

and inserts these expressions in Eq. (W8B.1) to obtain

$$\mathbf{D}(\mathbf{q}, \omega) = \epsilon(\mathbf{q}, \omega)\mathbf{E}(q, \omega), \tag{W8B.4}$$

where the Fourier-transformed dielectric function is given by

$$\epsilon(\mathbf{q}, \omega) = \int d\mathbf{r}\, dt \epsilon(\mathbf{r}, t) e^{-i(\mathbf{q}\cdot\mathbf{r}-\omega t)}. \tag{W8B.5}$$

Appendix W8C: Quantum-Mechanical Derivation of the Dielectric Function

In this appendix the quantum-mechanical derivation of the dielectric function will be given. The Hamiltonian is taken to be

$$H = H_0 - \boldsymbol{\mu} \cdot \mathbf{E}_0 \cos(\omega t) \exp(\alpha t) \equiv H_0 + H_1. \tag{W8C.1}$$

(For technical reasons one introduces a *switching factor*, with parameter $\alpha \to 0^+$, so that the field is turned on slowly from a value of zero at $t = -\infty$.) Let the nth electronic eigenstates of H_0 be denoted by $|n\rangle$, where

$$H_0|n\rangle = \epsilon_n|n\rangle. \tag{W8C.2}$$

To solve the time-dependent Schrödinger equation

$$H|\psi\rangle = i\hbar \frac{\partial}{\partial t}|\psi\rangle, \tag{W8C.3}$$

one writes the wavefunction (approximately) as

$$|\psi\rangle = \exp\left(-\frac{i}{\hbar}E_0 t\right)|0\rangle + \sum_{n>0} a_n(t) \exp\left(-\frac{i}{\hbar}E_n t\right)|n\rangle \tag{W8C.4}$$

and proceeds to solve for the coefficients $a_n(t)$. Assuming that the system starts out in state $|0\rangle$ at $t = -\infty$, one obtains

$$a_n(t) = -\frac{i}{\hbar}\int_{-\infty}^{t} e^{i\omega_{n0}t'} \langle n|H_1|0\rangle\, dt', \tag{W8C.5}$$

where $\omega_{n0} = (E_n - E_0)/\hbar$. The expectation value of the scalar product of the dipole operator with a constant vector $\mathbf{C}_0$ is

$$\langle\psi|\boldsymbol{\mu}\cdot\mathbf{C}_0|\psi\rangle = -\frac{1}{2\hbar}\sum_{n>0}\Bigg[\langle 0|\boldsymbol{\mu}\cdot\mathbf{C}_0|n\rangle\langle n|\boldsymbol{\mu}\cdot\mathbf{E}_0|0\rangle \times\left(\frac{e^{-i\omega t}}{\omega-\omega_{n0}+i\alpha}-\frac{e^{i\omega t}}{\omega+\omega_{n0}-i\alpha}\right)+\text{c. c.}\Bigg], \quad \text{(W8C.6)}$$

where c.c. means complex conjugate.

The notation is now modified so that the initial state (previously labeled $|0\rangle$) can be any of a set $\{|m\rangle\}$, with associated probability f_m, given by a Fermi factor. Then, by rearranging the indices, one may write

$$\langle\psi|\boldsymbol{\mu}\cdot\mathbf{C}_0|\psi\rangle = -\frac{1}{2\hbar}\sum_{nm}\left[\langle n|\boldsymbol{\mu}\cdot\mathbf{C}_0|m\rangle\langle m|\boldsymbol{\mu}\cdot\mathbf{E}_0|n\rangle\frac{e^{-i\omega t}}{\omega-\omega_{mn}+i\alpha}(f_n-f_m)+\text{c. c.}\right]. \quad \text{(W8C.7)}$$

Dividing by the volume, the expression becomes

$$\frac{1}{V}\langle\psi|\boldsymbol{\mu}\cdot\mathbf{C}_0|\psi\rangle = \frac{1}{2}\epsilon_0\mathbf{C}_0\cdot\overleftrightarrow{\chi}(\omega)\cdot\mathbf{E}_0e^{-i\omega t}+\text{c. c.}, \quad \text{(W8C.8)}$$

where the dynamic electric susceptibility dyadic is

$$\overleftrightarrow{\chi}(\omega) = -\frac{1}{\epsilon_0\hbar V}\sum_{\substack{m,n\\ m\neq n}}\langle n|\boldsymbol{\mu}|m\rangle\langle m|\boldsymbol{\mu}|n\rangle\frac{f_n-f_m}{\omega-\omega_{mn}+i\alpha}. \quad \text{(W8C.9)}$$

The dielectric function is

$$\overleftrightarrow{\epsilon}_r(\omega) = \overleftrightarrow{I}+\overleftrightarrow{\chi}(\omega), \quad \text{(W8C.10)}$$

where $\overleftrightarrow{I}$ is the unit dyadic. In the special case of a crystal, the states are labeled by the quantum numbers $\{n, \mathbf{k}, s\}$ and the energy eigenvalues are given by $\epsilon_n(\mathbf{k})$. Instead of having discrete energy levels, the levels are broadened into bands. The expression for the optical dielectric function becomes

$$\overleftrightarrow{\epsilon}_r(\omega) = \overleftrightarrow{I}+\frac{1}{\epsilon_0 V}\sum_{nn'}\sum_{\mathbf{k}\mathbf{k}'}\sum_{s}\frac{\langle n\mathbf{k}|\boldsymbol{\mu}|n'\mathbf{k}'\rangle\langle n'\mathbf{k}'|\boldsymbol{\mu}|n\mathbf{k}\rangle}{\epsilon_{n'}(\mathbf{k}')-\epsilon_n(\mathbf{k})-\hbar\omega-i\hbar\alpha}[f_n(\mathbf{k})-f_{n'}(\mathbf{k}')]. \quad \text{(W8C.11)}$$

From Eq. (W8C.11) one sees that the oscillator strengths are determined by the transition matrix elements (i.e., the dipole matrix elements connecting electronic states of the system). Comparing Eqs. (W8C.11) and (8.28), one sees that the resonance frequencies are just the energies of the quantum states divided by Planck's constant.

CHAPTER W9

Magnetic Properties of Materials

W9.1 Jahn–Teller Effect

Another effect that should be mentioned is the distortion of the octahedral arrangement of the six NN O^{2-} ions by $3d^4$ or $3d^9$ cations such as Mn^{3+} or Cu^{2+}, respectively. Due to the occupation of the $d_{x^2-y^2}$ and d_{z^2} atomic orbitals by the $3d$ electrons in these ions, additional asymmetric Coulomb forces will cause shifts in the positions of the cations and anions, thus producing additional tetragonal or octahedral distortions of the crystal. These distortions, which are a result of the *Jahn–Teller effect*, can remove the degeneracy of the lowest energy level. The Jahn–Teller effect corresponds to the removal of the ground-state degeneracy for a magnetic ion in a site of high symmetry by distortions of the structure which lower both the energy and the symmetry of the system. In the context of crystal field theory, the *Jahn–Teller theorem* states that such distortions are in fact expected to occur under certain specific conditions (e.g., when the symmetric ground state is not a *Kramers doublet* and when the effect is strong enough to dominate thermal effects and the effects of spin–orbit interaction).

W9.2 Examples of Weak and Strong Crystal Field Effects

The ionic complexes $Fe^{3+}(F^-)_6$ and $Fe^{3+}(CN^-)_6$ are examples of the weak- and strong-field limits, respectively, for the Fe^{3+} ion in an octahedral crystal field. In the former case the $3d^5$ Fe^{3+} ion has spin $S = \frac{5}{2}$, as expected from Hund's rules for a free ion, while in the latter case the Fe^{3+} spin $S = \frac{1}{2}$, corresponding to a single unpaired d electron. These values of the spin S are consistent with the predictions of crystal field theory presented in Table 9.2 of the textbook.[†] Crystal field theory is thus able to explain the variation in magnetic properties of the same ion in different crystal structures. In terms of the alternative molecular orbital theory, highly covalent bonding between the Fe^{3+} cation and the surrounding anions is proposed to occur in the strong-field $Fe^{3+}(CN^-)_6$ complex, while in the weak-field $Fe^{3+}(F^-)_6$ complex the bonding between cation and anions is primarily ionic with only a small covalent component.

W9.3 Crystal Fields and Cr^{3+} in Al_2O_3

The effects of crystal fields on a Cr^{3+} ion with a $3d^3$ electronic configuration in an octahedral site will now be considered in greater detail. Examples include Cr^{3+} in

[†] The material on this home page is supplemental to *The Physics and Chemistry of Materials* by Joel I. Gersten and Frederick W. Smith. Cross-references to material herein are prefixed by a "W"; cross-references to material in the textbook appear without the "W."

the solid antiferromagnetic oxide Cr_2O_3 or as an impurity or dopant ion in *ruby* (i.e., Al_2O_3), where each Cr^{3+} replaces an Al^{3+} ion. The latter example actually corresponds to the first solid-state material to exhibit laser action, as described in Chapter 18. In each of these examples six O^{2-} ions are the NNs of each Cr^{3+} ion. The free-ion ground state of the $3d^3$ Cr^{3+} ion is ${}^4F_{3/2}$ ($S = \frac{3}{2}$, $L = 3$, $J = L - S = \frac{3}{2}$) according to Hund's rules (see Table 9.1). The free-ion energy levels of Cr^{3+} and their splitting in an octahedral crystal field are shown in Fig. W9.1.†

The splitting of the energy levels of the Cr^{3+} ion by the crystal field is much larger than the splitting due to the spin–orbit interaction, not shown in Fig. W9.1, between free-ion energy levels with the same S and L but different J, (i.e., $J = L - S = \frac{3}{2}$, $\frac{5}{2}$, $\frac{7}{2}$, up to $J = L + S = \frac{9}{2}$. The ground-state ${}^4F_{3/2}$ configuration of the free Cr^{3+} ion, which is $(2S + 1)(2L + 1) = 28$-fold degenerate, is split into three levels in the crystal

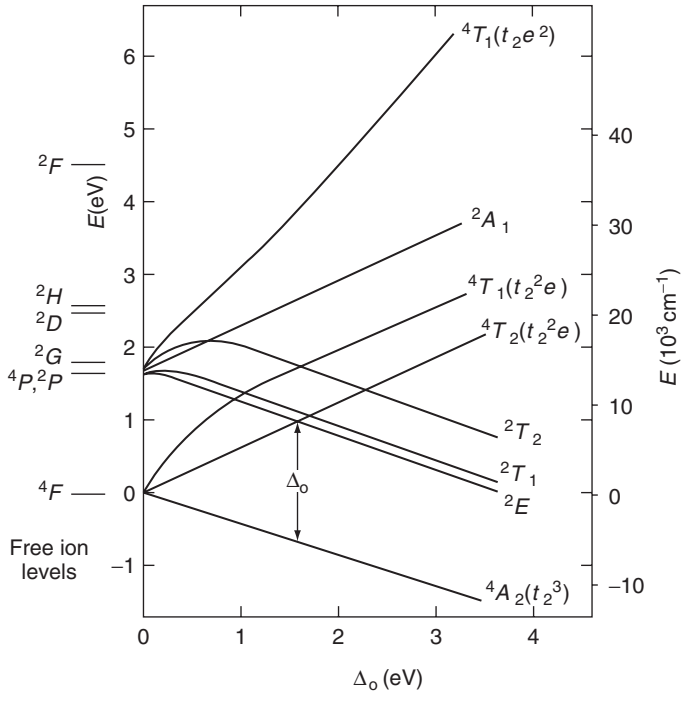

Figure W9.1. Free-ion energy levels of Cr^{3+} and their splitting in an octahedral crystal field shown in a Tanabe–Sugano diagram. The ground state of the $3d^3$ Cr^{3+} ion, ${}^4F_{3/2}$ ($S = \frac{3}{2}$, $L = 3$, $J = L - S = 3/2$), is split into three levels in the crystal field: a lower ${}^4A_2$ level and two upper levels, ${}^4T_2$ and ${}^4T_1$. The value $\Delta_o \approx 1.8$ eV for Cr^{3+} in Al_2O_3 is obtained from optical absorption spectroscopy.

† Energy-level diagrams known as Tanabe–Sugano diagrams for ions with $3d^n$ configurations in both octahedral and tetrahedral crystal fields are shown as functions of crystal field strength in Sugano et al. (1970, pp. 108–111). The transitions from the high-spin state ($\Delta_o < U$) to a state with lower spin ($\Delta_o > U$) are shown in these diagrams to occur at critical values of Δ_o for ions with $3d^4$, $3d^5$, $3d^6$, and $3d^7$ configurations.

TABLE W9.1 Mulliken Symbols for Crystal Field Representations[a]

Symbol M	Dimensionality	Symmetry
A	One	Symmetric with respect to rotation by $2\pi/n$ about the principal C_n axis.
B	One	Antisymmetric with respect to rotation by $2\pi/n$ about the principal C_n axis.
E	Two	
T	Three	
g (subscript)	—	Attached to symbols for representations that are symmetric with respect to inversion
e (subscript)	—	Attached to symbols for representations that are antisymmetric with respect to inversion

[a]For additional details, see F. A. Cotton, *Chemical Application of Group Theory*, 3rd ed., Wiley-Interscience, New York, 1990, p. 90.

field, a lower fourfold degenerate $^4A_2$ level and two upper levels, $^4T_2$ and $^4T_1$, each of which is 12-fold degenerate. These new levels in the crystal field are denoted by the group-theoretic labels ^{2S+1}M, where M refers to the *Mulliken notation*. The meanings of the Mulliken symbols are summarized briefly in Table W9.1.

Note that L is no longer a good quantum number in the presence of the crystal field and so can no longer be used to designate the new levels. The $^4A_2$ level remains the lowest energy level for all crystal field strengths, and therefore a high-spin to low-spin transition is not observed for Cr^{3+} in octahedral crystal fields, as expected from Table 9.2.

The crystal field splittings Δ_o of the energy levels of the Cr^{3+} ion are also typically larger than splittings due to the Coulomb interaction between free-ion levels with different L (e.g., between the $^4F_{3/2}$ ground state and the ^4P, ^2P, ^2G, ^2D, ^2H, and ^2F excited states shown in Fig. W9.1). As a result of crystal field splitting, the ground state of the ion is no longer $(2L + 1) =$ sevenfold orbitally degenerate. Instead, orbitals with different values of m_l now have different energies in the solid. The splitting of the ground-state level in a magnetic field therefore lifts only the degeneracy due to the spin S. As a result, the ion acts magnetically as if $J = S$, with an effective magneton number $p = g\sqrt{S(S+1)}$. This is consistent with the p observed for Cr^{3+}, presented in Table 9.1.

The value of the crystal field splitting Δ_o (often referred to in the literature as $10Dq$) for Cr^{3+} in Al_2O_3 has been obtained from optical spectroscopy. The optical absorption spectrum observed for Al_2O_3 containing Cr^{3+} as an impurity cannot be explained as being due to absorption by the Al_2O_3 host or to transitions between energy levels in the free Cr^{3+} ion. Instead, the absorption is due to transitions between the new energy levels of the Cr^{3+} ion in the octahedral crystal field. The specific transitions involved are from the ground-state $^4A_2$ level to the excited-state levels shown in Fig. W9.1, including the ^2E, $^2T_1$, $^4T_2$, $^2T_2$, and $^4T_1$ levels. The value $\Delta_o = 1.8$ eV is obtained in this way. These energy levels for the Cr^{3+} ion lie within the energy gap of the Al_2O_3 host, as is often the case for transition metal impurities in insulating materials.

The crystal field quenches the orbital angular momentum L by splitting the originally orbitally degenerate levels into levels separated by energies that are much greater than mH, where m is the magnetic moment of the atom or ion. In this case the magnetic field can split the spin-degenerate levels of the ground state only into the $(2S + 1)$ nondegenerate levels, which are responsible for the paramagnetic susceptibility of the ion, discussed in more detail in Section 9.4.

W9.4 Experimental Results for χ in the Free-Spin Limit

Experimental results[†] for the contribution of Mn spins to the low-field magnetic susceptibility χ of a series of six dilute alloys of Mn in Au are shown in Fig. W9.2, plotted in this case as χ versus T/n on a logarithmic plot. The fact that Mn impurities at dilute concentrations tend to act as free spins in Au is clear since the measured values of χ for the six alloys lie close to a single straight line with a slope of -1, consistent with Curie law behavior. Note also that since the measured values of $\chi = M/H$ are much less than 1, it follows that $M \ll H$. This justifies the use of the approximation $B = \mu_o H$. Assuming that $g = 2$, the value of the magnitude of the spin for Mn in Au obtained from the Curie constant C is $S = 2.25 \pm 0.1$, which is close to the Mn^{2+} free-ion value of $S = 2.5$ (see Table 9.1). This value of S is the same as that obtained from the measured saturation magnetization for the same alloys, using $S = M_{sat}/ng\mu_B$.

Evidence for the appearance of interactions at high n and low T can be seen in Fig. W9.2 where χ at low T for the highest-concentration AuMn alloy falls below the straight line that represents the Curie law behavior observed for the lower-concentration

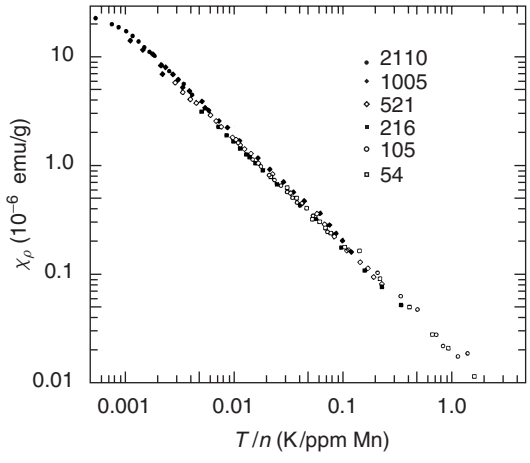

Figure W9.2. Experimental results for the contribution of Mn spins to the low-field magnetic susceptibility χ of a series of six dilute alloys of Mn in Au are shown plotted as χ versus T/n on a logarithmic plot. The concentration n of Mn spins is given in parts per million (ppm). [From J. C. Liu, B. W. Kasell, and F. W. Smith, *Phys. Rev. B*, **11**, 4396 (1975). Copyright © 1975 by the American Physical Society.

[†] J. C. Liu, B. W. Kasell, and F. W. Smith, *Phys. Rev. B*, **11**, 4396 (1975).